2011

Modeling and Performance Investigation of a Rotor with Dissimilar Bearing Support System

Yunlu Li
Cleveland State University

MODELING AND PERFORMANCE INVESTIGATION OF A ROTOR WITH DISSIMILAR BEARING SUPPORT SYSTEM

YUNLU LI

Bachelor of Engineering in Mechanical Engineering

Shenyang Institute of Technology, China

July, 2007

Submitted in partial fulfillment of requirements for the degree

MASTER OF SCIENCE IN MECHANICAL ENGINEERING

at the

CLEVELAND STATE UNIVERSITY

April, 2011

This thesis has been approved

for the Department of MECHANICAL ENGINEERING

and the College of Graduate Studies by

_____

Dr. Jerzy T. Sawicki, Thesis Committee Chairperson
Department of Mechanical Engineering, CSU

_____

Dr. Asuquo B. Ebiana
Department of Mechanical Engineering, CSU

_____

Dr. Ana V. Stankovic
Department of Electrical and Computer Engineering, CSU

ACKNOWLEDGEMENTS

First of all, I would like to show my deepest gratitude to Dr. Jerzy T. Sawicki, my academic advisor, for providing me with supports and guidance throughout my pursuit of master's degree. His passion and rigorous attitude towards research is always an inspiration for me. This thesis research would never have been accomplished without Dr. Sawicki's guidance and encouragement.

Thanks also go to Alexander Pesch, my colleague, for giving numerous precious suggestions for both experimental work and thesis writing, which led me throughout the thesis research.

I would also like to thank Dr. Asuquo B. Ebiana and Dr. Ana V. Stankovic for serving as my thesis evaluation committee members, for their time, reviewing the thesis, and suggestions. Thanks to all my colleagues in the Center for Rotating Machinery Dynamics and Control laboratory at Cleveland State University, especially Volodymyr Mykhaylyshyn, for helping me in setting up the experimental test rig and collecting data.

In addition, I would like to thank all my friends for being by my side, which makes me feel like at home and not alone when studying in the United States.

Last but not least, gratitude goes to my parents, Mr. Wan Li, and Mrs. Piyan Liu, for their selfless love, encouragement, and supports throughout my growth and academic pursuit.

MODELING AND PERFORMANCE INVESTIGATION OF A ROTOR WITH DISSIMILAR BEARING SUPPORT SYSTEM

YUNLU LI

ABSTRACT

Different types of bearings have different dynamic characteristics. By using one type of bearing at one end of a rotor and another type of bearing at the other end of the rotor, it is possible to exploit the advantages of both types in the same system. One example of such combination is a bronze bushing and active magnetic bearing (AMB). In the available literature, there are examples of such systems but are not fully explored with regard to how to model the system to fully utilize both support type properties. This thesis investigates the modeling and performance of such a dissimilar bearing support system. An experimental test rig with a rotor supported at one end by AMB and at the other end by bushing is modeled with two different methods, i.e., approximate analytical approach and finite element analysis (FEA). A cost function minimizing AMB controller design method is used for both system models, resulting in two controllers of the same form. Both controllers are implemented on the experimental test rig. AMB suspension is achieved, steady state orbits are measured at several selected constant speeds. Then experimental results are compared to numerical simulations and recommendations made regarding the utilization of these dissimilar bearing supports.

TABLE OF CONTENTS

LIST OF TABLES

LIST OF FIGURES

Figure

NOMENCLATURE

A_g = Area of active magnetic bearing pole face [μm^2]

$\mathbf{A_{amp}}$ = Linear state-space dynamic matrix of the power amplifier

$\mathbf{A_{ff}}$ = Linear state-space dynamic matrix of the free-free rotor model

$\mathbf{A_{open}}$ = Linear state-space dynamic matrix of the open-loop three-mass model

$\mathbf{A_s}$ = Linear state-space dynamic matrix of the open-loop three-mass model with supports

$\mathbf{a}$ = Two dimensional acceleration vector [$\frac{m}{s^2}$]

$\mathbf{B_{amp}}$ = Linear state-space input matrix of the power amplifier

$\mathbf{B_{ff}}$ = Linear state-space input matrix of the free-free rotor model

$\mathbf{B_{open}}$ = Linear state-space input matrix of the open-loop three-mass model

$\mathbf{B_s}$ = Linear state-space input matrix of the open-loop three-mass model with supports

$\mathbf{C_{amp}}$ = Linear state-space output matrix of the power amplifier

$\mathbf{C}$ = Damping matrix

C_b = Damping of the bronze bushing [$\frac{N\text{-}s}{m}$]

$\mathbf{C_{ff}}$ = Linear state-space output matrix of the free-free rotor model

$\mathbf{C_s}$ = Linear state-space output matrix of the open-loop three-mass model with supports

$\mathbf{C_{open}}$ = Linear state-space output matrix of the open-loop three-mass model

C_{s1} = Damping on the motor side section of the shaft for the approximate analytical model [$\frac{N\text{-}s}{m}$]

C_{s2} = Damping on the non-motor side section of the shaft for the approximate analytical model [$\frac{N\text{-}s}{m}$]

$\mathbf{D_{amp}}$ = Linear state-space feed through matrix of the power amplifier

$\mathbf{D_{ff}}$ = Linear state-space feed through matrix of the free-free rotor model

$\mathbf{D_{open}}$ = Linear state-space feed through matrix of the open-loop three-mass model

$\mathbf{D_s}$ = Linear state-space feed through matrix of the open-loop three-mass model with supports

e = Eccentricity [μm]

F = Two dimensional force vector [N]

$\overline{F}$ = Force generated from the active magnetic bearing [N]

F_x = Force in the X direction [N]

F_y = Force in the Y direction [N]

g = Acceleration due to gravity [$\frac{m}{s^2}$]

g_0 = Effective gap between AMB rotor and pole [μm]

G = Gyroscopic matrix

G = Transfer function of the controller

G_L = Transfer function of the low pass filter

G_N = Transfer function of the notch filter

G_{PD} = Transfer function of the PD controller

I_b = Bias current in an active magnetic bearing coil [A]

I_c = Control current in an active magnetic bearing [A]

J = Cost function

K = Stiffness matrix for the approximate analytical model [$\frac{N}{m}$]

K_b = Stiffness of the bronze bushing [$\frac{N}{m}$]

K_D = Derivative gain of the controller [$\frac{A\text{-}s}{\mu m}$]

K_i = Current stiffness of the active magnetic bearing [$\frac{\text{N}}{\text{A}}$]

K_I = Integral gain of the controller [$\frac{\text{A}}{\mu\text{m-s}}$]

K_P = Proportional gain of the controller [$\frac{\text{A}}{\mu\text{m}}$]

K_{s1} = Stiffness on the motor side section of the shaft on the approximate analytical model [$\frac{\text{N}}{\text{m}}$]

K_{s2} = Stiffness on the non-motor side section of the shaft on the approximate analytical model [$\frac{\text{N}}{\text{m}}$]

K_t = Total gain of the controller

K_x = Position stiffness of the active magnetic bearing [$\frac{\text{N}}{\text{m}}$]

$\mathbf{M}$ = Mass matrix for the approximate analytical model [kg]

m = Mass [kg]

m_l = Left lumped mass of the approximate analytical model [kg]

m_m = Middle lumped mass of the approximate analytical model [kg]

m_r = Right lumped mass of the approximate analytical model [kg]

N = Number of windings in an active magnetic bearing coil

$\mathbf{q}$ = Two dimensional X-Y position vector [μm]

t = Time [s]

$\mathbf{u}$ = Input vector

W_1 = Weighting factor for displacement

W_2 = Weighting factor for current

x = Displacement of the rotor in horizontal direction [μm]

x_l = Displacement of the left lumped mass in horizontal direction [μm]

x_m = Displacement of the middle lumped mass in horizontal direction [μm]

x_r = Displacement of the right lumped mass in horizontal direction [μm]

x = Position vector [μm]

y = Displacement of the rotor in vertical direction [μm]

y_l = Displacement of the left lumped mass in vertical direction [μm]

y_m = Displacement of the middle lumped mass in vertical direction [μm]

y_r = Displacement of the right lumped mass in vertical direction [μm]

y = Output vector

α =Angle of active magnetic bearing pole face [rad]

ω = rotor angular speed [$\frac{\text{rad}}{\text{s}}$]

ω_{lp} = Frequency of the low pass filter [$\frac{\text{rad}}{\text{s}}$]

ω_n = Frequency of the notch filter [$\frac{\text{rad}}{\text{s}}$]

ζ_{lp} = Damping ratio of the low pass filter

ζ_n = Damping ratio of the notch filter

μ_0 = Permeability of a vacuum [$\frac{\text{H}}{\text{m}}$]

Φ = Modal matrix of the rotor

CHAPTER I

INTRODUCTION

1.1 Introduction

Rotating machines are widely used in industry, since rotation offers a way to transfer power from one point to another, or convert motion to different planes through gears, belts, shafts etc.. Reliability and stability of rotating machines operating often at high speeds are very important in industry. Rotating machine usually includes a rotor, bearings and a support structure. Each component of the system has an effect on the overall dynamic behavior of the machine. To keep a stable motion of rotor machinery is an important motivating factor in looking into the dynamic behavior of the rotating system.

At least two bearings are needed to support a rotor. The same type of bearing with the same parameters is usually preferred for simplicity. Models of these systems are usually based on an isotropic assumption. In other words, isotropic stiffness and damping in vertical and horizontal planes, both bearing supports are identical and symmetric bearing locations. Also it is convenient if the rotor itself is symmetric. Symmetric models

of the rotor bearing system offer several advantages. For example, a typical symmetric rotor bearing model, the extended Jeffcott rotor, is converted to a two mass-spring-damper system with two degree-of-freedom by Kirk [1991]. With his assumptions and simplifications, the equations of motion for the simplified mass-spring-damper system are readily available for further analysis. Furthermore, for a geometrically symmetric configuration with both ends having bearings of the same properties, rotor mode shape is symmetric with respect to the bearing mid-span of the shaft.

But, in reality, due to reasons such as manufacture differences, wear of bearing parts during operation, non symmetric external forces, assembling misalignment and so on, systems with identical bearing supports do not exist. Thus, anisotropy and dissimilarity of such system must be studied in order to provide more realistic results for rotating machinery.

In this thesis, two different types of bearing supports with significantly different features, bushing and active magnetic bearing (AMB) are used with an experimental test rig. The modeling and performance of the test rig is examined to look at the problem. The AMB has unique capabilities such as embedded real time system monitoring, active vibration control, displacement tracking, or tunable stiffness and damping. The AMB also has disadvantages such as low static load capacity and possible instability, especially for a flexible rotor system. The bushing, have higher static load capacity and being inherently stable, can make up for the AMB's deficiencies. In the later section, a literature review will be provided to discuss the development of the rotor. Published works on AMB suspension will also be included. Then, the scope of this thesis will be provided to guide the reader through the whole work.

1.2 Literature Review

Childs [1993] provides the reader in his book with the background in analysis techniques related to rotating machinery dynamics. It is a good reference for those engineers and researchers who are involved with rotating machinery design and analysis. Several stages during the development of rotating machinery are pointed out in the reference. Early investigations of rotordynamics are only related to rotor structure, without concerns for any bearings; they examine the critical speeds for a flexible rotor. In the early 1960s, work such as Lund and Sterlicht [1962] focuses on rotor supports with hydrodynamic bearings. In the mid 1970s, since the increase of rotational speed of many machine parts, more components of a rotating system are taken into account. Many works focus on rotordynamic instability problems. They are interested in the influences on fluid-structure-interaction forces. While nowadays, for the sake of high performance of rotating machinery, all structure interaction forces and influence factors should be considered.

Since this thesis will look into the problem for a rotor system with a support of two different types of bearings, early published papers of rotor system with different bearings will be overviewed in the following section. The dynamics of bearings exhibit some non-linear characteristic. Many published works focus on the non linearity of the rotor bearing dynamics, such as Cheng [2006], Sinou [2009], Chang [2008] and Tiwari [1991]. Bearing foundations, as a crucial component in the system, have been studied by researchers in their works, such as, Kang et.al. [2002]. Kirk and Gunter [1972] finds the dynamic unbalance response and transient motion of a three-mass extended Jeffcott rotor in elastic bearings mounted on damped, flexible support. They provided design charts for

minimizing the rotor amplitude. They investigated the system response for two types of excitation forces, corresponding to unbalance excitation force at the mid span disk, and a constant magnitude harmonic excitation applied at the bearings. The paper concentrates on the solution of a two degree-of-freedom model developed by extending the original Jeffcott rotor to include bearing stiffness and damping, and with journal mass for modeling AMB supports, with non-collocation of the bearing and AMB sensor taken into account. Adiletta [1996] adopted a simple Jeffcott like experimental rotor with a shaft mass that is negligible with respect to the disk, and supported with all ball bearings. They set up an experimental model to check in a straightforward manner the non-linearity of the system and confirm results of theoretical analysis. Trajectory plots of the disk center and phase diagrams of component motions are shown. Friswell [2006] introduces a method for the analysis of rotor models where supports are considered. He pointed out that extra supports are often used in structures to increase natural frequencies, reduce displacements due to static loads, or to improve structural performance. Numerous papers can be found discussing the dynamic behavior of a simply supported rotor system. Since the simply supported rotor case is a mature topic, the reader is referred to rotordynamic handbooks such as Chong [1993].

In the majority of former studies which do consider different types of bearings, researchers neglect the rotor flexibility and disk gyroscopic effect in getting the overall governing equations of motion. Mohiuddin [1998] compared the various methods for vibration analysis of rotor bearing systems. The first is a discretization approach, using finite element analysis (FEA), where the rotor bearing system is approximated by motions described by a set of ordinary differential equations at each node. The other is an

analytical method where the equations of motions of the system are described by partial differential equations. Model reduction techniques were applied to a complicated rotor bearing system, and the Lagrangian approach was employed. In the model, shear deformation, gyroscopic effect and rotary inertia are taken into account. Responses to different types of excitations are generated from the model. There are many papers which incorporate the finite element methods in deriving the responses and dynamics for the rotor bearing systems, such as Chen [1997] and Milne [1994].

AMB supports in a variety of applications are becoming more and more popular because they provide unique advantages such as providing a frictionless operation environment for higher speeds, increased efficiency, eliminate the need for lubricant, prevent lubricant contamination of the product, as well as allowing for active vibration control and fault monitoring. Nevertheless, emerging papers dealing with magnetic power failure show another drawback aspect of the AMBs. Cuesta [2003] investigated the rotor behavior when the levitated rotor is in an overload regime. The work presents a rotor supported by magnetic bearing on the non-drive end, a bronze bushing on the other. A model was proposed for description of dynamical interaction between the backup bearing and the rotor during the impact. A detailed ball bearing model used in finding the dynamic behavior of a flexible rotor during drop is studied by Antti [2007]. Although not the focus of that work, a better understanding and modeling of a rotor system with a traditional support and AMB support will aid research in these areas.

1.3 Scope of work

The scope of this thesis is to develop an algorithm for an extended Jeffcott rotor with dissimilar bearing support, specifically, one end supported with a typical bronze bushing and the other end levitated by an AMB. In literature we can find such rotors supported by either two conventional bearings or two AMBs, but research related to dissimilar bearing system has not been fully investigated so far. So, this thesis will focus on the analysis of dynamic behavior of a rotor bearing system upon dissimilar support. This analysis will be used for controller design and will compare the model made using finite elements and subsequent controller to the model and subsequent controller made using an approximate analytical method similar to the extended Jeffcott rotor model, but enhanced to accommodate the non-negligible effects of the AMB.

Chapter I is the introduction and literature review for the whole thesis. Chapter II is an overview and set up of the experimental test rig. Chapter III sets up the approximate analytical rotor model and finite element model of the investigated system. Open-loop models of the system with AMB control current input and position output are assembled using both rotor models. Static deflections, critical speed map, Campbell diagram, and graphs of the mode shapes are shown for the unsupported finite element rotor in this chapter. Chapter IV introduces a cost function AMB controller design approach applied to the bushing and AMB support system. Two controllers are derived for the two different modeling methods. One controller is based on approximate analytical rotor model while the other is based on FEA model. The controller developed using the approximate analytical model is called controller “A”, and the controller developed using the finite element model is called controller “B”. Rotor behavior is numerically simulated

utilizing the models and derived controllers for several selected rotation speeds. Chapter V will show experimental results using the two controllers implemented on the test rig at the same speed as simulated in Chapter IV. Then a comparison of cost index values using both controllers is made through experimental and simulation. Finally, Chapter VI summarizes the whole thesis, draws conclusions and outlines future research directions.

CHAPTER II

EXPERIMENTAL TEST RIG

2.1 Overview and Description of the Test Rig

The RK-4 Rotor test rig in this study was manufactured by Bently Nevada and fitted with an AMB manufactured by Revolve Magnetic Bearing Inc, Canada. The experimental test rig is shown below in Figure 2.1.

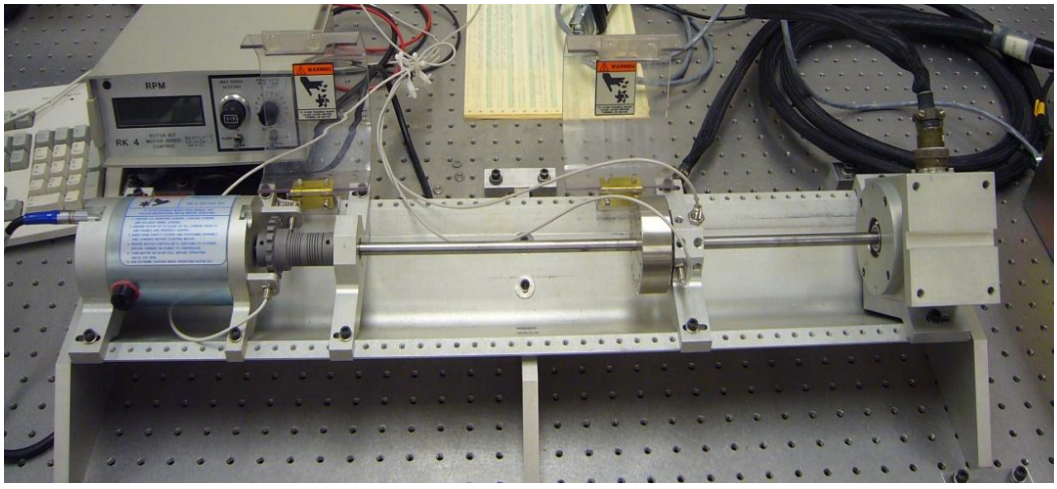

Figure 2. 1 Experimental test rig

The system's motor, is 48VDC, runs from 0 to 15,000 RPM. This motor provides the system with rotation torque that allows for a rotordynamic investigation. A flexible motor coupling connects the motor to the shaft, allowing for small axial and radial movement of the shaft. The test stand also comes with an adjustable base which allows for axial movement of system components to achieve different system configurations. A V-shaped base is employed in the rig, which allows for axial flexibility of the location of the disk and the AMB, making it possible for a vertical Y axis and a horizontal X axis orientation for the AMB. A disk is mounted on a defined location near the middle of the bearing span of a bushing and an AMB. The shaft is supported by a bronze bushing on the left end (motor side) and a radial AMB supporting at the right end. The SKF MB340G4-ERX magnetic bearing controller is used to provide active control of the AMB. The controller is programmed with MBScope 2000^{TM} software. It is a highly graphical interface that allows for researchers to access system parameters such as current and position. Controller information such as proportional gain, derivative gain integral gain, notch filter, and low pass filter information is sent from an external computer that equipped with MBScope 2000^{TM} to the controller through a communication cable. Two types of sensors are used in this experiment to monitor position change of the rotor. One is a pair of eddy current position probes located near the disk, oriented vertically and horizontally. Data from these probes are collected using an ADRE 408 DSPi (Dynamic Signal Processing Instrument) and a computer equipped with ADRE software. The other is a pair of variable reluctance probes located on a sensor ring that is built into the AMB. The major dimensions and component layout of the experimental system with sensor

locations indicated is shown in Figure 2.2, a block diagram for the system layout with all data acquisition equipment involved is shown in Figure 2.3:

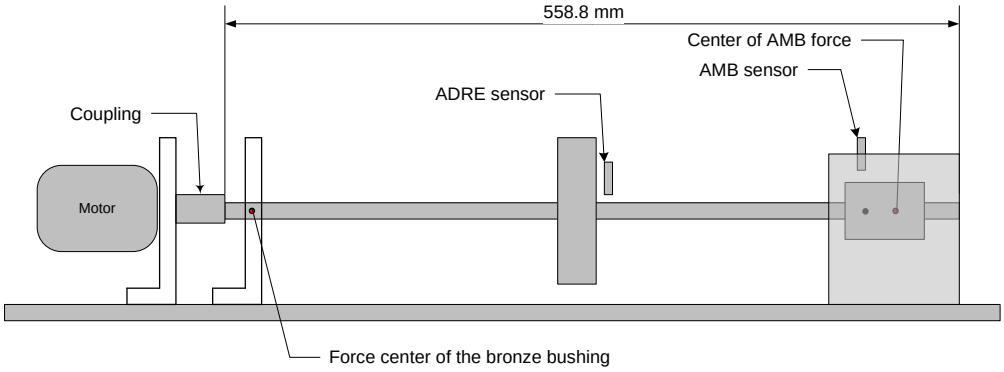

Figure 2. 2 Experimental system layout

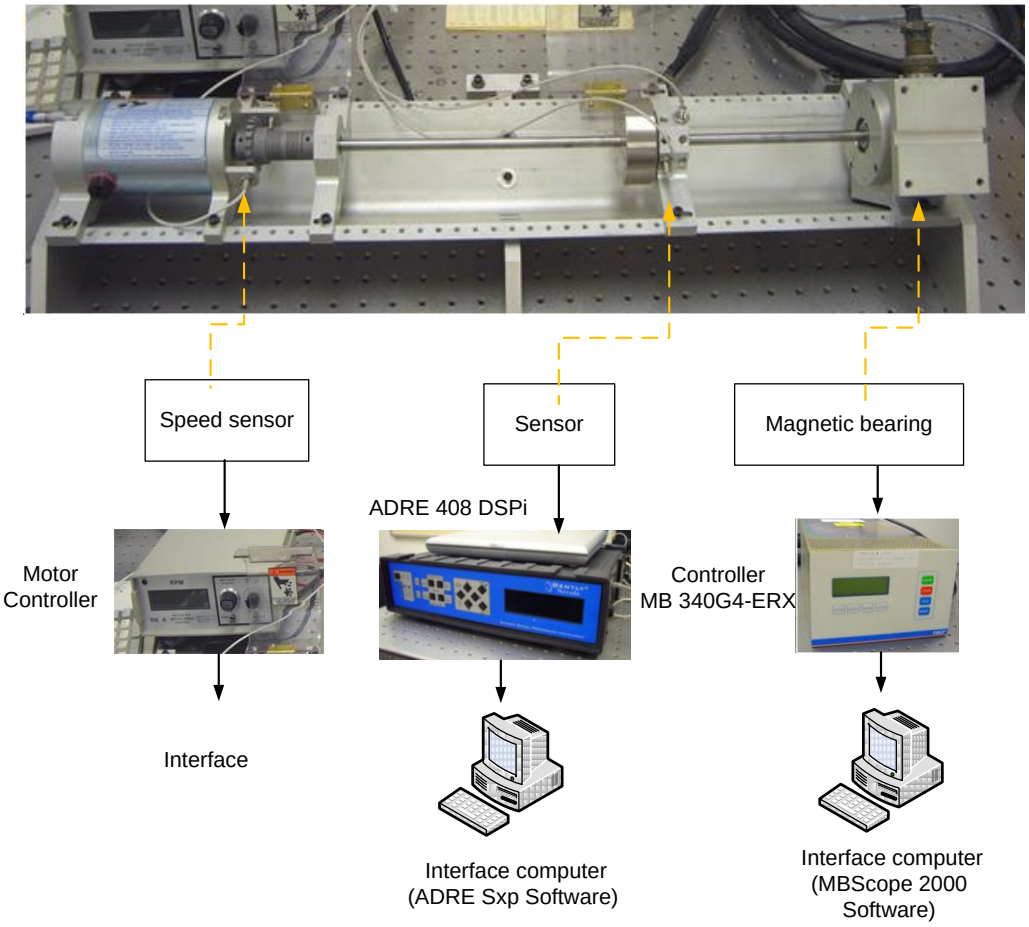

Figure 2. 3 Experimental system block diagram

2.2 The Rotor

The rotor used in this experiment consists of a shaft, a disk, and an AMB rotor. The shaft has a length of 558.8 mm and a diameter of 10 mm. The disk mounted on the shaft has a weight of 0.83 kg, a diameter of 76.2 mm, and a thickness of 25.4 mm. The AMB rotor is part of the active magnetic bearing used to levitate the shaft. Major dimensions of the rotor bearing system and properties of components are shown in Figure 2.4 and Table I respectively.

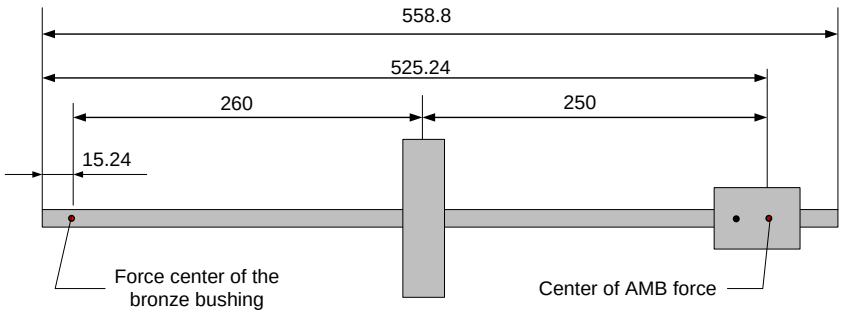

Figure 2. 4 Major dimensions of the rotor assembly with an AMB rotor and a disk (in millimeters)

Table I Masses and moments of inertia for the rotor components

Component	Length	Diameter	Mass	Polar moment of inertia	Transverse moment of inertia
	(mm)	(mm)	(kg)	(kg-m^2)	(kg-m^2)
Shaft	558.8	10.0	0.346	10.40	2162.94
Disk	25.4	76.2	0.830	1447.26	107.19
MB rotor	47.8	34.3	0.246	86.88	71.49

2.3 The Bushing

A bushing is a kind of plain bearing that consists of only a bearing surface with no rolling elements, explained by Shigley [2006]. There are advantages such as high sliding velocity for rotating parts, no external lubrication needed, maintenance-free during the life of the bushing, easily replaceable when needed.

Figure 2.5 shows the bronze bushing that is used in the experiment. It is used to support the motor side of the shaft while allowing the shaft to rotate. The bushing is manufactured by Bently Nevada Corp.. This solid bronze bushing has an inner race diameter of 10 mm, the supporting stiffness provided by the manufacturer is 175 $\frac{KN}{m}$ and 148 $\frac{KN}{m}$ in horizontal and vertical directions respectively, damping ratio for the bushing are 175 $\frac{N\text{-}s}{m}$ and 148 $\frac{N\text{-}s}{m}$ horizontally and vertically.

Figure 2. 5 Solid bronze bushing

2.4 The Active Magnetic Bearing

AMBs differ from normal bearings because they can support a load by magnetic levitation. They are becoming more and more popular in both industry and research disciplines for their numerous advantages over conventional bearings, summarized below:

- Allow for no contact, eliminating wear and the need for lubricant in the system
- Allow for rotating machine part at high speeds
- Provide active control for the bearing and can realize active vibration control, along with tunable stiffness and damping.
- Lower maintenance cost and longer life time for the machine due to lack of mechanical wear
- Better performance can be achieved since the position of the rotor is read by a sensor signal within the control loop

However, there are also drawbacks for AMBs, such as: low static load capacity, possible instability (especially for a flexible rotor system), cost due to its complexity in structure and manufacturing. Also, AMBs may cause difficulty in implementation and technical supervision because magnetic bearings are still a relatively new technology as compared to conventional bearings.

The active magnetic radial bearing used in this experiment consists of a touchdown bearing, a radial stator, a radial rotor, a radial position sensor ring, and AMB housing. The stator and the radial rotor are used to levitate the shaft while the sensor ring monitors the rotor radial position. The touchdown bearing, sometimes called the backup bearing or auxiliary bearing, has a smaller inner race gap than the AMB radial rotor. Thus, the touchdown bearing can serve as a support for the shaft in case of a system power failure or in the case that the AMB's not being in activation. Below, Figure 2.6 shows the components in a radial active magnetic bearing.

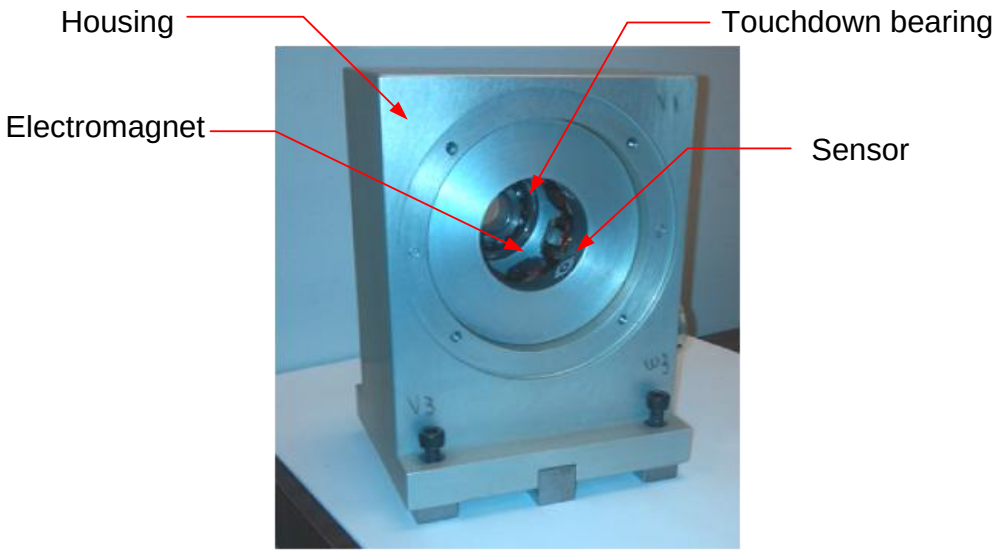

Figure 2. 6 Radial AMB components

Basic usage for an active magnetic bearing is to suspend a ferromagnetic mass using an electromagnet. An actively controlled electromagnetic force is the principle mechanism used for stable levitation. Figure 2.7 explains this function in a simplified schematic.

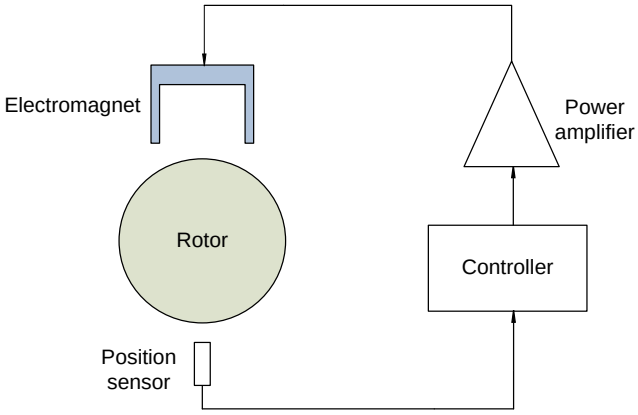

Figure 2. 7 Basic function diagram of an active magnetic bearing

As the figure shows, the position sensor measures the displacement of the rotor by its relative distance from the sensor. Next, the controller generates a control signal from this displacement, finally, the power amplifier transfers the control signal to a control current and sends it to the electromagnet. In the sequence, the electromagnet generates more or less magnetic force to drive the rotor to remain at the desired position. A more detailed one-axis control theory in an AMB is shown in Figure 2.8.

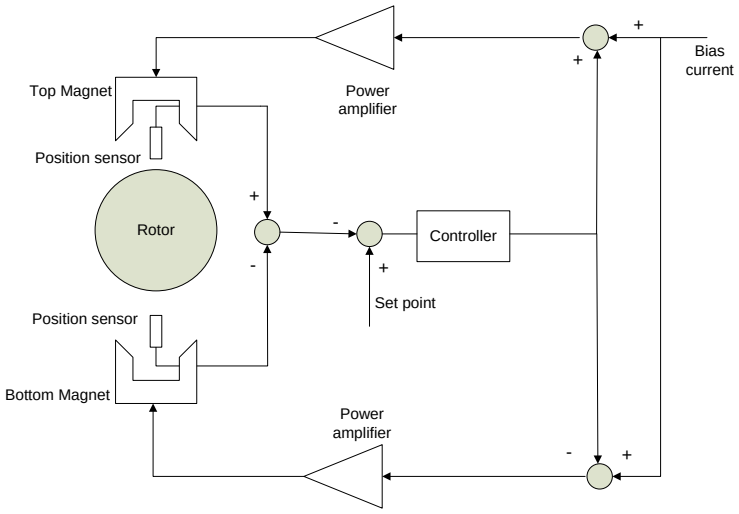

Figure 2. 8 One-axis differential control scheme for the active magnetic bearing

As is shown in Figure 2.8, the active magnetic bearing system consists of a pair of magnetic coils, sensors, power amplifiers and one controller. In order for the AMBs to create stable levitation of the rotor, the closed-loop control algorithm is implemented. Therefore, any change in a rotor position will result in a change of coil currents. Initially, bias current with a constant value is applied to top and bottom coils. Rotor position is changed when a control current is added to the bias current in one coil and subtracted in the opposite coil. Since configuration of the electromagnets is identical for both vertical

and horizontal planes, with planes mutually perpendicular, the same control principle applies to both.

The experiment uses one AMB to realize one rotor end levitation. The radial AMB bearing has two perpendicular control axes, i.e. X and Y for the experimental test rig. With the AMB housing sitting on the V-base as is shown in the following figure, the actual control axis orientation is one horizontal and the other vertical.

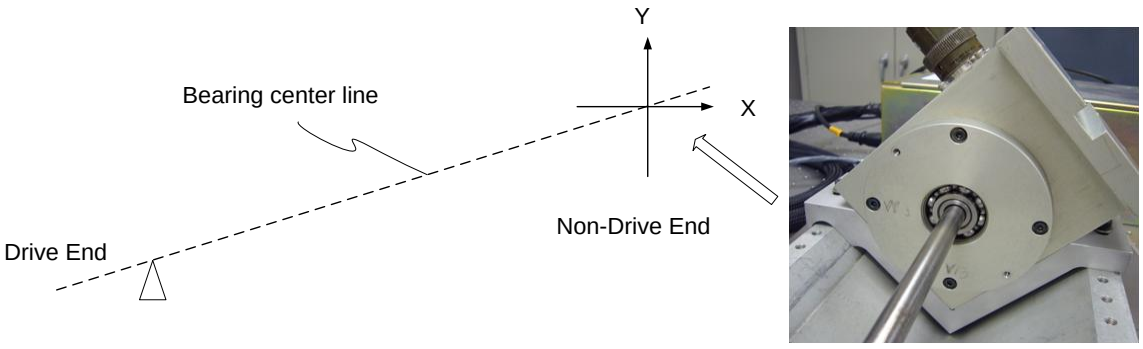

Figure 2. 9 Magnetic bearing axis identification

Electromagnetic forces are applied along the two axes and rotor position is controlled by these radial forces from the AMB. This magnetic bearing actuator force is generated by a pair of opposed magnets which provide forces in either the positive or negative direction. As a consequence, the total force generated is:

$$\overline{F} = \frac{\mu_0 N^2 A_g}{4}\left(\frac{(I_b + I_c)^2}{(g_0 - x)^2} - \frac{(I_b - I_c)^2}{(g_0 + x)^2}\right)\cos\alpha \qquad (2.1)$$

Where $(I_b + I_c)$ and $(I_b - I_c)$ are current of the top and bottom coils, respectively. The variable I_b is the bias current, I_c is the control current, α is the Angle of active

magnetic bearing pole face, g_0 is the effective gap distance between the rotor and the magnet when x=0, $\mu_0 N^2 A_g$ is defined as a whole as the force calibration factor, and x is the displacement of the rotor in X direction. An equivalent equation applies in the Y direction. Although Equation (2.1) shows that the forces acting on the rotor are nonlinear, the equation can be linearized at a set point for control purposes. The force generated by the electromagnet when expressed as a function of displacement and control current, follows a single linearized equation around the operating point:

$$\overline{F} = -K_x x + K_i I_c \tag{2.2}$$

Where $\overline{F}$ is the force generated from the AMB, x is the position relative to the set point, I_c is the control current, and K_x and K_i are position stiffness and current stiffness respectively. K_i and K_x are defined by taking partial derivatives:

$$\frac{\partial \overline{F}}{\partial I_c} = \frac{\mu_0 N^2 A_g \cos\alpha}{4 {g_0}^2}(2(I_b + I_c) - 2(I_b - I_c)(-1)) \tag{2.3}$$

$$-\frac{\partial \overline{F}}{\partial x} = -\frac{\mu_0 N^2 A_g \cos\alpha}{4 {g_0}^2}\left((-2)\frac{(I_b + I_c)^2}{(g_0 - x)^3}(-1) - (-2)\frac{(I_b - I_c)^2}{(g_0 + x)^3}(+1)\right) \tag{2.4}$$

The current stiffness increases in proportion to bias current, and inversely with gap squared. The position stiffness is negative and is proportional to bias current and inversely proportional to gap. When at the set point, $x = 0$, and the resulting control current $I_c = 0$, this condition applies if the actuator has two poles. Then the open-loop stiffness is studied by Maslen [2000], has current and position stiffness given by:

$$K_i = \frac{\mu_0 N^2 I_b A_g}{g_0^{\,2}} \cos\alpha \tag{2.5}$$

$$K_x = -\frac{\mu_0 N^2 I_b^{\,2} A_g}{g_0^{\,3}} \cos\alpha \tag{2.6}$$

The following figure shows a general control loop using linearization assumptions:

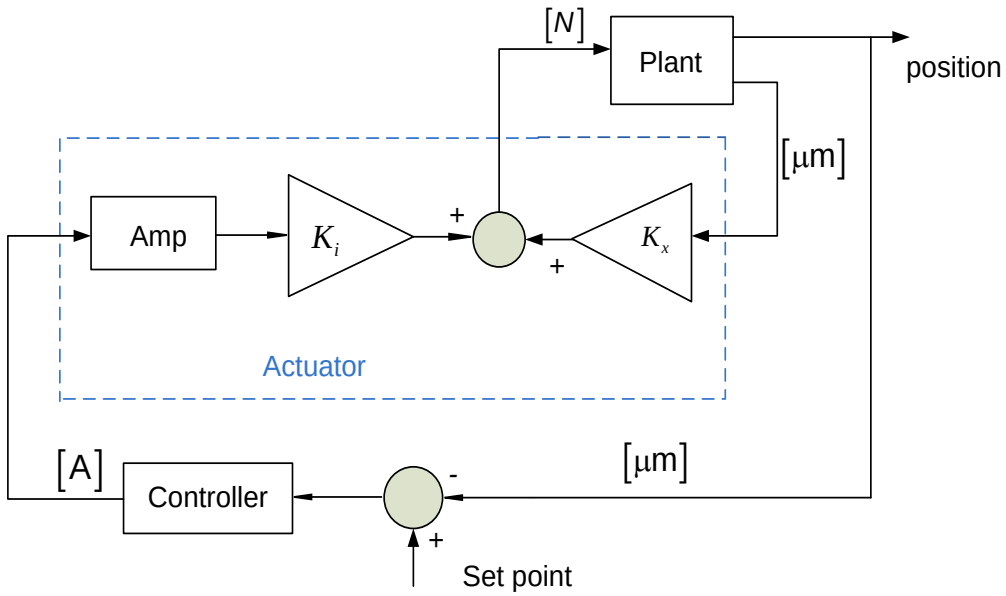

Figure 2. 10 Linear expression of the AMB in feedback control loop block diagram

The following table shows the meanings to each parameter that appears in the Equation (2.5) and (2.6), along with values corresponding to the AMB used in the experiment.

Table II Parameters for calculating K_i and K_x

Parameter	Symbol	Values	Unit
Number of windings in an active magnetic bearing coil	N	228	NA
Permeability of a vacuum	μ_0	$4\pi\times10^{-7}$	$\frac{\mathrm{H}}{\mathrm{m}}$
Angle of active magnetic bearing pole face	α	$\frac{\pi}{8}$	rad
Bias current	I_b	0.5	A
Area of active magnetic bearing pole face	A_g	6.074×10^{7}	$\mu\mathrm{m}^2$
Effective gap between of an active magnetic bearing	g_0	401.55	μm

When these parameter values are placed in Equation (2.5) and (2.6), current stiffness and position stiffness yield the following values:

$$K_i = \frac{\mu_0 N^2 I_b A \cos\alpha}{g_0^2} = 11.74\ \frac{\mathrm{N}}{\mathrm{A}} \tag{2.7}$$

$$K_x = \frac{-\mu_0 N^2 {I_b}^2 A \cos\alpha}{g_0^3} = -2.1\times10^4\ \frac{\mathrm{N}}{\mathrm{m}} \tag{2.8}$$

2.5 Open-Loop System Identification

The system's open-loop transfer function is found by using the experimental test rig. The experiment is done using MBScope Analyzer tool by injecting a harmonic current to the AMB and recording the amplitude response over a range of frequencies. A sinusoidal

current with amplitude of 0.05 A was injected to the AMB in both X and Y axes, one axis at a time. The block diagram illustrating the process is shown in figure as follows:

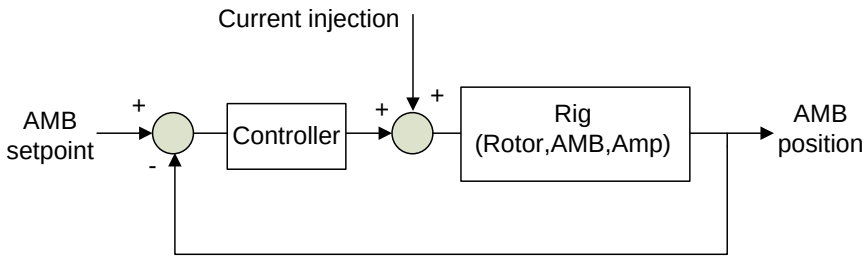

Figure 2. 11 Block diagram for system open-loop identification

The transfer function identification of the open-loop system refers to the system transfer function without controller. As is shown in Figure 2.11, the injection is added to the control current and the open loop transfer function can be found from the total current going into the rig to the AMB position output. Figure 2.12 and Figure 2.13 below shows the experimental results for open-loop system identification in horizontal and vertical directions respectively.

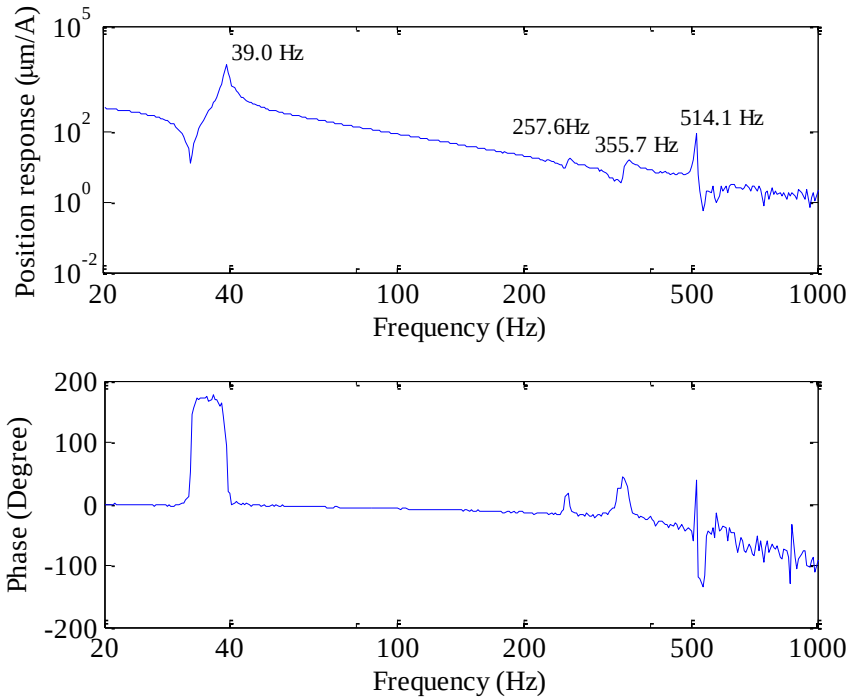

Figure 2. 12 Experimental frequency response of the open-loop system on horizontal axis

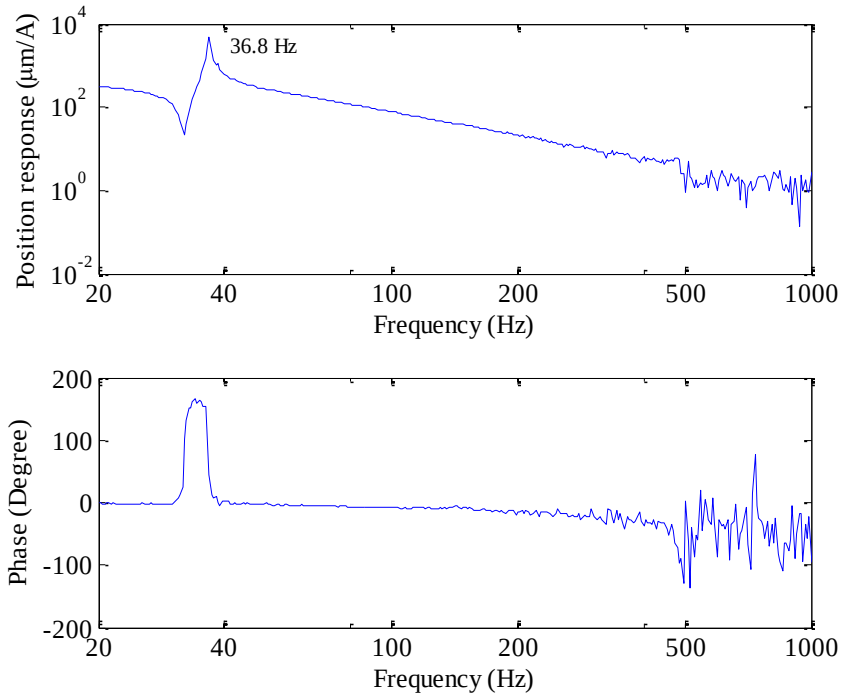

Figure 2. 13 Experimental frequency response of the open-loop system on vertical axis

As one can read from the figures above, the natural frequencies of the open-loop system in the horizontal axis occurred at 39.0 Hz, 257.6 Hz, 355.7 Hz and 514.1 Hz, while in the vertical direction only one at 36.8 Hz can be seen.

CHAPTER III

MODELING OF THE ROTOR BEARING SYSTEM

3.1 Introduction

In this chapter, two models of the open-loop experimental test rig are established. Both models include the amplifiers, the magnetic bearing, the bushing and an expression of the rotor. The first model in Section 3.2 is made using approximate analytical method, which is a three mass-spring-damper system. The parameters of the models are derived from the simplifications of the geometry from the test rig. This simple method is expected to be able to be applied quickly without a rotordynamic expertise. The second model in Section 3.3 is made by discretize the geometry of the rotor and then expressing the sections as finite elements. This method is more time-consuming but it is more detailed expression of the dynamics of the flexible rotor.

3.2 Approximate Analytical Model

A Jeffcott rotor model is shown in Figure 3.1. It consists of a massless flexible shaft and a rigid disk mounted on the middle of the shaft (bearing mid span) with rigid bearing supports.

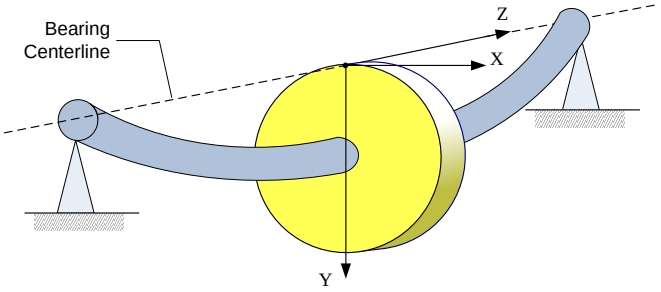

Figure 3. 1 Jeffcott rotor with shaft bending due to weight of the disk

The equation of motion for the disk is derived from Newton's Second Law:

$$\mathbf{F} = m\mathbf{a} \tag{3.1}$$

$$\begin{Bmatrix} F_x \\ F_y \end{Bmatrix} = m \begin{Bmatrix} \ddot{x} \\ \ddot{y} \end{Bmatrix} \tag{3.2}$$

Kirk studied the critical speed and forced response solutions for an active magnetic bearing using an extended Jeffcott rotor system. A six degree-of-freedom model was developed by extending the original Jeffcott model to include bearing stiffness, damping, and journal mass. By looking at only the Y-Z plane, using the property of symmetry, the system can be reduced to a two degree-of-freedom. Figure 3.2 (a) and Figure 3.2 (b) below shows an extended Jeffcott rotor model and its conversion configuration to a two degree-of-freedom model.

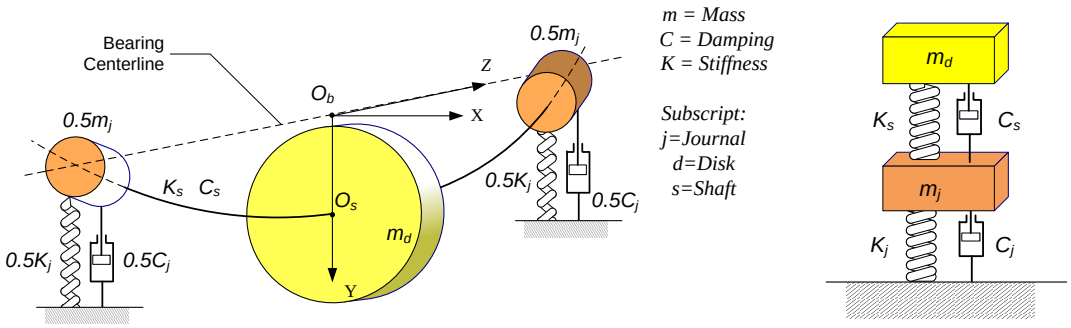

Figure 3. 2 (a) Extended Jeffcott rotor with lumped mass, (b) Equivalent two-mass system

Sometimes, models are simplified to represent particular characters and features of a system. However, there is limited application to the simplified model compared to the real one. All simplified models are based on assumptions that are used to derive the model. One advantage of simplifying a model is the problem can be easily understood by making simple equations. In this section, an approximate analytical model will be introduced. The simplified three-mass analytical model which is referred to as the approximate analytical model is finally presented by a mathematical representation. The ideas used in the extended Jeffcott rotor are applied to the system of interest in the study. The assumptions of symmetry however do not hold, therefore, a non-symmetric model will be introduced in the next section.

3.2.1 Description of the Approximate Analytical Model

The rotor bearing system is simplified to a lumped three-mass configuration so as to represent the approximate analytical model in this section. There are three point-masses at three locations along the shaft that approximately represent the mass for the real rotor

bearing system. The mass of the shaft, mass of the disk, and mass of the AMB rotor are the main concerns of mass distribution for the system. In the model, mass of the shaft is distributed evenly on to the three concentrated masses. The disk mass is assumed lumped at the mass center. The AMB rotor mass is assumed lumped at one side. The total shaft mass is divided by four with one fourth added to the left, one fourth added to the right, and two fourth at the center. With the establishment of this simplified three-mass analytical model, system properties such as transfer function and natural frequencies can be studied.

This approximate analytical model is similar to Kirk's extended Jeffcott rotor model, which converts a rotor bearing system to a three-mass model with lumped masses on two bearing locations and the disk location, and assuming the shaft is massless. The configuration of the three-mass analytical model used fully represents the bushing and the AMB and is shown in the following Figure 3.3:

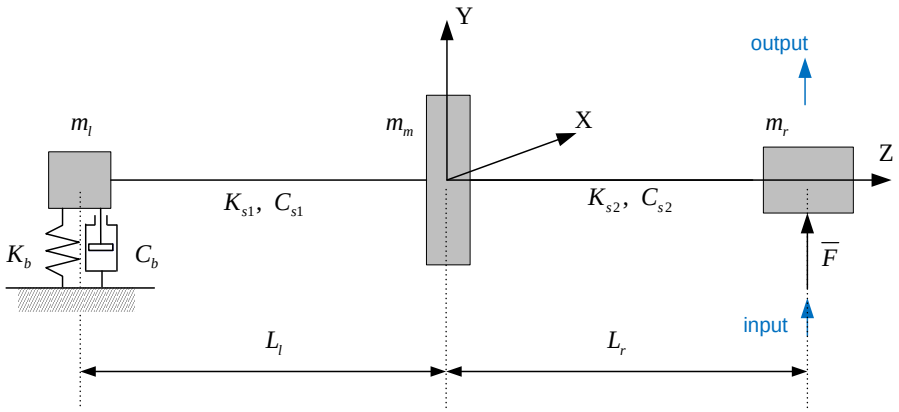

Figure 3. 3 Approximate analytical model of the system including rotor, bushing and AMB

The variables m_l, m_m and m_r are the lumped mass on the left-end, near the center, on the right-end respectively, K_b and C_b are the stiffness and damping of the bushing,

K_{s1}, K_{s2} are calculated stiffness of the flexible shaft on the left and on the right, likewise, C_{s1}, C_{s2} are the damping for the two sides of the shaft. L_l and L_r are the length of the left segment of the shaft and right segment of the shaft respectively.

Some features that the three-mass analytical model has are listed as follows:

- The shaft mass is distributed evenly on to three lumped mass;
- The disk is mounted on a specific location near the mid span along the shaft;
- The left-lumped mass m_l is supported by bronze bushing with manufacture provided stiffness and damping; the right-lumped mass m_r is supported by magnetic force produced by the active magnetic bearing.
- Three concentrated masses are located at three mass centers and are connected by the flexible shaft which has stiffness.
- Shaft stiffness of the two segments which occur between the masses is calculated according to the beam deflection theory.
- The system has one force input from the AMB, and one displacement output at the same location.

Since the right-end mass is suspended by the linearized AMB force as studied in the previous chapter, it is equivalent to say that the right-end mass is supporting by a spring with the stiffness K_x, along with another force proportional to the control current according to K_i from the AMB. The configuration of this three-mass analytical model is shown in Figure 3.4:

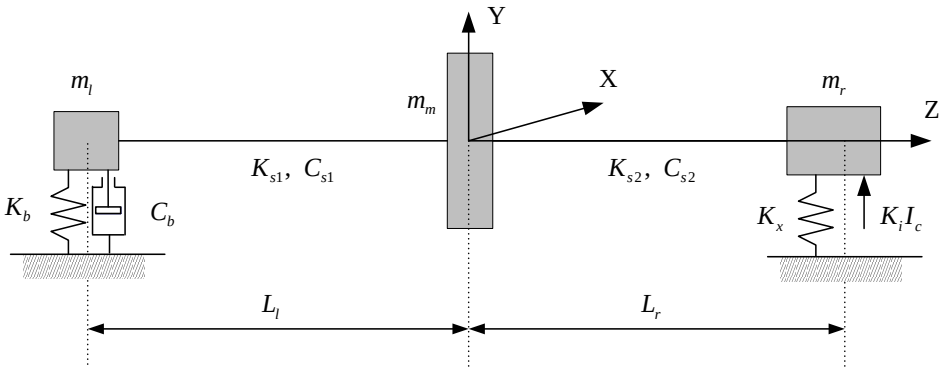

Figure 3. 4 Approximate analytical model with linearized AMB force

3.2.2 Equations of Motion of the Simplified Rotor System

In order to analyze the dynamics of the system, equations of motion for the system are derived based on Newton's Second Law. The overall equations of motion expressed in matrix form for vertical and horizontal planes yields:

$$\mathbf{M}\ddot{\mathbf{q}} + \mathbf{C}\dot{\mathbf{q}} + \mathbf{K}\mathbf{q} = \mathbf{F} \tag{3.3}$$

Where $\mathbf{F}$ denotes the system external forces vector, such as unbalance forces and $\mathbf{q}$ is the position vector for the three masses in X and Y planes. **M, C** and **K** are the mass matrix, damping matrix and stiffness matrix for the model respectively. Summing forces on each mass of the model, equations of motion respectively to X-Z plane and Y-Z plane can be written as follows:

$$\begin{aligned}
&m_l\ddot{x}_l + K_b x_l - K_{s1}(x_m - x_l) + C_b\dot{x}_l - C_{s1}(\dot{x}_m - \dot{x}_l) = 0 \\
&m_m\ddot{x}_m + K_{s1}(x_m - x_l) + K_{s2}(x_m - x_r) + C_{s1}(\dot{x}_m - \dot{x}_l) + C_{s2}(\dot{x}_m - \dot{x}_r) = 0 \\
&m_r\ddot{x}_r + K_x x_r - K_{s2}(x_m - x_r) = F_x
\end{aligned} \tag{3.4}$$

$$
\begin{aligned}
&m_l\ddot{y}_l + K_b y_l - K_{s1}(y_m - y_l) + C_b\dot{y}_l - C_{s1}(\dot{y}_m - \dot{y}_l) = -m_l g \\
&m_m\ddot{y}_m + K_{s1}(y_m - y_l) + K_{s2}(y_m - y_r) + C_{s1}(\dot{y}_m - \dot{y}_l) + C_{s2}(\dot{y}_m - \dot{y}_r) = -m_m g \\
&m_r\ddot{y}_r + K_x y_r - K_{s2}(y_m - y_r) = F_y - m_r g
\end{aligned} \tag{3.5}
$$

Where F_x and F_y are the forces from the active magnetic bearing horizontally and vertically. To account for the presence of the gravity force, the AMB force in the vertical direction has to overcome weight to levitate the system. While on the horizontal plane, no additional force is needed. Rewrite and arrange Equation (3.4) in the horizontal plane to a matrix form yields:

$$
\begin{bmatrix} m_l & 0 & 0 \\ 0 & m_m & 0 \\ 0 & 0 & m_r \end{bmatrix}\begin{bmatrix} \ddot{x}_l^2 \\ \ddot{x}_m^2 \\ \ddot{x}_r^2 \end{bmatrix} + \begin{bmatrix} K_b + K_{s1} & -K_{s1} & 0 \\ -K_{s1} & K_{s1} + K_{s2} & -K_{s2} \\ 0 & -K_{s2} & K_x + K_{s2} \end{bmatrix}\begin{bmatrix} x_l \\ x_m \\ x_r \end{bmatrix} + \begin{bmatrix} C_b + C_{s1} & -C_{s1} & 0 \\ -C_{s1} & C_{s1} + C_{s2} & -C_{s2} \\ 0 & -C_{s2} & C_{s2} \end{bmatrix}\begin{bmatrix} \dot{x}_l \\ \dot{x}_m \\ \dot{x}_r \end{bmatrix} = \begin{bmatrix} 0 \\ 0 \\ F_x \end{bmatrix} \tag{3.6}
$$

The state vector on the horizontal plane can be defined as : $\mathbf{x} = [x_l \; x_m \; x_r \dot{x}_l \; \dot{x}_m \dot{x}_r]^T$. Then Equation (3.4) can be written in state-space representation form as follows:

$$
\dot{\mathbf{x}} = \begin{bmatrix} \mathbf{0} & \mathbf{I} \\ \mathbf{-M^{-1}K} & \mathbf{-M^{-1}D} \end{bmatrix}\mathbf{x} + \begin{bmatrix} \mathbf{0} \\ \mathbf{M^{-1}} \end{bmatrix} F_x \tag{3.7}
$$

$$
\dot{\mathbf{x}} = \begin{bmatrix} 0 & 0 & 0 & 1 & 0 & 0 \\ 0 & 0 & 0 & 0 & 1 & 0 \\ 0 & 0 & 0 & 0 & 0 & 1 \\ -\dfrac{K_b + k_{s1}}{m_l} & \dfrac{K_{s1}}{m_l} & 0 & -\dfrac{C_b + C_{s1}}{m_l} & \dfrac{C_{s1}}{m_l} & 0 \\ \dfrac{K_{s1}}{m_m} & -\dfrac{K_{s1} + K_{s2}}{m_m} & \dfrac{K_{s2}}{m_m} & \dfrac{C_{s1}}{m_m} & -\dfrac{C_{s1} + C_{s2}}{m_m} & \dfrac{C_{s2}}{m_m} \\ 0 & \dfrac{K_{s2}}{m_r} & -\dfrac{K_x + K_{s2}}{m_r} & 0 & \dfrac{C_{s2}}{m_r} & -\dfrac{C_{s2}}{m_r} \end{bmatrix}\mathbf{x} + \begin{bmatrix} 0 \\ 0 \\ 0 \\ 0 \\ 0 \\ -\dfrac{1}{m_r} \end{bmatrix} F_x \tag{3.8}
$$

$$
\mathbf{y} = [0 \quad 0 \quad 1 \quad 0 \quad 0 \quad 0]\mathbf{x}
$$

Then, the state-space matrixes for the supported three-mass analytical model yields,

$$\mathbf{A_s}=\begin{bmatrix} 0 & 0 & 0 & 1 & 0 & 0 \\ 0 & 0 & 0 & 0 & 1 & 0 \\ 0 & 0 & 0 & 0 & 0 & 1 \\ -\frac{K_b+k_{s1}}{m_l} & \frac{K_{s1}}{m_l} & 0 & -\frac{C_b+C_{s1}}{m_l} & \frac{C_{s1}}{m_l} & 0 \\ \frac{K_{s1}}{m_m} & -\frac{K_{s1}+K_{s2}}{m_m} & \frac{K_{s2}}{m_m} & \frac{C_{s1}}{m_m} & -\frac{C_{s1}+C_{s2}}{m_m} & \frac{C_{s2}}{m_m} \\ 0 & \frac{K_{s2}}{m_r} & -\frac{K_x+K_{s2}}{m_r} & 0 & \frac{C_{s2}}{m_r} & -\frac{C_{s2}}{m_r} \end{bmatrix}, \mathbf{B_s}=\begin{bmatrix} 0 \\ 0 \\ 0 \\ 0 \\ 0 \\ -\frac{1}{m_r} \end{bmatrix}, \quad (3.9)$$

$$\mathbf{C_s}=[0 \quad 0 \quad 1 \quad 0 \quad 0 \quad 0],\ \mathbf{D_s}=[0]$$

The values used for the test rig are shown in Table III:

Table III Parameters of the values of the approximate analytical model

Parameter	Symbol	Value	Unit
Total shaft mass	NA	0.3437	kg
Left lumped mass	m_l	0.0885	kg
Middle lumped mass	m_m	1.0019	kg
Right lumped mass	m_r	0.3294	kg
Left half shaft length	L_l	260×10^{-6}	m
Right half shaft length	L_r	250×10^{-6}	m
Stiffness of the bronze bushing	K_b	1.75×10^{5}	$\frac{N}{m}$
Damping of the bronze bushing	C_b	175	$\frac{N\text{-}s}{m}$
Stiffness of left half the shaft	K_{s1}	2.033×10^{4}	$\frac{N}{m}$
Stiffness of right half the shaft	K_{s2}	2.049×10^{4}	$\frac{N}{m}$
Position stiffness	K_x	-2.1×10^{4}	$\frac{N}{m}$
Current stiffness	K_i	11.74	$\frac{N}{A}$

3.2.3 Open-Loop Model

The open-loop three-mass analytical model introduced in this section has no controller, no feedback, but has other system components associated with the controller. The purpose of making this model is for controller design. Figure 3.5 below shows the open-loop block diagram for the three-mass analytical model.

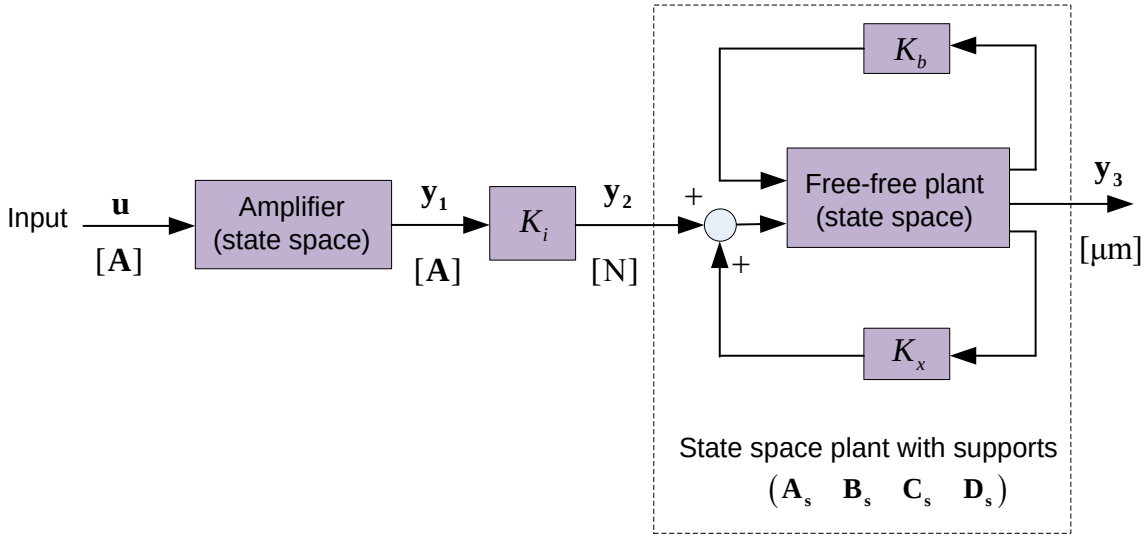

Figure 3. 5 Block diagram of open-loop model with amplifier

The transfer function from output $\mathbf{y_3}$ to input $\mathbf{u}$ should be derived first in order to get the system natural frequencies. As one can see in the figure, an amplifier is in series with the plant. Amplifier output in series with current stiffness K_i is input to the plant. Here the state vector of the amplifier is $\mathbf{x_a}$ and that of the plant is $\mathbf{x}$, $\mathbf{x_{open}}$ is the open-loop plant state vector, y_1 is the output of the amplifier and y_2 is the input to the plant. According to the diagram, derivation from input signal to output signal will be performed as follows:

$$\begin{aligned}\dot{\mathbf{x}}_{\mathbf{a}} &= \mathbf{A}_{\mathbf{amp}}\mathbf{x}_{\mathbf{a}} + \mathbf{B}_{\mathbf{amp}}\mathbf{u} \\ \mathbf{y}_{\mathbf{1}} &= \mathbf{C}_{\mathbf{amp}}\mathbf{x}_{\mathbf{a}} + \mathbf{D}_{\mathbf{amp}}\mathbf{u} \\ \mathbf{y}_{\mathbf{2}} &= K_i\mathbf{y}_{\mathbf{1}} = K_i\mathbf{C}_{\mathbf{amp}}\mathbf{x}_{\mathbf{a}} + K_i\mathbf{D}_{\mathbf{amp}}\mathbf{u}\end{aligned} \tag{3.10}$$

For the plant, state-space representation yields:

$$\begin{aligned}\dot{\mathbf{x}}_{\mathbf{open}} &= \mathbf{A}_{\mathbf{s}}\mathbf{x} + \mathbf{B}_{\mathbf{s}}\mathbf{y}_{\mathbf{2}} = \mathbf{A}_{\mathbf{s}}\mathbf{x} + \mathbf{B}_{\mathbf{s}}\left[\mathbf{C}_{\mathbf{amp}}\mathbf{x}_{\mathbf{a}}K_i + \mathbf{D}_{\mathbf{amp}}\mathbf{u}K_i\right] \\ \mathbf{y}_{\mathbf{3}} &= \mathbf{C}_{\mathbf{s}}\mathbf{x} + \mathbf{D}_{\mathbf{s}}\mathbf{y}_{\mathbf{2}} = \mathbf{C}_{\mathbf{s}}\mathbf{x} + \mathbf{D}_{\mathbf{s}}\left[\mathbf{C}_{\mathbf{amp}}\mathbf{x}_{\mathbf{a}}K_i + \mathbf{D}_{\mathbf{amp}}\mathbf{u}K_i\right]\end{aligned} \tag{3.11}$$

$$\begin{aligned}\dot{\mathbf{x}}_{\mathbf{open}} &= \begin{bmatrix}\dot{\mathbf{x}}_{\mathbf{a}} \\ \dot{\mathbf{x}}\end{bmatrix} = \begin{bmatrix}\mathbf{A}_{\mathbf{amp}} & \mathbf{0} \\ \mathbf{B}_{\mathbf{s}}\mathbf{C}_{\mathbf{amp}}K_i & \mathbf{A}_{\mathbf{s}}\end{bmatrix}\begin{bmatrix}\mathbf{x}_{\mathbf{a}} \\ \mathbf{x}\end{bmatrix} + \begin{bmatrix}\mathbf{D}_{\mathbf{amp}}K_i \\ \mathbf{B}_{\mathbf{amp}}\end{bmatrix}\mathbf{u} \\ \mathbf{y}_{\mathbf{3}} &= \begin{bmatrix}\mathbf{0} & \mathbf{C}_{\mathbf{s}}\end{bmatrix}\begin{bmatrix}\mathbf{x}_{\mathbf{a}} \\ \mathbf{x}\end{bmatrix}\end{aligned} \tag{3.12}$$

The plant matrixes $\mathbf{A}_{\mathbf{s}}, \mathbf{B}_{\mathbf{s}}, \mathbf{C}_{\mathbf{s}}, \mathbf{D}_{\mathbf{s}}$ refers to the state-space matrixes obtained in the previous section, with parameter K_b and K_x included in these matrixes. Then, state-space matrixes for the open-loop three-mass analytical are as follows:

$$\begin{aligned}\mathbf{A}_{\mathbf{open}} &= \begin{bmatrix}\mathbf{A}_{\mathbf{amp}} & \mathbf{0} \\ \mathbf{B}_{\mathbf{s}}\mathbf{C}_{\mathbf{amp}}K_i & \mathbf{A}_{\mathbf{s}}\end{bmatrix} \\ \mathbf{B}_{\mathbf{open}} &= \begin{bmatrix}\mathbf{D}_{\mathbf{amp}}K_i \\ \mathbf{B}_{\mathbf{amp}}\end{bmatrix} \\ \mathbf{C}_{\mathbf{open}} &= \begin{bmatrix}\mathbf{0} & \mathbf{C}_{\mathbf{s}}\end{bmatrix} \\ \mathbf{D}_{\mathbf{open}} &= \mathbf{[0]}\end{aligned} \tag{3.13}$$

Then, the bode plot of the open-loop system is shown in Figure 3.6:

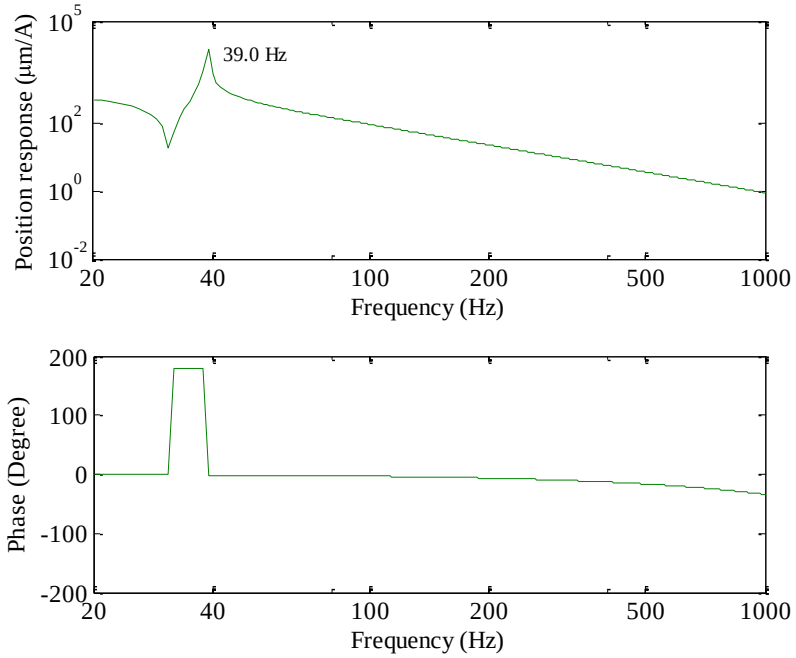

Figure 3. 6 Frequency response of the approximate analytical model in assembled open-loop

In the figure above, a natural frequency can be seen at 39.0 Hz. Compute the eigenvalues of the system, three natural frequencies happens at 0 Hz, 39 Hz and 236.5 Hz.

3.3 Finite Element Analysis Model

3.3.1 Description of the FEA Rotor Model

The finite element approach is used in setting up a detailed model of the real experimental rotor. The beam elements are based on Timoshenko beam theory; beam shear deformation and rotation inertia taken into consideration. The rotor is modeled by 30 elements, the disk and the AMB rotor are lumped at the 14^{th} node and 27^{th} node. The

overall equations of motion for the finite element approach given by Rao [2004], can be expressed as:

$$\mathbf{M}\ddot{\mathbf{q}} + (\mathbf{C} + \Omega\mathbf{G})\dot{\mathbf{q}} + \mathbf{K}\mathbf{q} = \mathbf{F} \tag{3.14}$$

Where **M** is the mass matrix, **C** is the damping matrix, **G** is the gyroscopic matrix and **K** is the stiffness matrix. Ω is the spinning speed of the rotor, **q** is the position vector of each node. However, the finite element model is set up in modal coordinates, where the equations of motion (2.13) can be updated as follows:

$$\mathbf{\Phi}^T\mathbf{M}\mathbf{\Phi}\ddot{\mathbf{q}} + (\mathbf{\Phi}^T\mathbf{C}\mathbf{\Phi} + \Omega\mathbf{\Phi}^T\mathbf{G}\mathbf{\Phi})\dot{\mathbf{q}} + \mathbf{\Phi}^T\mathbf{K}\mathbf{\Phi}\mathbf{q} = \mathbf{\Phi}^T\mathbf{F} \tag{3.15}$$

Where **Φ** is the modal matrix of the rotor. The figure below shows the FEA model of the rotor bearing system with sensor location indicated.

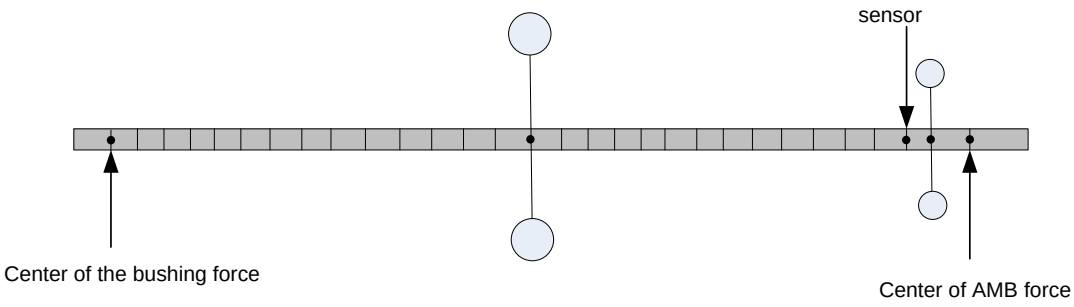

Figure 3. 7 Finite element model of the free rotor with 30 stations.

3.3.2 Free-free Model

A finite element modeling program is used in setting up the FEA mode. This analysis software for magnetic bearing audits was developed by Maslen et. al. [1997]. The finite element program is able to generate state representation for the FEA model. Input parameters to the software include geometry for each FEA beam segment. See Appendix A for detailed information. System analysis such as mode shapes and a Campbell diagram of the free-free (no bearing support) rotor can be generated. Equation (3.15) can be put into state space as follows:

$$\begin{aligned} \dot{\mathbf{x}} &= \left[\mathbf{A}_{\mathbf{ff}} + \Omega\mathbf{G}_{\mathbf{ff}}\right]\mathbf{x} + \mathbf{B}_{\mathbf{ff}}\mathbf{u} \\ \mathbf{y} &= \mathbf{C}_{\mathbf{ff}}\mathbf{x} + \mathbf{D}_{\mathbf{ff}}\mathbf{u} \end{aligned} \tag{3.16}$$

Where $\mathbf{A}_{\mathbf{ff}}$, $\mathbf{B}_{\mathbf{ff}}$, $\mathbf{C}_{\mathbf{ff}}$, and $\mathbf{D}_{\mathbf{ff}}$ are the generated state-space matrixes for the free-free rotor model, $\mathbf{G}_{\mathbf{ff}}$ is the gyroscopic matrix, Ω is the running speed of the rotor.

The Campbell diagram in Figure 3.8 shows the free-free system's natural frequencies as a function of rotor running speed. The gyroscopic effect is taken into account and critical speeds can be read at the intersection of each forward whirl natural frequency line and a synchronous speed line which has a slope of 1.

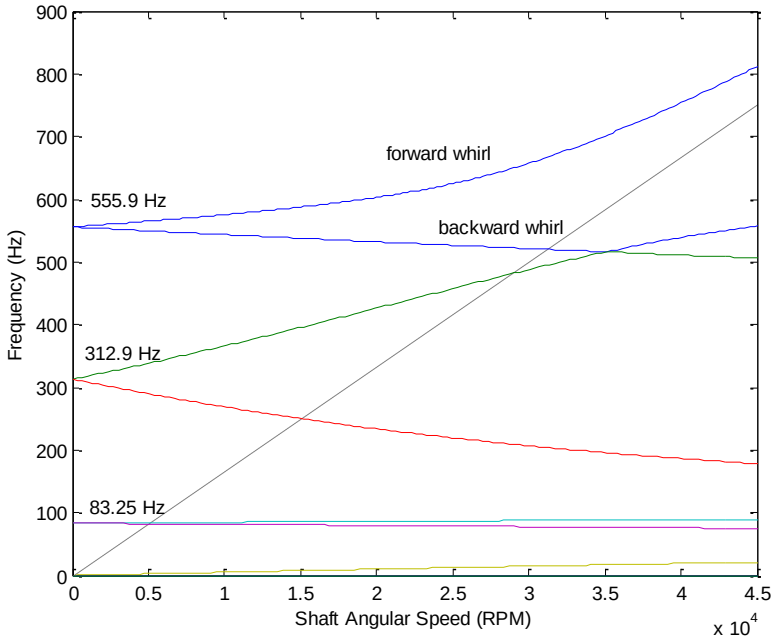

Figure 3. 8 Campbell diagram for the supported FE rotor

As is shown in the figure above, the natural frequencies of the free-free rotor model were found to be rigid body modes at 0 Hz, and three bending modes at 83.25 Hz, 312.9 Hz and 555.9 Hz. The mode shapes corresponding to the natural frequencies that occur at 0 RPM are shown in Figure 3.9 below:

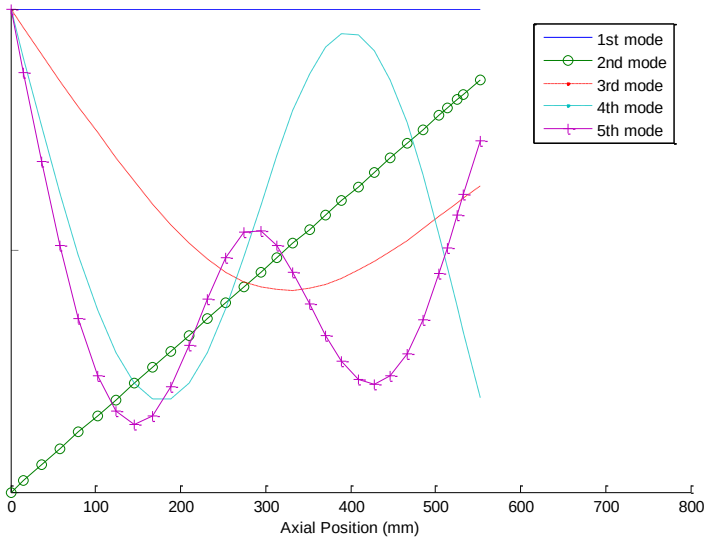

Figure 3. 9 Mode shape of the FE rotor pinned at the bushing node

3.3.3 FEA Rotor Model with Supports

As is described in Section 3.2.3, the three-mass analytical state-space model has an open-loop assembly with bearing stiffness K_b, K_x and K_i considered. Correspondingly in this section, the FEA model will have an open-loop model with all these factor taken into consideration.

With the free-free FEA model set up in the previous section, an easy change can be made upon the model to make it involve bearing stiffness on both ends for the system. A feedback with a gain which is exactly the value of support stiffness is performed at the node where the bearing force is applied. Extracting the displacement at the bearing node, then multiplying by the spring stiffness, results in the supporting force. Then, inject the resultant force to the state-space model of the original free-free rotor.

In one plane of the free-free finite element model, there are three position outputs, bronze bushing location, AMB sensor location, and AMB force center location. A block diagram that shows this feedback process is shown in the following Figure 3.10:

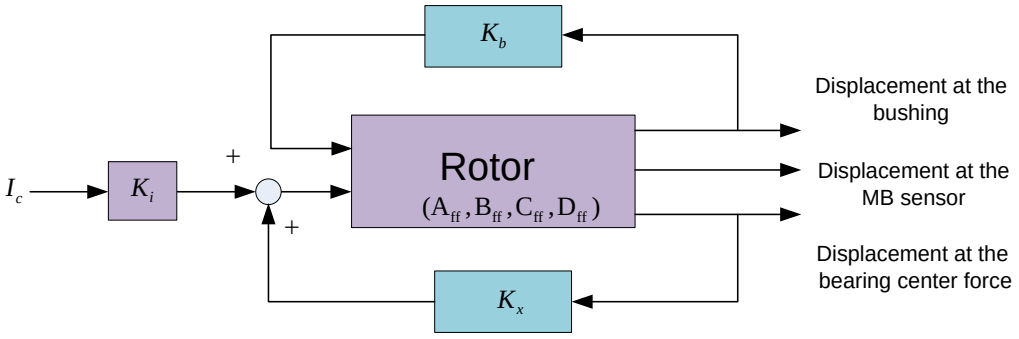

Figure 3. 10 Finite element model with stiffness feedback.

In the above Figure 3.10, the center block is the free-free FEA model. The equivalent rotor bearing model corresponding to the overall block diagram is shown in Figure 3.11:

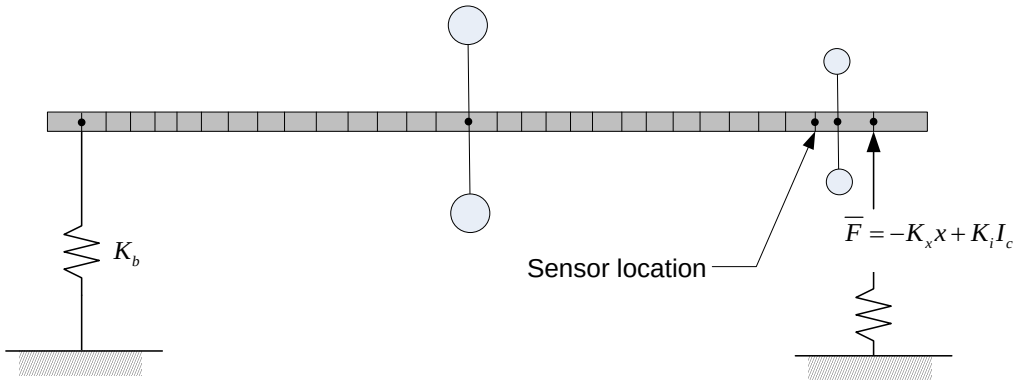

Figure 3. 11 FE rotor with supports.

Defining parameter names of the new stiffness feedback system, the state space representation of the model can be re-written as a new state-space model. Name F_b the force caused by bronze bushing and $\overline{F}$ the force caused by displacement stiffness from the AMB. $\mathbf{C_{b1}}$, $\mathbf{C_{b2}}$ and $\mathbf{C_{b3}}$ are the state-space output matrixes of the bushing, AMB sensor and center of the bearing force respectively. According to the block diagram in Figure 3.10, then new model can be expressed as:

$$\begin{aligned}\dot{\mathbf{x}} &= \mathbf{A}_{\text{ff}}\mathbf{x}+\mathbf{B}_{\mathbf{ff}}\begin{Bmatrix}F_b\\ \overline{F}\end{Bmatrix} = \mathbf{A}_{\text{ff}}\mathbf{x}+\mathbf{B}_{\text{ff}}\begin{Bmatrix}K_b\mathbf{C_{b1}}\mathbf{x}\\ K_x\mathbf{C_{b3}}\mathbf{x}+K_iI_c\end{Bmatrix} \\ &= \left(\mathbf{A}_{\text{ff}}+\mathbf{B}_{\text{ff}}K_b\mathbf{C_{b1}}+\mathbf{B}_{\text{ff}}K_x\mathbf{C_{b3}}\right)\mathbf{x}+\mathbf{B}_{\text{ff}}K_iI_c\end{aligned} \tag{3.17}$$

The same amplifier as is used for the three-mass analytical model is also considered in this FEA model for the open-loop assembly. Utilizing the same principle as in Equation (3.13), the open loop transfer function can be assembled. The frequency response of the transfer function is shown in the following figure:

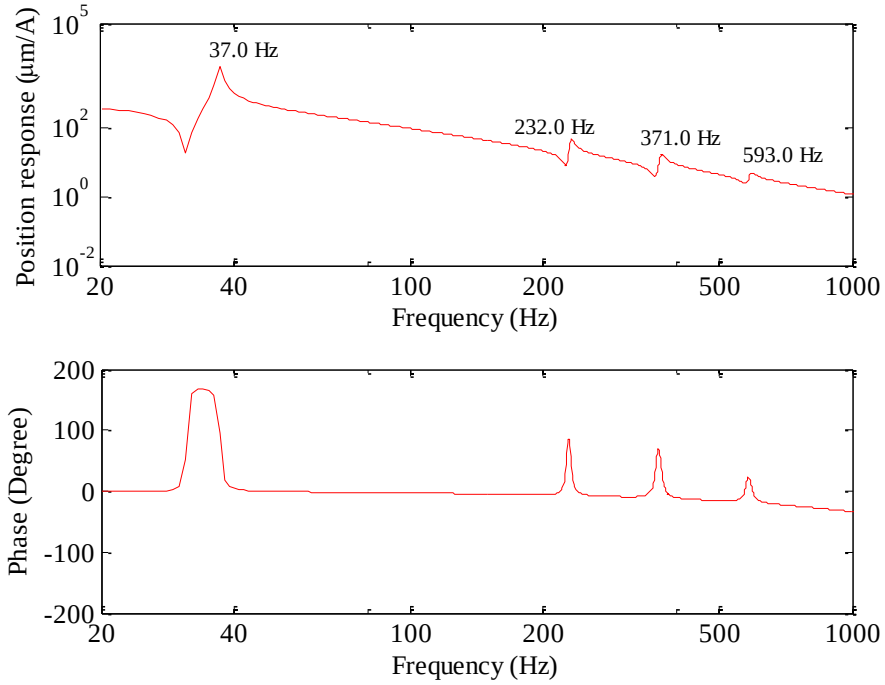

Figure 3. 12 Frequency response of the FEA model in assembled open-loop

Seen from this figure, this FEA open-loop model has natural frequencies at 37.0 Hz, 232.0 Hz, 371.0 Hz and 593.0 Hz.

3.4 Experimental System Identification and Comparison to Both Models

A comparison of the three-mass analytical model and the FEA model will be discussed in this section. It can give the reader an idea on how well the simplified model and the FEA model can represent the real system. System frequency responses for all three transfer functions are compared. It is shown in the following Figure 3.13, that there is a difference in the first natural frequency of the three-mass model and the FEA model. The three-mass model has a higher frequency than the finite element model which is closer to the experimental system. Also, the finite element model reflects the flexible

modes that are seen in the experimental rig. A table shows the critical speeds for the three-mass analytical model, the finite element model and the experimental results respectively.

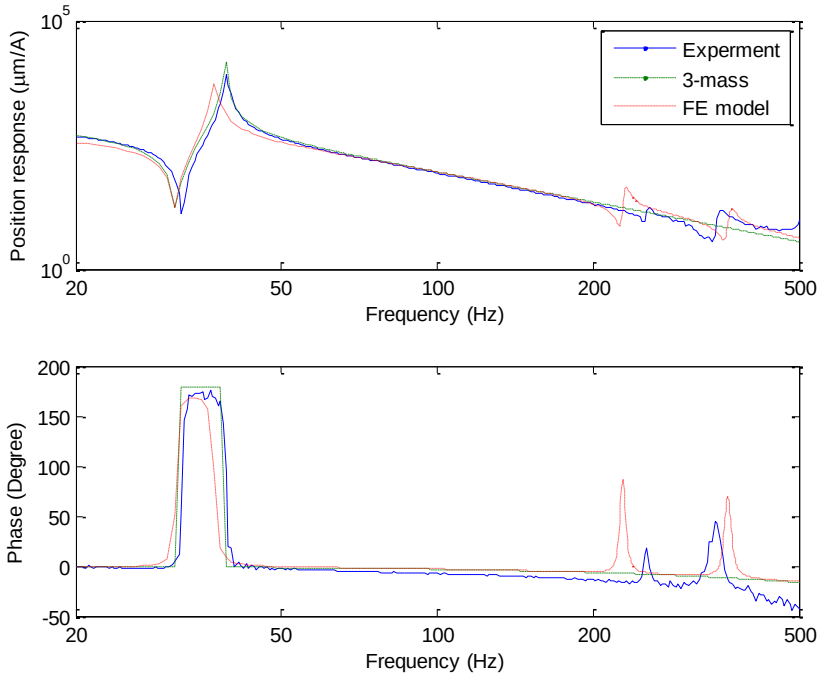

Figure 3. 13 Comparison of the open-loop frequency response of the FEA model, the approximate analytical model and the experimental test rig

Table IV Natural frequencies of the different models

	Natural frequencies (Hz)		
Three-mass analytical	39.0	236.5	
Finite element	37.0	232.0	371.0
Experiment	39.0	257.6	355.7

The results show small differences in static stiffness with the finite element being less stiff than the experimental data. From a broad perspective, the comparison shows agreement between both model and experimental data. The three-mass model has a natural frequency at 236.5 Hz which cannot be seen in this bode plot due to the mode shape and collocation of the actuator and the sensor.

CHAPTER IV

CONTROLLER DESIGN FOR THE ACTIVE MAGNETIC BEARING

4.1 Introduction

As has been previously mentioned, feedback control is required for successful operation of AMBs in a rotor system. In order to design a controller, several requirements have to be met concerning the overall dynamic characteristics of the rotor bearing system. First, the controller must stabilize the system. Second, the controller must be such that the closed loop system achieves certain performance requirements such as rise time, settling time, peak position response, peak current response, stiffness, natural frequency, etc.. And, the controller should be stabilizing and meet performance requirements in the rotor operating speed range, which is to say that there will be external excitation at the rotational speed due to unbalance that must be taken into account. Also, non-collocation of the AMB's sensors and force centers must be dealt with. Because in many AMB designs, the rotor displacement is not measured at the magnetic actuator center but rather some distance beside it because of space constraints, the control engineer is burdened with the problem of non-collocation.

PD control is selected for the current work because it is compatible with hardware in use with most magnetic bearing systems today. The problem then becomes how to select proportional and derivative gains to stabilize the system and best achieve the design goals in a dissimilar bearing configuration. In the section, a cost function minimizing approach similar to LQR but constrained to a local PD solution is used. This technique demonstrates the usefulness of the different modeling methods of interest in this work.

After knowing the whole open–loop model dynamics including a rotor, amplifier, and a linearized magnetic bearing, a controller is added in the system to achieve certain stability and performance requirements. Figure 4.1 below shows a schematic block diagram representation of the components of the open-loop rotor bearing system which has been stabilized with a feed-back controller.

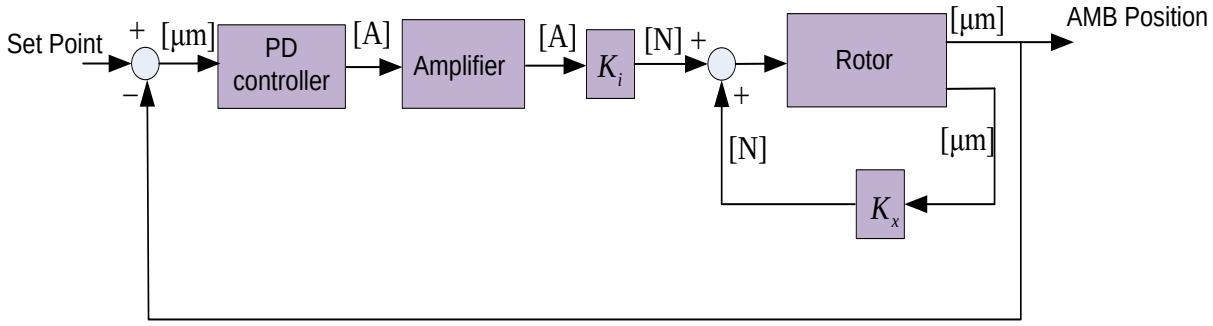

Figure 4. 1 Closed-loop model of the system with controller in feedback.

The idea of this part is to find a control manner that can minimize the system performance measure *J*. In the process of selecting the performance measure, a mathematical expression is found. In other words, this mathematical expression is

derived by translating from the system's physical requirement to a quantified value. The minimized expression indicates the most desirable performance of the system. Kirk [1970] gives a typical performance measure of a minimum control effort problem, $J = \int |u(t)| dt$ where $u(t)$ is the control input vector. In this present rotor bearing control scenario, the performance measure is selected in order to evaluate the vibration and control current of the system. The control input vector $u(t)$ in this case supplies control current $I_c(t)$ to the AMB. But, displacement is also a major performance concern. So, one possible cost function could be:

$$J = \int \left[W_1 x(t)^2 + W_2 I_c(t)^2 \right] dt \tag{4.1}$$

Where W_1 and W_2 are the weighting factors of each term, by changing the values of these factors, one can weight the importance of each part in the expression. The symbol $x(t)$ denotes the time dependent displacement of the rotor. Note that $x(t)$ is the displacement at the position sensors making this method easy to use considering real world operation limits. The weighted terms are squared to avoid returning faulty results when integrating possible negative parts of the function. It is a simple reason exercise to see that without the squaring of those terms the minimum value of J will become negative infinity. It is relatively intuitive to implement a PD controller with this method. For a PD controller, the proportional part is like a spring in a Spring-Mass-Damper system, while the derivative part is like the damper in such system. One can easily find out the displacement and velocity vector using the state-space model that has already been set up with a numerical simulation.

Figure 4.1 shows the form of the rotor bearing system after inserting a PD controller. The system without controller has a state space representation with dynamic matrix: $\mathbf{A}_{\mathbf{open}}$, input matrix: $\mathbf{B}_{\mathbf{open}}$, output matrix: $\mathbf{C}_{\mathbf{open}}$ and no feed through. After incorporating the controller, only dynamic matrix, $\mathbf{A}_{\mathbf{open}}$, changes to:

$$\mathbf{A_c} = \mathbf{A_{open}} - \mathbf{B_{open}}[K_P \quad K_D]\mathbf{C_{open}} \tag{4.2}$$

Where $\mathbf{A_c}$ is the open-loop dynamic matrix with a PD controller closing the loop. In the above equation, matrix$[K_P \quad K_D]$, indicate a set of proportional and derivative gain values that constitute the controller. Then, the cost function of the system performance measure with the PD controller is used to evaluate the system response. The cost function has K_P and K_D related terms, thus, the value that the minimum cost function returns is corresponding to a pair of K_P and K_D combinations, then this pair of K_P and K_D is the optimal controller parameters for the system. Using the same procedure for both finite element model and the approximate analytical model will result in two different PD controllers.

For the cost function, W_1 =1, and W_2=19000 are used. Assuming zero initial conditions and a current impulse disturbance acts on the system, the output response time history is substituted in the expression as displacement $x(t)$. Current $I_c(t)$ can be obtained by multiplying the controller matrix $[K_P \quad K_D]$ and the output vector. Note the output vector has two parts, one corresponding to displacement and the other corresponding to velocity. The equation that demonstrates this process can be expressed as follows:

$$I_c(t) = [K_P \quad K_D]^T \mathbf{Y_{response}} \tag{4.3}$$

Where $\mathbf{Y}_{\mathbf{response}} = [x(t) \quad \dot{x}(t)]^T$ refers to the displacement and velocity response at the sensor. The cost function is updated as:

$$J = \int \left[W_1 x(t)^2 + W_2 (K_p x(t) + K_D \dot{x}(t))^2 \right] dt \tag{4.4}$$

4.2 Controller Design using Each Model

For both the approximate analytical model of the rotor and the FEA model, a proper proportional gain and derivative gain searching area is selected based on realistic values drawn from experience with the test rig. Note that controller total gain K_t should be multiplied by the proportional gain and derivative gain. The proportional gain searching area is from 50 $\frac{\text{A}}{\mu\text{m}}$ to 100 $\frac{\text{A}}{\mu\text{m}}$, and that for derivative gain is from 0.1 $\frac{\text{A-s}}{\mu\text{m}}$ to 0.4 $\frac{\text{A-s}}{\mu\text{m}}$, with a step size of 0.0001 $\frac{\text{A}}{\mu\text{m}}$ and 0.0001 $\frac{\text{A-s}}{\mu\text{m}}$ respectively. The total gain $K_t = 0.0001$. This search range is taken for both models. Figure 4.2 below shows the displacement and control current response of the system to an impulse for a characteristic pair of PD values. The controller gains for this example are K_P =60 $\frac{\text{A}}{\mu\text{m}}$ and K_D =0.35 $\frac{\text{A-s}}{\mu\text{m}}$. This example is a characteristic impulse responses used for controller design. The Matlab command impulse was used with a fixed step size of 0.0001 *s*, and has a simulation time of 0.5 *s*.

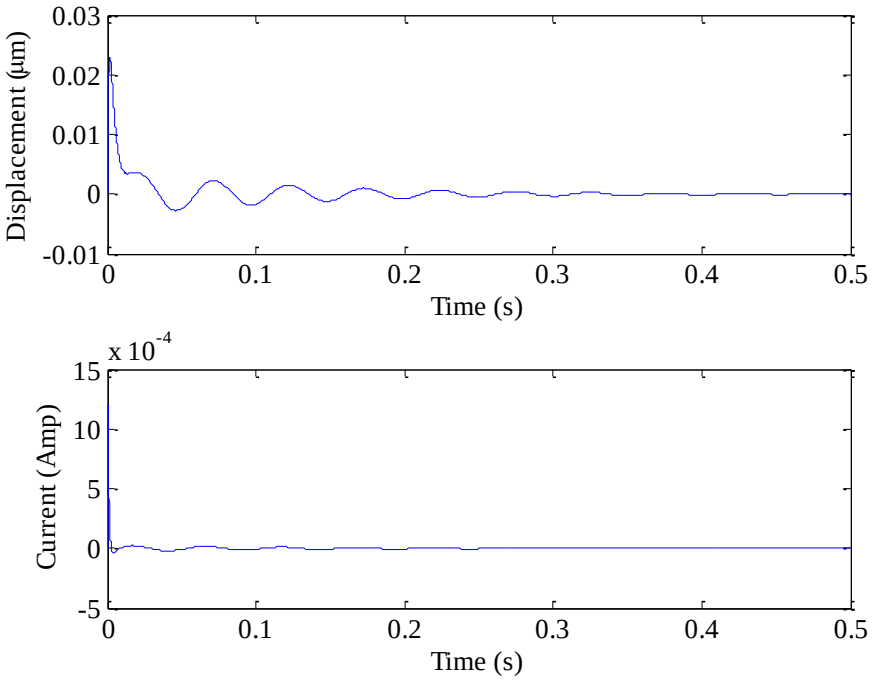

Figure 4. 2 Example in impulse response in the PD controller tuning process.

4.2.1 Initial Controller "A" Design for the Approximate Analytical Model

The aforementioned procedure is performed for the approximate analytical model. Figure 4.3 below shows the cost index with respect to K_P and K_D using the cost function Equation (4.4).

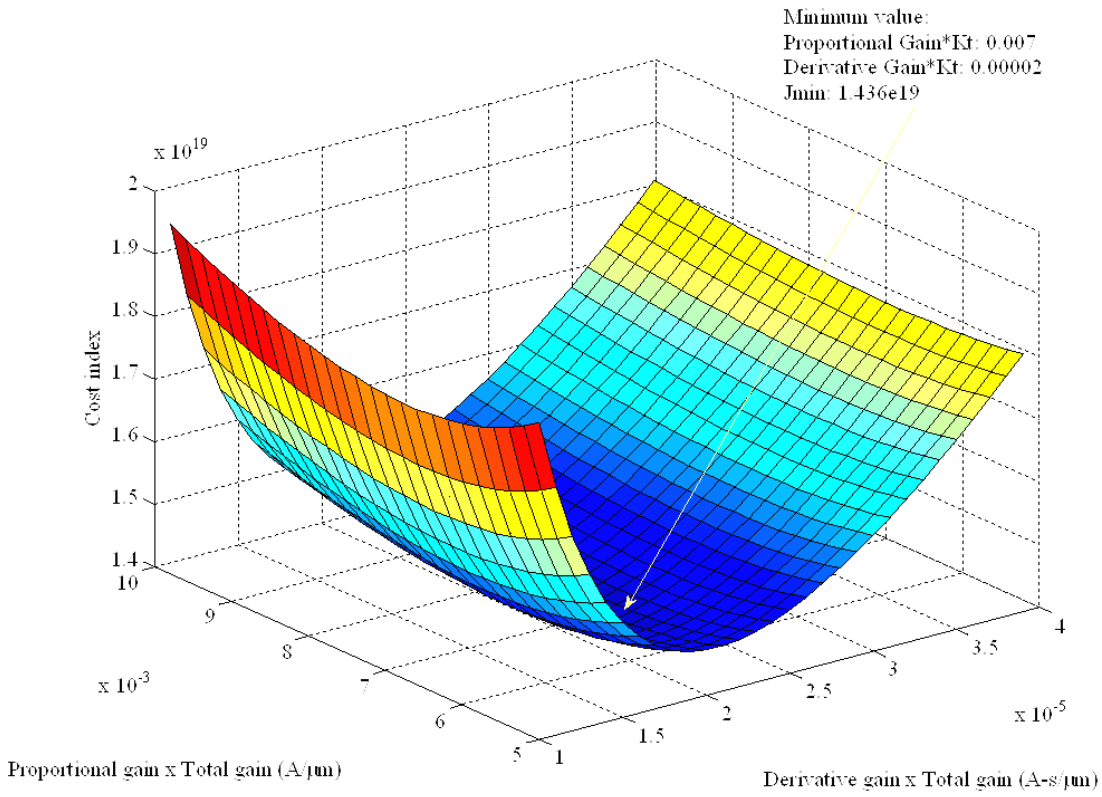

Figure 4. 3 Cost index from numerical simulation response to impulse corresponding to different PD combinations for the three-mass model.

Selecting the minimum point from the figure above, the final PD controller was found to be K_P =70 $\frac{\text{A}}{\mu\text{m}}$, K_D =0.2 $\frac{\text{A-s}}{\mu\text{m}}$, and with total gain K_t =0.0001. Therefore, a PD controller that minimizes the cost function for the three-mass system has the controller parameters in the following table:

Table V Nominal controller "A" parameters

Parameters	Symbol	Value	Unit
Total gain	K_t	0.0001	NA
Proportional gain	K_P	70	$\frac{\text{A}}{\mu\text{m}}$
Derivative gain	K_D	0.2	$\frac{\text{A-s}}{\mu\text{m}}$
Minimum cost function	J	1.436×10^{19}	NA

4.2.2 Initial Controller "B" Design for the Finite Element Model

The aforementioned procedure is performed for the finite element model. Figure 4.4 below shows the cost index with respect to K_P and K_D using the cost function Equation (4.4).

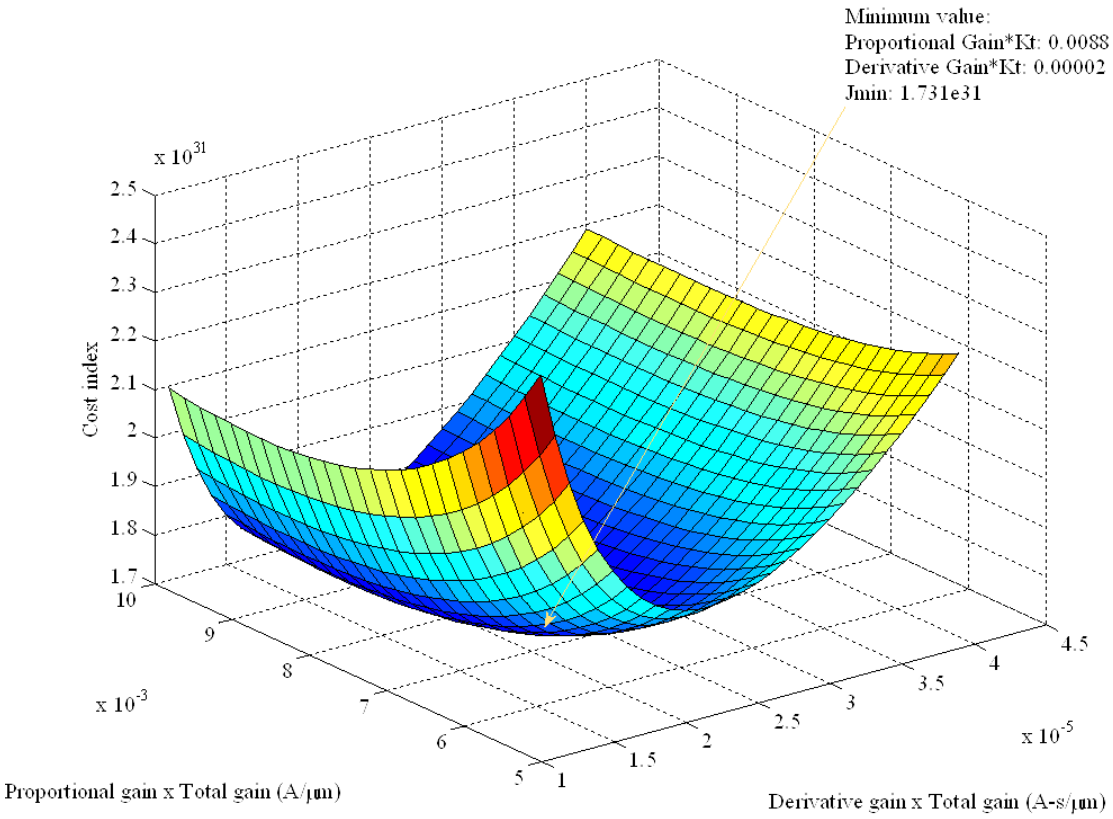

Figure 4. 4 Cost index from numerical simulation response to impulse corresponding to different PD combinations for the FE model.

Selecting the minimum point from the figure above, the final PD controller was found to be K_P =88 $\frac{A}{\mu m}$, K_D =0.2 $\frac{A\text{-}s}{\mu m}$, and with total gain K_t =0.0001. Therefore, a PD controller

that minimizes the cost function for the finite element system has the controller parameters in the following table:

Table VI Nominal controller "B" parameters

Parameters	Symbol	Value	Units
Total gain	K_t	0.0001	NA
Proportional gain	K_P	88	$\frac{\text{A}}{\mu\text{m}}$
Derivative gain	K_D	0.2	$\frac{\text{A-s}}{\mu\text{m}}$
Minimum cost function	J	1.731×10^{31}	NA

4.3 Numerical Simulation

4.3.1 Introduction

Matlab Simulink simulations are carried out in this section based on the mathematical models set up in the previous sections. Dormand-Prince numerical integration with variable step size is used. Both the finite element model and the approximate analytical model are simulated under the same conditions but utilizing their corresponding controllers which have been developed. Simulation results show the vibration response when the rotor is spinning at different speeds. A zero initial condition is employed and the transient is allowed to die out. An unbalance of 0.000023 *kg-m* is applied at the disk for both models.

4.3.2 Simulation Using Controller "A"

The whole closed-loop AMB system is implemented in Simulink software in order to simulate the behavior for the controlled system. The generated PD controller previously

discussed is implemented in the simulation model. Figure 4.5 below shows a two axes control schematic for the AMBs. An unbalance force is applied at the disk with a 90° phase different from one plane to the other. The state-space model of the approximate analytical model used in this simulation model has two inputs one at the disk, the other at the right mass, m_r. The AMB force is applied at m_r. The two outputs of the model are also taken at the disk and m_r, which separately represent the ADRE sensor output and the AMB sensor output.

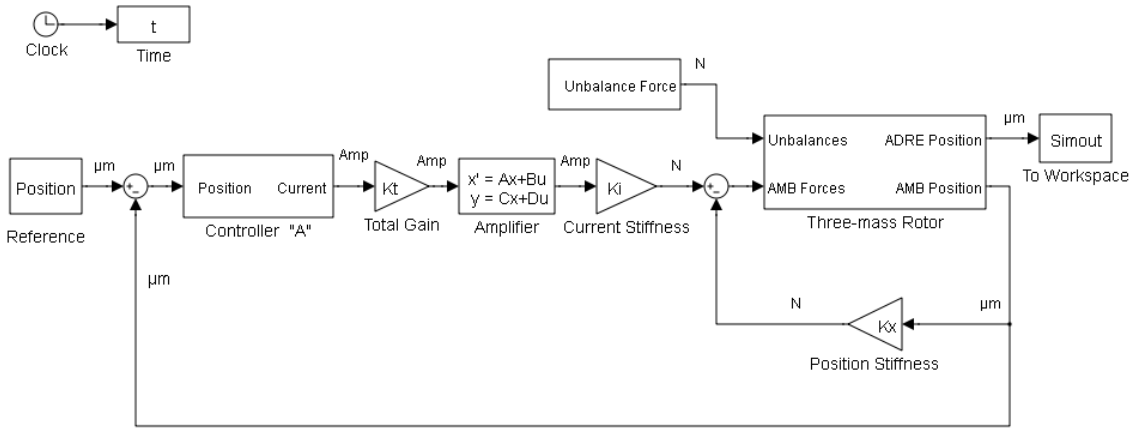

Figure 4. 5 Simulink simulation of the approximate analytical rotor and controller "A" in two planes.

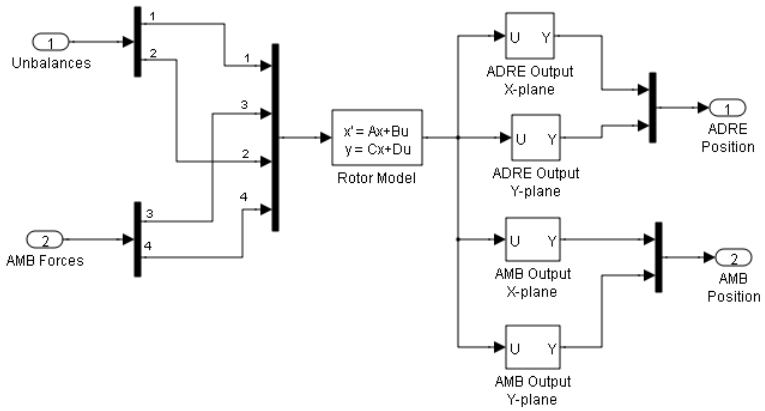

Figure 4. 6 Simulink model of the Three-mass rotor shown in Figure 4.5

In order to simulate the responses, one at the ADRE sensor, and the other at the AMB sensor, the three-mass analytical model should have two outputs in each plane. Also two inputs are needed in each plane, the first on the disk for unbalance force, and the second on the AMB rotor for the magnetic force. The state-space representation for the approximate analytical model (without the amplifier and the AMB) will result in a change in the input matrix and the output matrix, which yields:

$$\mathbf{B_2} = \begin{bmatrix} 0 & 0 \\ 0 & 0 \\ 0 & 0 \\ 0 & 0 \\ -\frac{1}{m_r} & 0 \\ 0 & -\frac{1}{m_r} \end{bmatrix}, \quad \mathbf{C_2} = \begin{bmatrix} 0 & 1 & 0 & 0 & 0 & 0 \\ 0 & 0 & 1 & 0 & 0 & 0 \end{bmatrix}$$

The unbalance block in Figure 4.5 is shown in the following Figure 4.7:

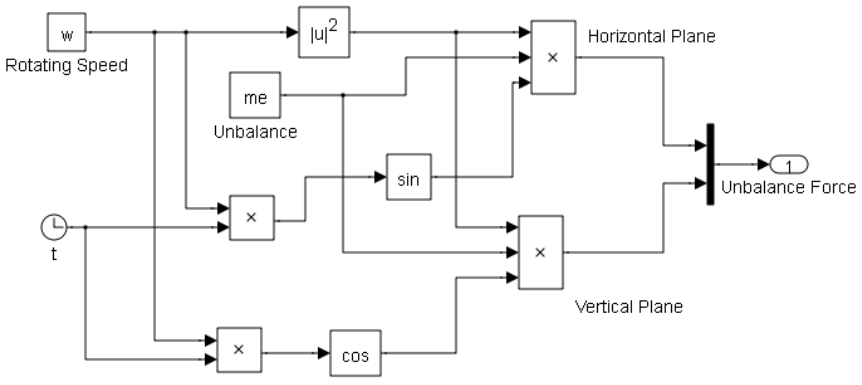

Figure 4. 7 Simulink model of the unbalance shown in Figure 4.5

Figure 4.8 through 4.15 below shows the system vibration response 1000 RPM, 1600 RPM, 2000 RPM, and 2500 RPM respectively at the AMB sensor and the ADRE sensor.

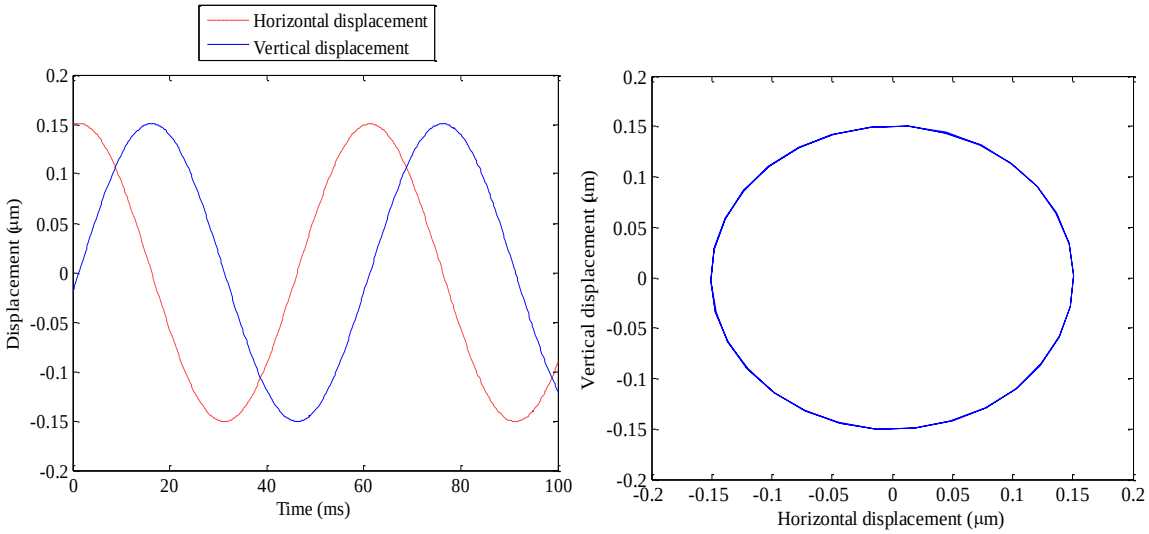

a) **b)**

Figure 4. 8 Simulation at 1000 RPM using controller "A" at AMB sensor. a) Time response. b) Orbit.

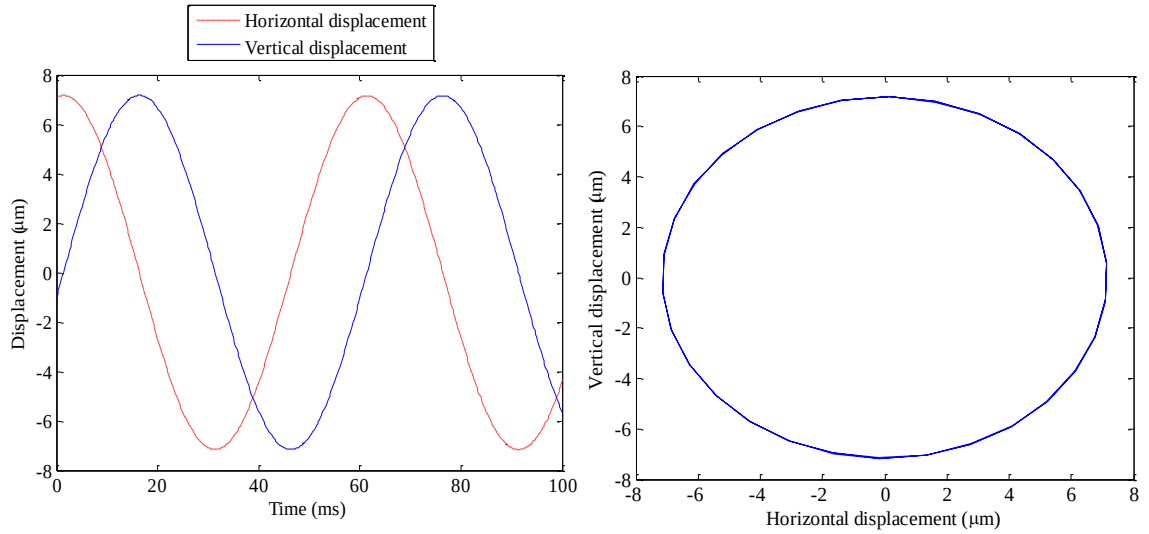

a) **b)**

Figure 4. 9 Simulation at 1000 RPM using controller "A" at ADRE sensor. a) Time response. b) Orbit.

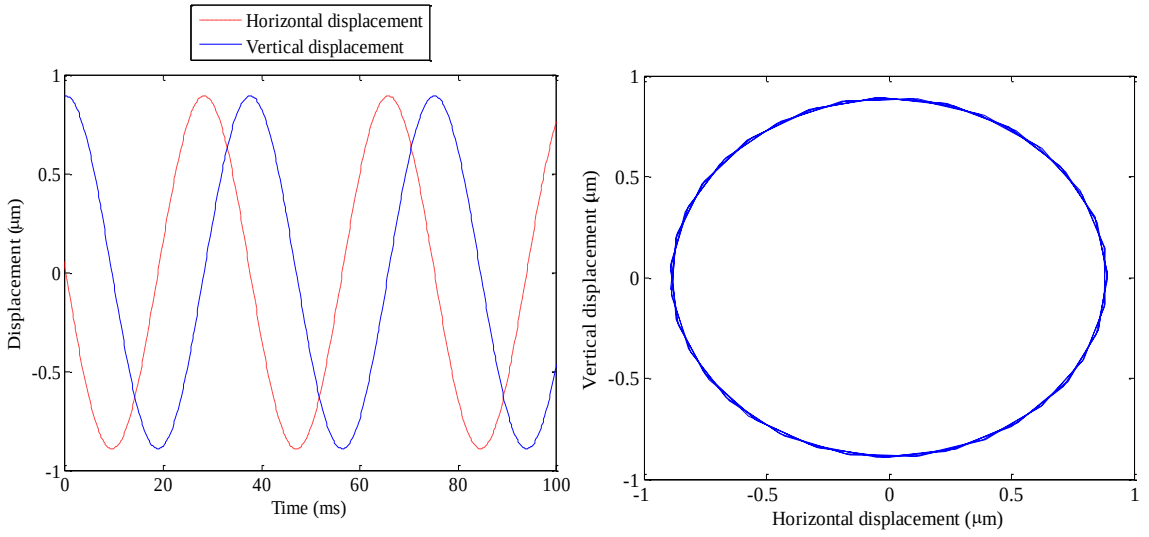

a) **b)**

Figure 4. 10 Simulation at 1600 RPM using controller "A" at AMB sensor. a) Time response. b) Orbit.

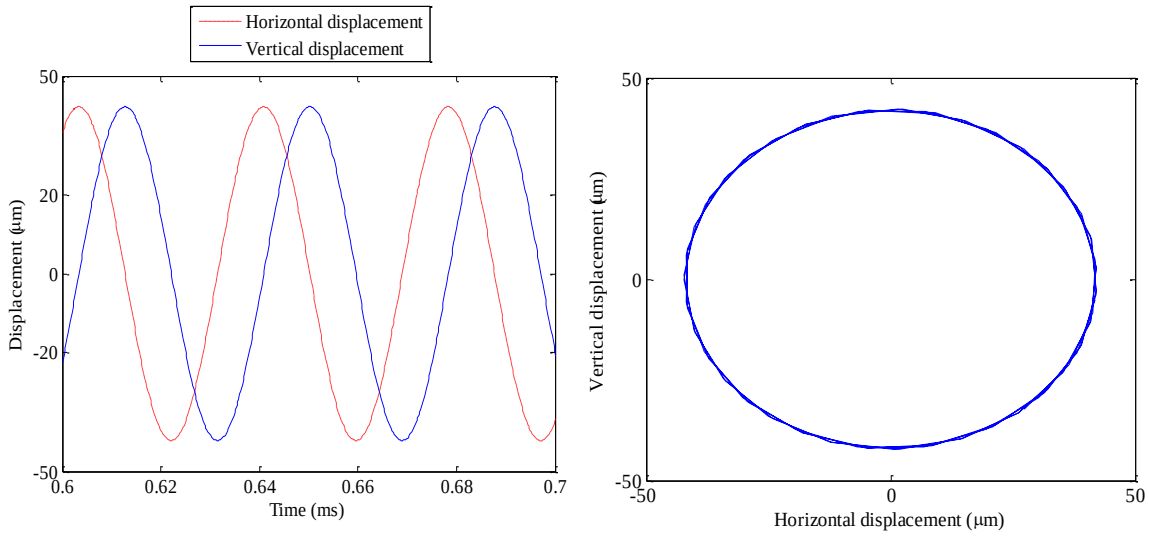

a) **b)**

Figure 4. 11 Simulation at 1600 RPM using controller "A" at ADRE sensor. a) Time response. b) Orbit.

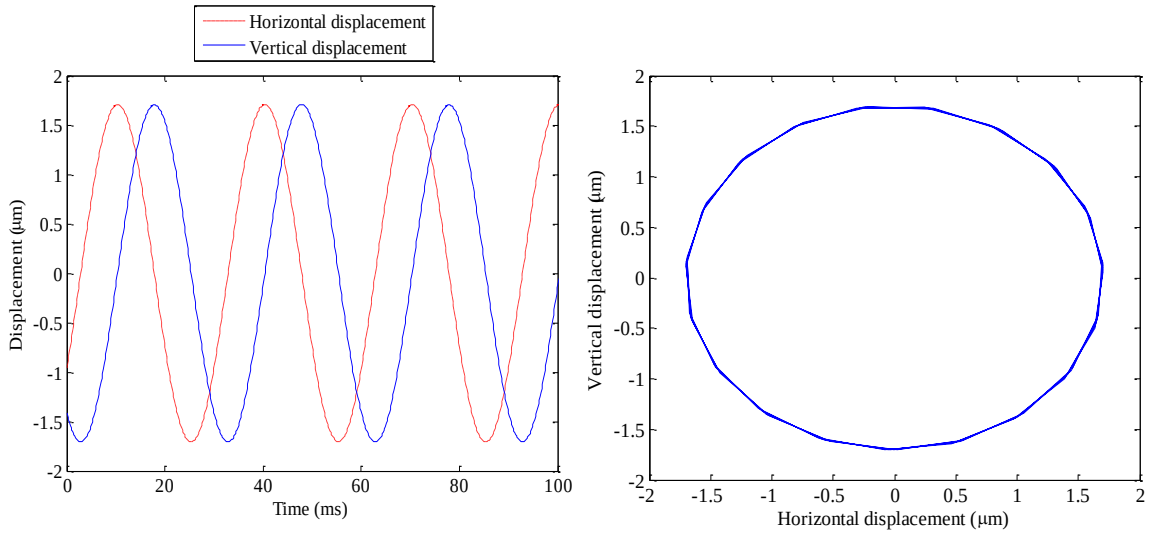

a) **b)**

Figure 4. 12 Simulation at 2000 RPM using controller "A" at AMB sensor. a) Time response. b) Orbit.

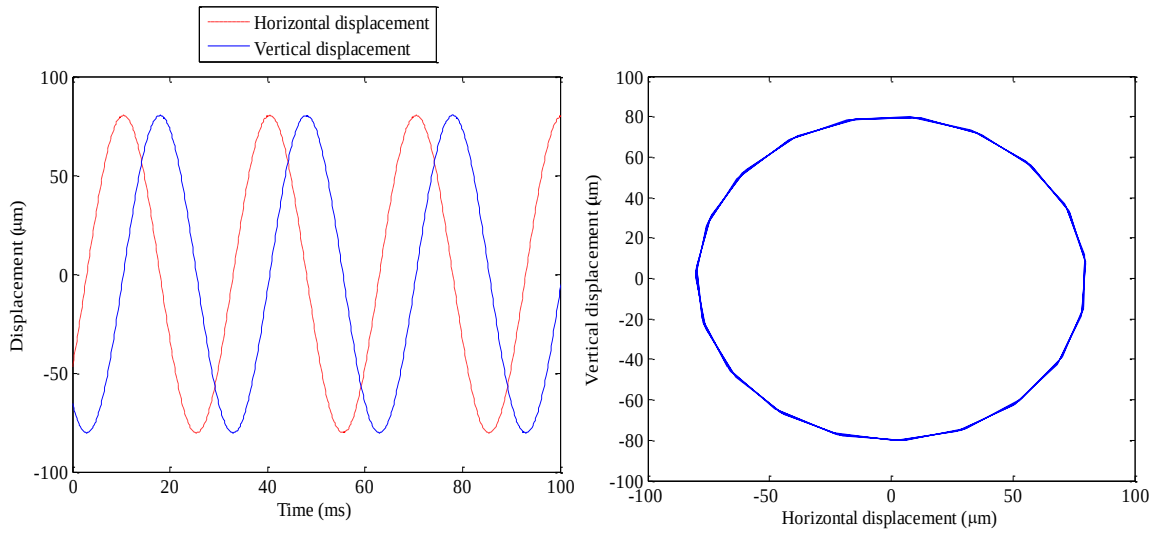

a) **b)**

Figure 4. 13 Simulation at 2000 RPM using controller "A" at ADRE sensor a) Time response. b) Orbit.

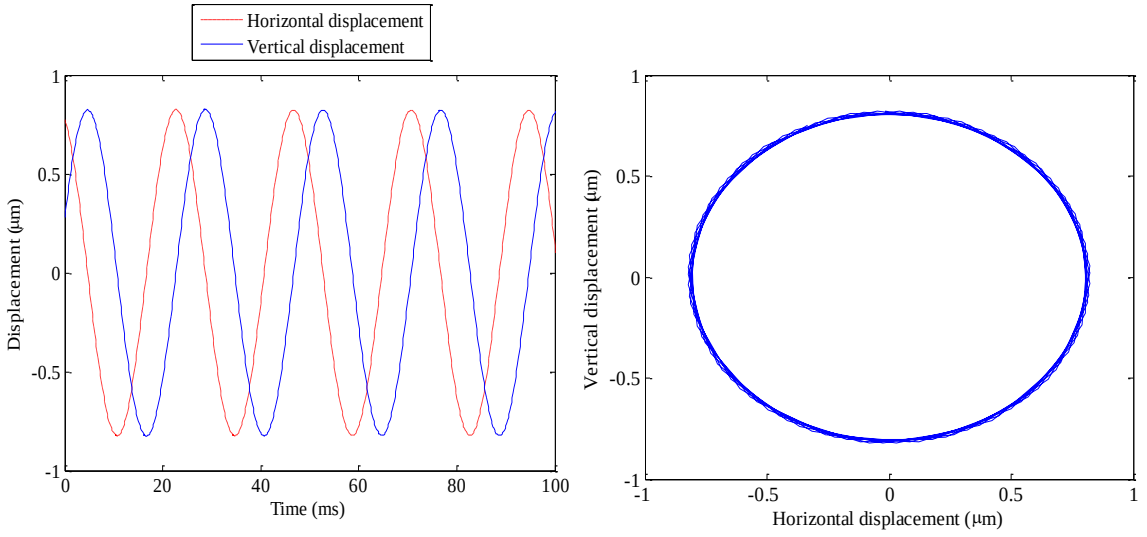

a) **b)**

Figure 4. 14 Simulation at 2500 RPM using controller "A" at AMB sensor. a) Time response. b) Orbit.

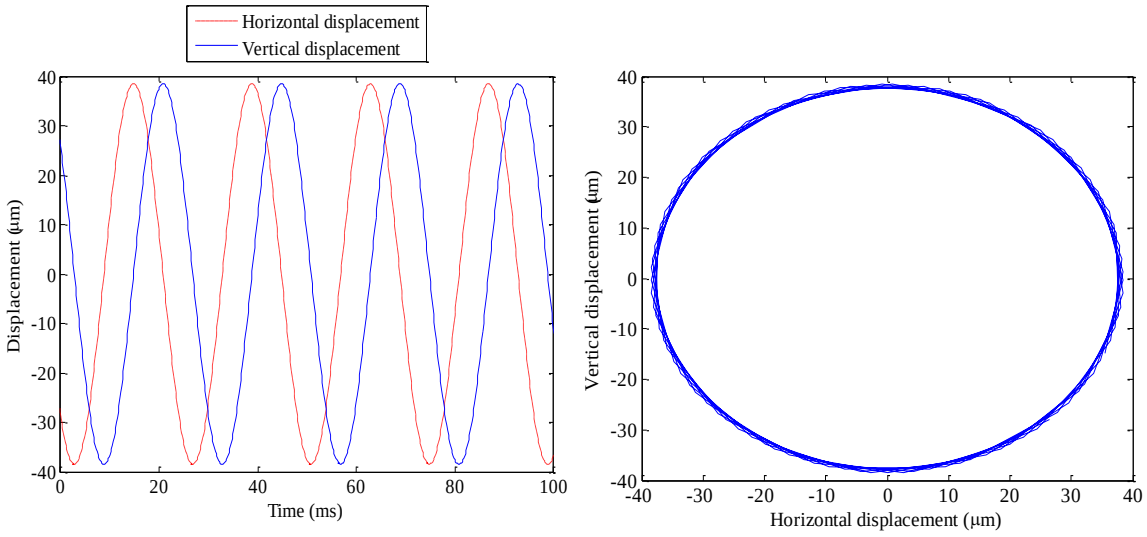

a) **b)**

Figure 4. 15 Simulation at 2500 RPM using controller "A" at ADRE sensor. a) Time response. b) Orbit.

4.3.3 Simulation Using Controller "B"

The whole closed-loop AMB system is implemented in Simulink software in order to simulate the behavior for the controlled system. The generated PD controller previously discussed is implemented in the simulation model. Figure 4.16 below shows a two axes control schematic for the AMBs corresponding to the FE model. Unbalance force is applied at the disk with a 90° phase different from one plane to the other. The state-space model of the FE model has three inputs, first at the bushing center, second at the disk, and the third is placed on the AMB center of force. Outputs are placed at the nodes that correspond to the ADRE sensor output and AMB sensor output. Another output at the bushing center is needed for making the bushing stiffness. The free-free model matrices are used in the rotor model which does not include bushing and AMB stiffness. Take $\mathbf{A}_{\mathbf{ff}}$, $\mathbf{B}_{\mathbf{ff}}$, $\mathbf{C}_{\mathbf{ff}}$, and $\mathbf{D}_{\mathbf{ff}}$ as the state-space matrices for the free-free rotor bearing model, $\mathbf{G}_{\mathbf{ff}}$ is taken as the gyroscopic matrix; the state vector $\mathbf{x}$ is arranged as X-plane first, then Y-plane. Then, the speed depended system can be described as follows:

$$\dot{\mathbf{x}} = \left\{\mathbf{A}_{\mathbf{ff}} + \Omega\mathbf{G}_{\mathbf{ff}}\right\}\mathbf{x} + \mathbf{B}_{\mathbf{ff}}\mathbf{u}$$
$$\mathbf{y} = \mathbf{C}_{\mathbf{ff}}\mathbf{x} + \mathbf{D}_{\mathbf{ff}}\mathbf{u}$$

Where Ω is the spinning speed of the rotor in rad/s. Figure 4.16 below shows the FE simulation model, Figure 4.17 and Figure 4.18 shows the free-free FEA rotor model and unbalance block for the whole system. Figure 4.19 through 4.26 show simulation results of the system vibration response with a rotating speed at 1000 RPM, 1600 RPM, 2000 RPM, and 2500 RPM respectively at the AMB sensor and the ADRE sensor.

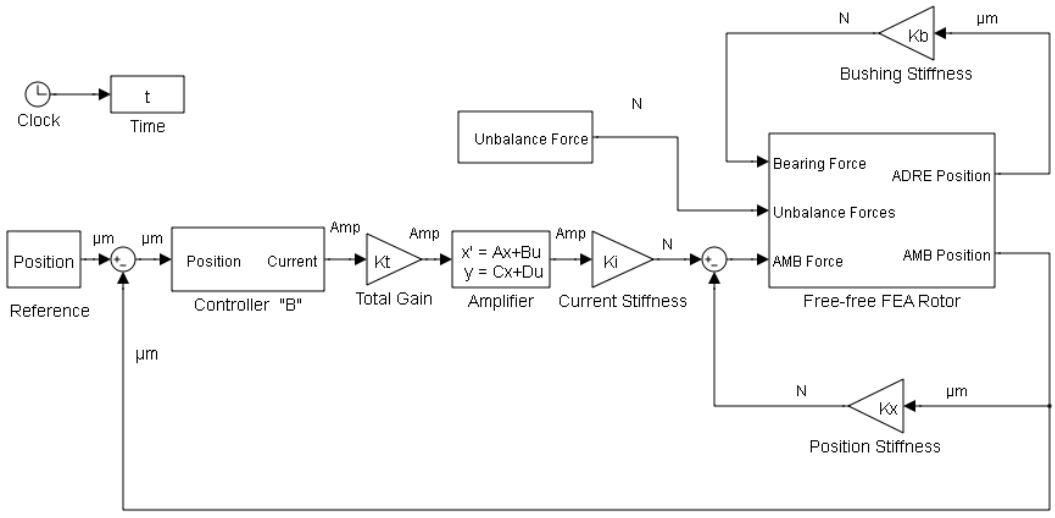

Figure 4. 16 Simulink simulation of the finite element rotor and controller "B" in two planes.

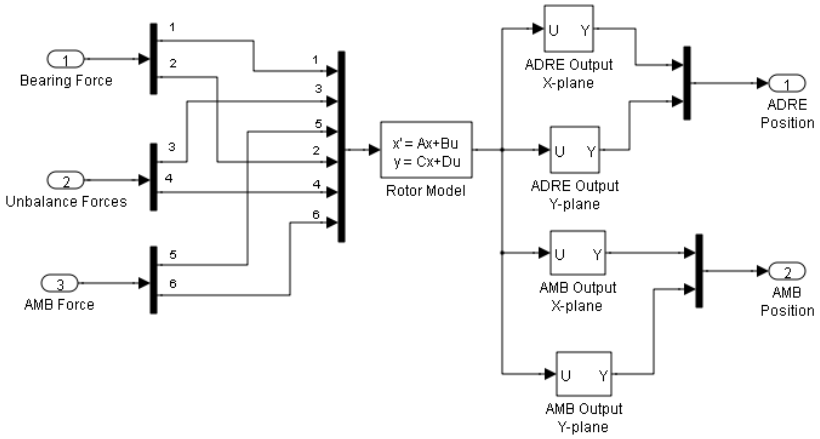

Figure 4. 17 Simulink model of the Free-free FEA Rotor shown in Figure 4.16

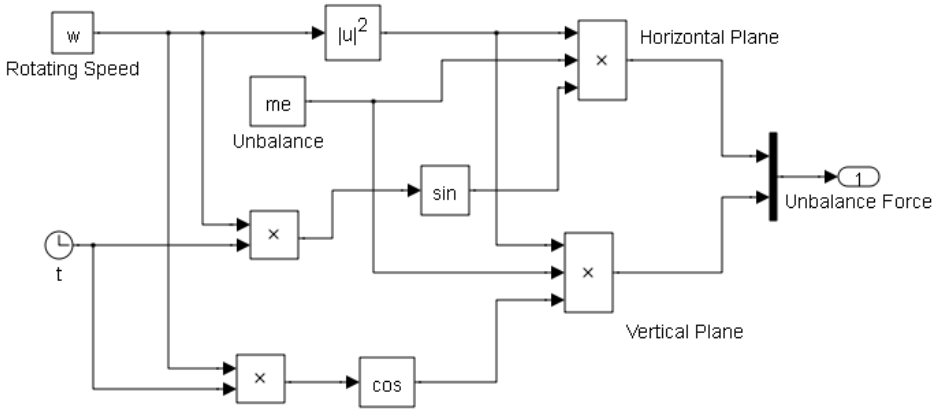

Figure 4. 18 Model block of the unbalance shown in Figure 4.16

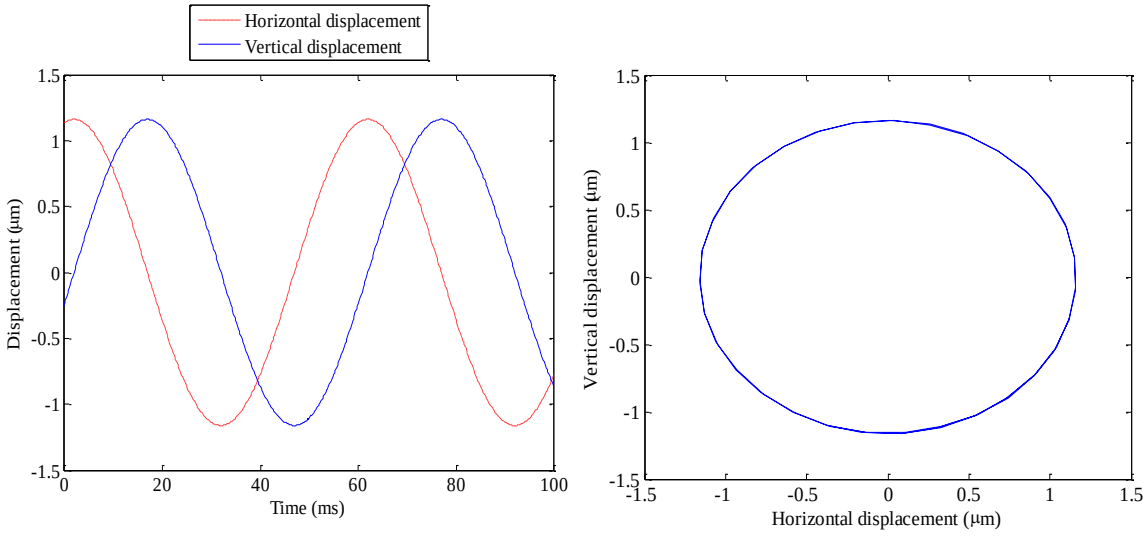

Figure 4. 19 Simulation at 1000 RPM using controller "B" at AMB sensor. a) Time response. b) Orbit.

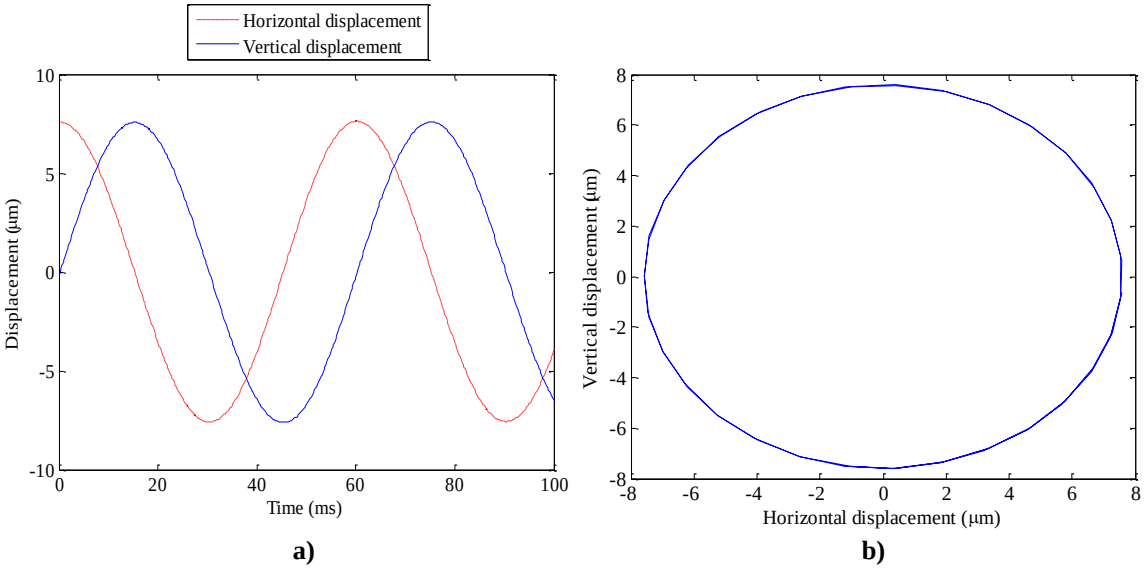

Figure 4. 20 Simulation at 1000 RPM using controller "B" at ADRE sensor. a) Time response. b) Orbit.

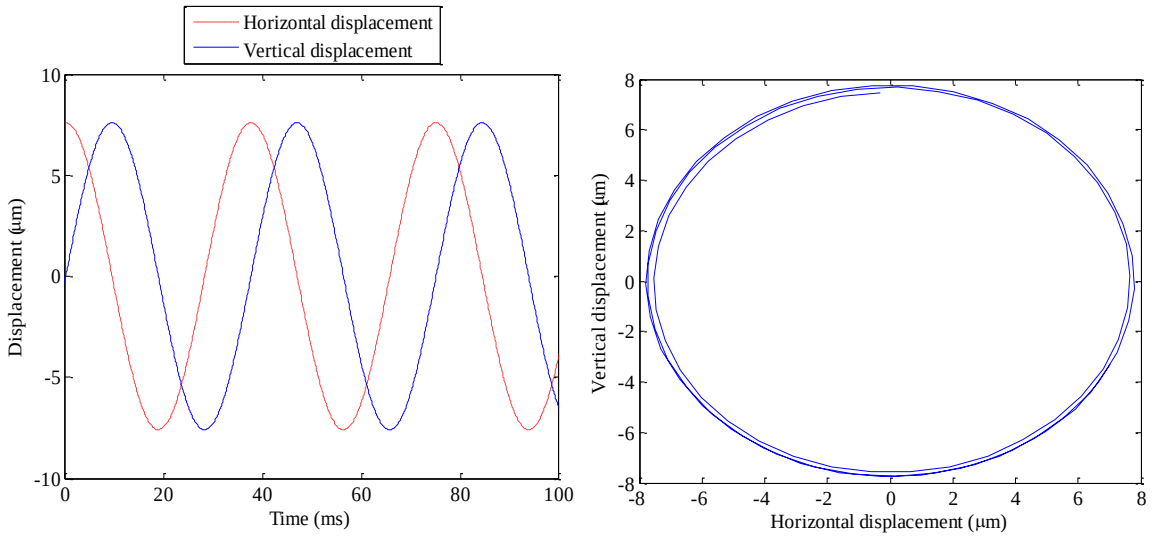

a) **b)**

Figure 4. 21 Simulation at 1600 RPM using controller "B" at AMB sensor. a) Time response. b) Orbit.

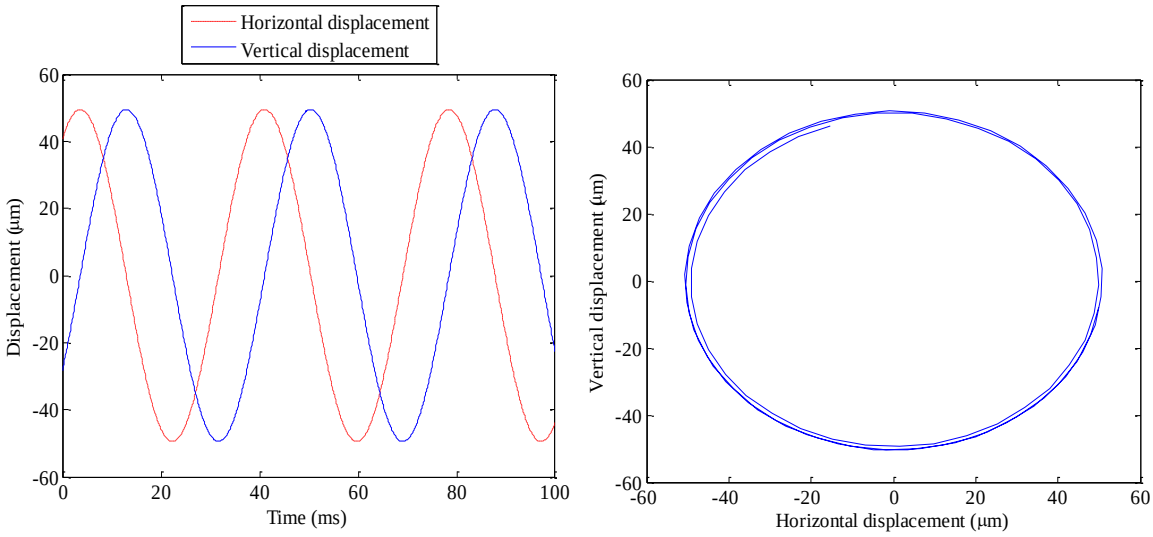

a) **b)**

Figure 4. 22 Simulation at 1600 RPM using controller "B" at ADRE sensor. a) Time response. b) Orbit.

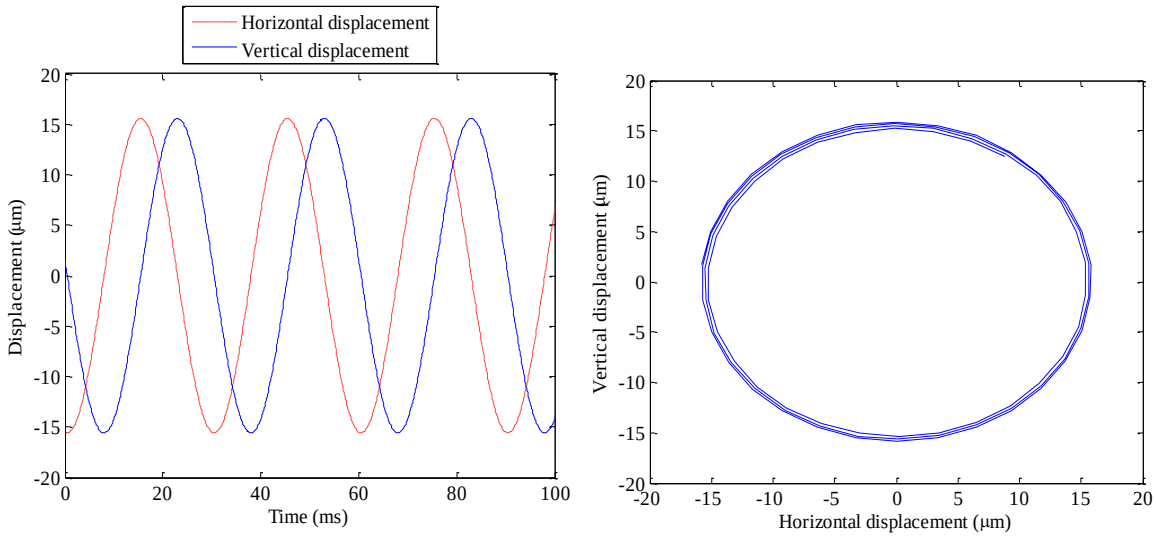

a) **b)**

Figure 4. 23 Simulation at 2000 RPM using controller "B" at AMB sensor. a) Time response. b) Orbit.

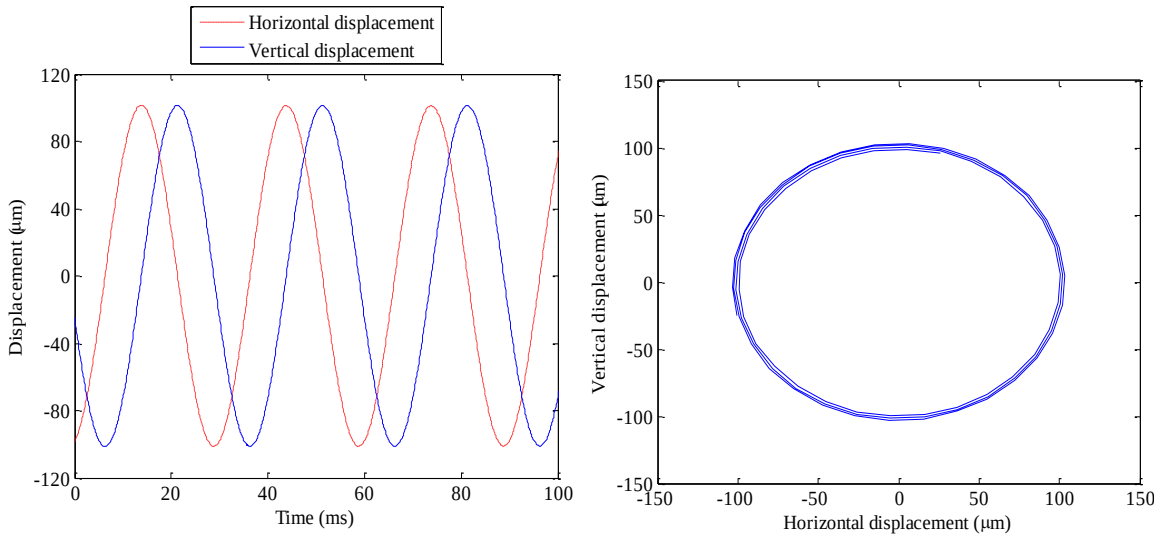

a) **b)**

Figure 4. 24 Simulation at 2000 RPM using controller "B" at ADRE sensor. a) Time response. b) Orbit.

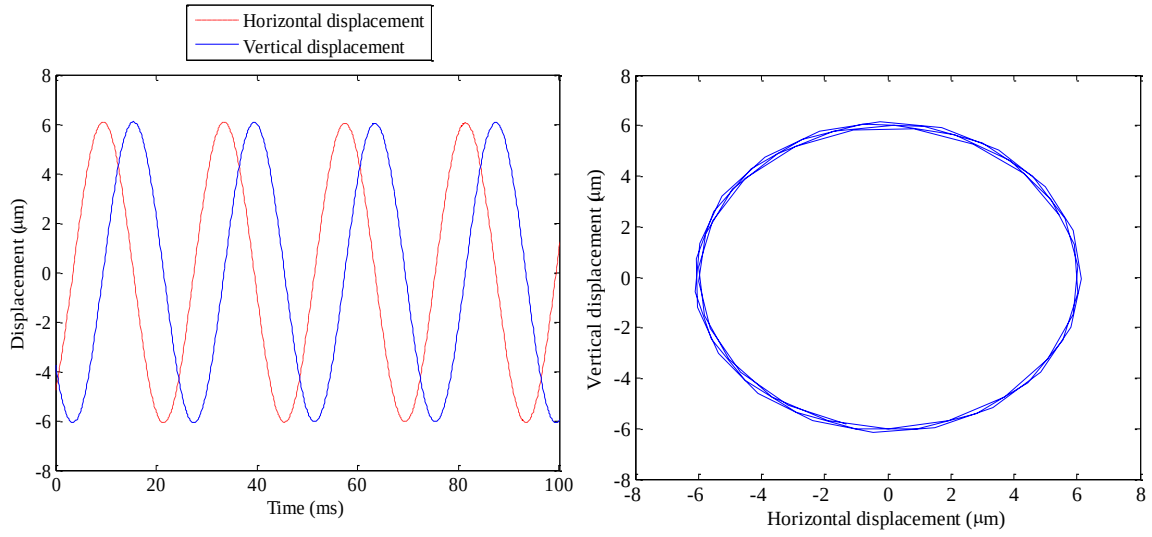

a) **b)**

Figure 4. 25 Simulation at 2500 RPM using controller "B" at AMB sensor. a) Time response. b) Orbit.

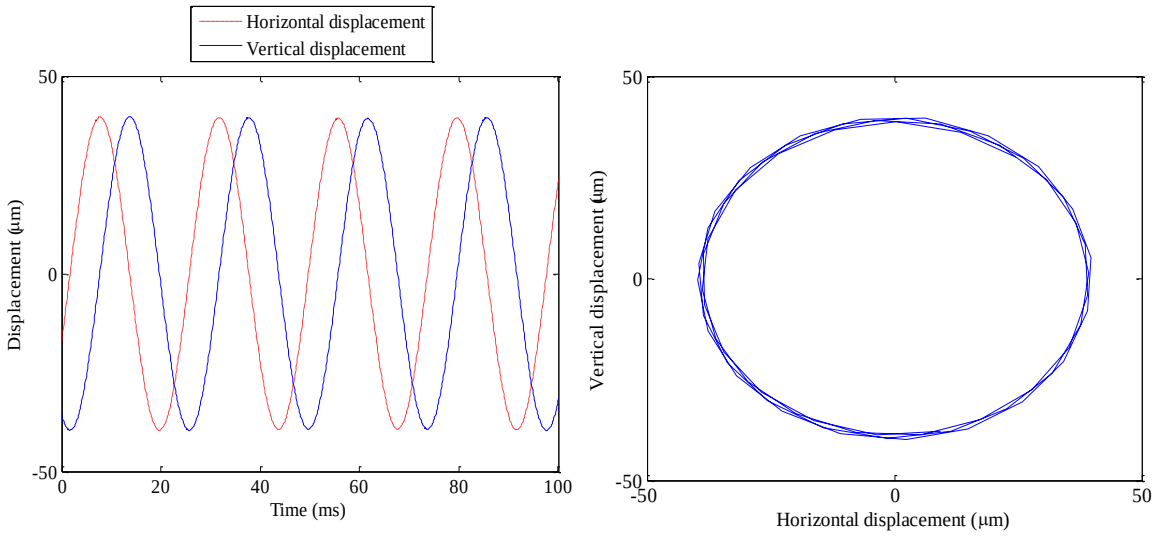

a) **b)**

Figure 4. 26 Simulation at 2500 RPM using controller "B" at ADRE sensor. a) Time response. b) Orbit.

4.4 Practical Implementation Issues

In order to successfully levitate the system, at least one low pass filter must be used. Low pass filters are used to attenuate controller gain at frequencies above the bandwidth of the controller. The low pass filter also serves as an anti-aliasing filter for digital implementation of the controller and to eliminate high frequency noise which does not occur in the simulation. In this research one low pass filter with a cut off frequency of 1500 Hz and 0.707 damping ratio is used. The transfer function of the low pass filter can be written as:

$$G_L = \frac{\omega_{lp}^2}{s^2 + 2\zeta_{lp}\omega_{lp}s + \omega_{lp}^2} \tag{3.5}$$

Where the ω_{lp} is the cut off frequency of the low pass filter and ζ_{lp} is the damping of the low pass filter.

An additional tool for stabilizing the actual system is the notch filter. The notch filter, or band stop filter, has near zero gain for a specific narrow frequency range and a gain of one for all other frequencies. It is useful because the actual rotor, being continuous, has a theoretically infinite number of flexible modes. Either rotor model, having a finite number of flexible modes, will result in a controller which may excite the neglected flexible modes of the actual system. The notch filters are designed manually post hoc and cascaded with the AMB controller to counter this. Also note that the rotor flexible modes will have at least some damping due to the flexing of the shaft material. The transfer function of a notch filter can be written as:

$$G_N = \frac{s^2 + \omega_n^2}{s^2 + 2\zeta_n \omega_n s + \omega_n^2} \tag{3.6}$$

Where the ω_n is the notch frequency of the notch filter and ζ_n is the damping of the notch filter. The low pass filter and the notch filter are discussed and the transfer functions are given by Maslen [2009].

So the overall transfer function of a controller in this study is the controller in series with the low pass filter and notch filter. Then, the controller transfer function becomes:

$$G = G_N G_L G_{PD} = G_N G_L \left(K_P + K_D s \right) \tag{3.7}$$

Both controller designs are based on horizontal axis, but in reality, controller in the vertical axis will need additional control current to generate a force that overcomes the rotor gravity. After designing both controllers, an integral gain 10 $\frac{\text{A}}{\mu\text{m-s}}$ in the vertical axis is added. Then Equation (3.7) will be updated as follows:

$$G = G_N G_L G_{PID} = G_N G_L \left(K_P + K_D s + \frac{K_I}{s} \right) \tag{3.8}$$

4.5 Finalized Controller "A" and "B"

Table VII below shows the final parameters for controller "A" and controller "B" in horizontal axis and vertical axis. Figure 4.27 shows the bode plot of the transfer function for both controllers in the horizontal direction.

Table VII Finalized controller parameters

Parameters	Controller "A"		Controller "B"	
	X-axis	**Y-axis**	**X-axis**	**Y-axis**
Total gain K_t	0.0001	0.0001	0.0001	0.0001
Proportional gain K_P $(\frac{A}{\mu m})$	70	70	88	88
Derivative gain K_D $(\frac{A\text{-}s}{\mu m})$	0.2	0.2	0.2	0.2
Integral gain K_I $(\frac{A}{\mu m\text{-}s})$	0	10	0	10
Low pass filter cut off frequency ω_{lp} (Hz)	1500	1500	1500	1500
Low pass filter damping ζ_{lp}	0.707	0.707	0.707	0.707
Notch filter frequency ω_n (Hz)	514	514	514	514
Notch filter damping ratio ζ_n	0.2	0.2	0.2	0.2

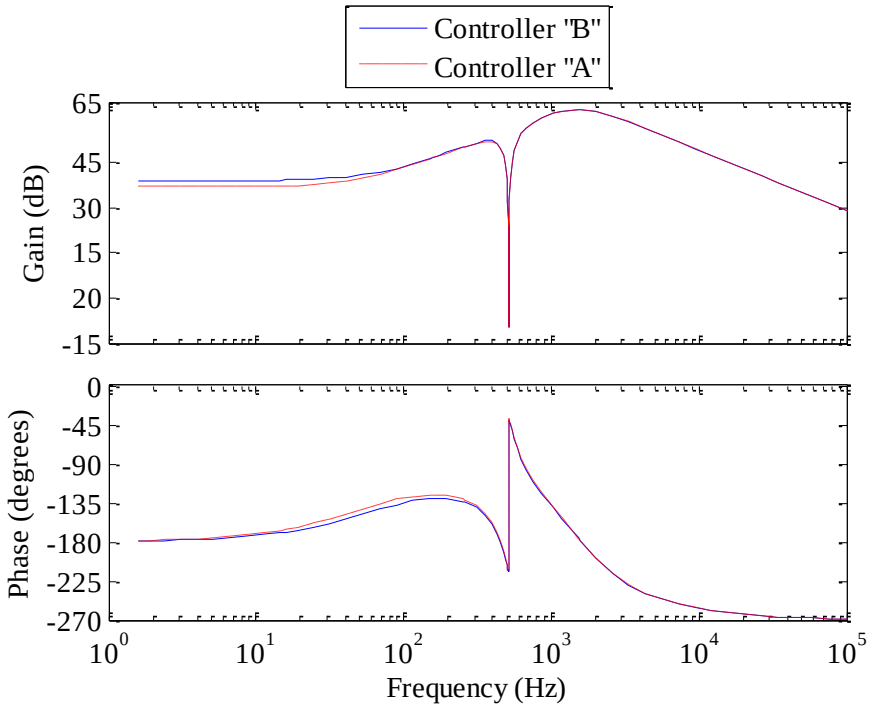

Figure 4. 27 Horizontal controllers "A" and "B" with low pass filter and a notch filter.

CHAPTER V

EXPERIMENTAL PROCEDURE AND RESULTS

5.1 Introduction

Experiments using the test rig described in Chapter II and modeled in Chapter III are carried out. Results are presented and discussed in this chapter. The experiments consist of implementation of both controllers designed in Chapter IV. To evaluate performances of the controllers, the rig is rotated at several speeds (1000, 1600, first natural frequency, 2000, and 2500 RPM). The time response and orbit are observed at the AMB and the disk, the cost function (Equation 4.4) is evaluated at each speed. An initial step before performing these experiments is identification of transfer function for the closed loop systems. This is realized using MBScope Analyzer tool through a sine sweep test. By injecting a harmonic current into the AMB over a range of frequencies, it is possible to measure the magnitude and phase of the response at each frequency, and construct the Bode plot. Recall the system frequency response without a controller as is shown in Figure 2.12 and Figure 2.13. The transfer functions are identified for the non-rotating rig.

ADRE Sxp software and MBScope software are used in acquiring experimental data for rotation tests. The ADRE system collects rotor position data from two eddy current probes, one vertical and one horizontal, the one placing near the disk is around the mid-span of the two bearings. MBScope collects horizontal and vertical rotor position data from the two AMB position probes.

5.2 Controller "A"

5.2.1 Closed-Loop Sine Sweep Identification

Figure 5.1 and 5.2 below shows the experimental closed loop system identification using controller "A". The input is AMB control current perturbation and the output is the AMB position sensor signal. (See Figure 2.11 for block diagram.)

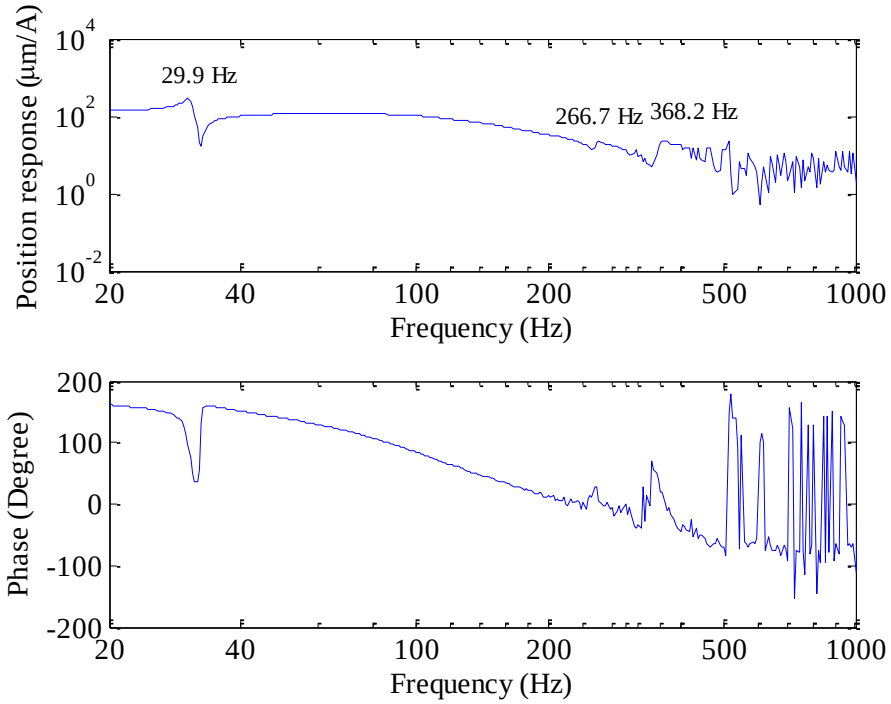

Figure 5. 1 Controller "A" closed-loop sine sweep in vertical direction

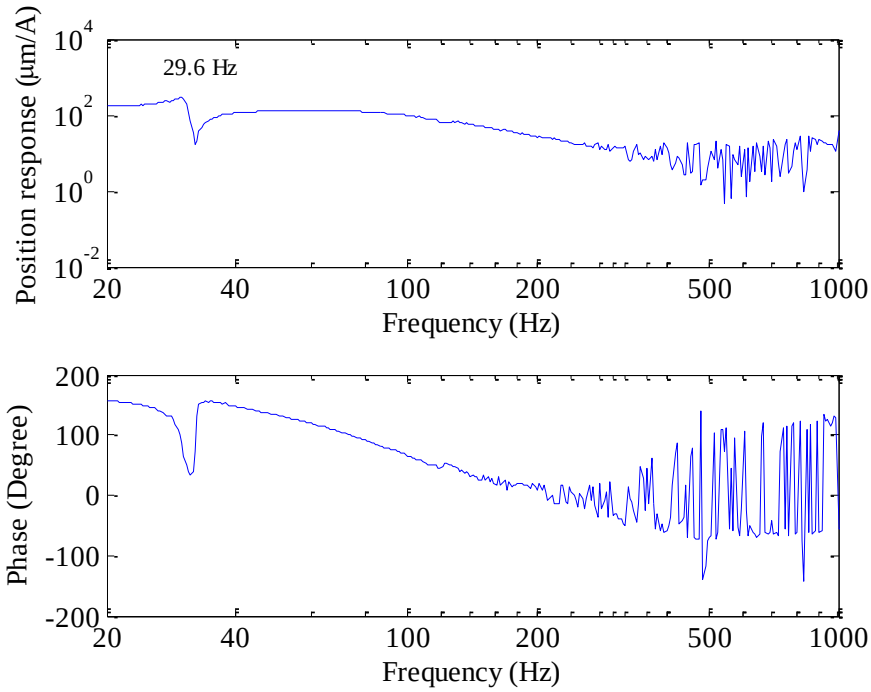

Figure 5. 2 Controller "A" closed-loop sine sweep in horizontal direction

A small change in natural frequency can be seen between the horizontal and vertical axes due to the integrator and gravity preloading. Also the resonance peaks are well damped due to the derivative gain.

5.2.2 Running Speed Tests

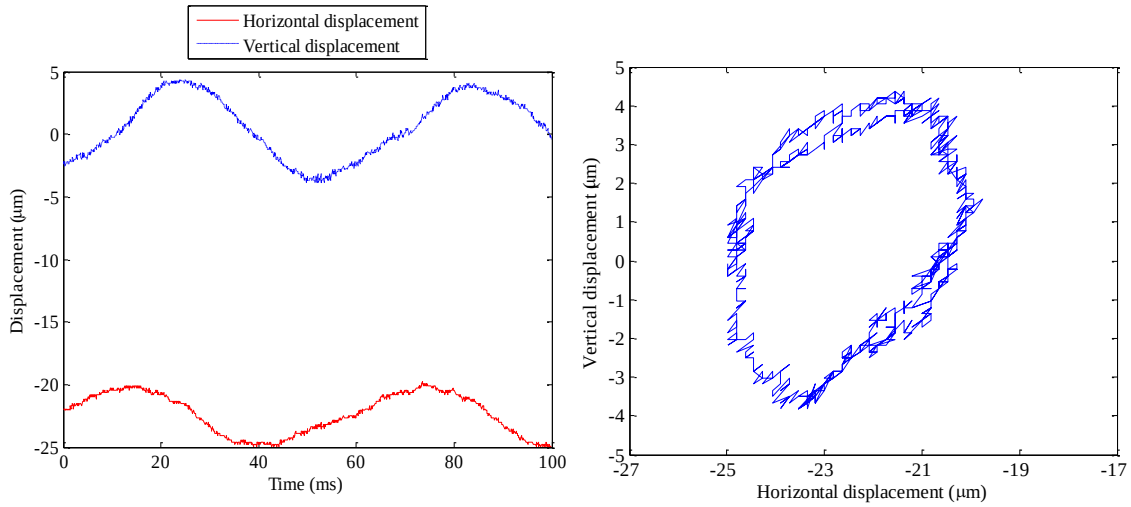

a) **b)**

Figure 5. 3 Experimental response at 1000 RPM using controller "A" at AMB sensor. a) Time response. b) Orbit.

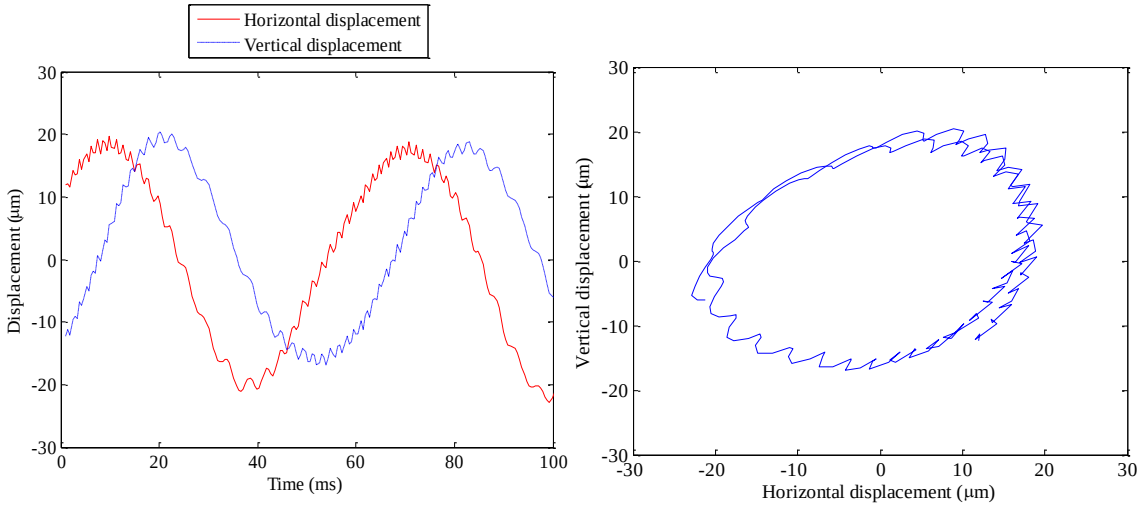

a) **b)**

Figure 5. 4 Experimental response at 1000 RPM using controller "A" at ADRE sensor. a) Time response. b) Orbit.

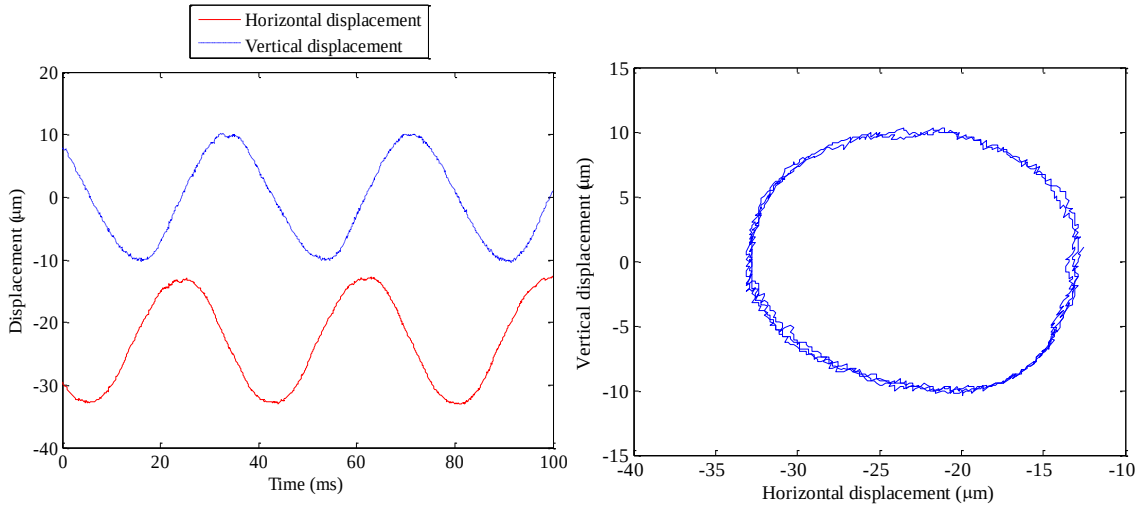

a) **b)**

Figure 5. 5 Experimental response at 1600 RPM using controller "A" at AMB sensor. a) Time response. b) Orbit.

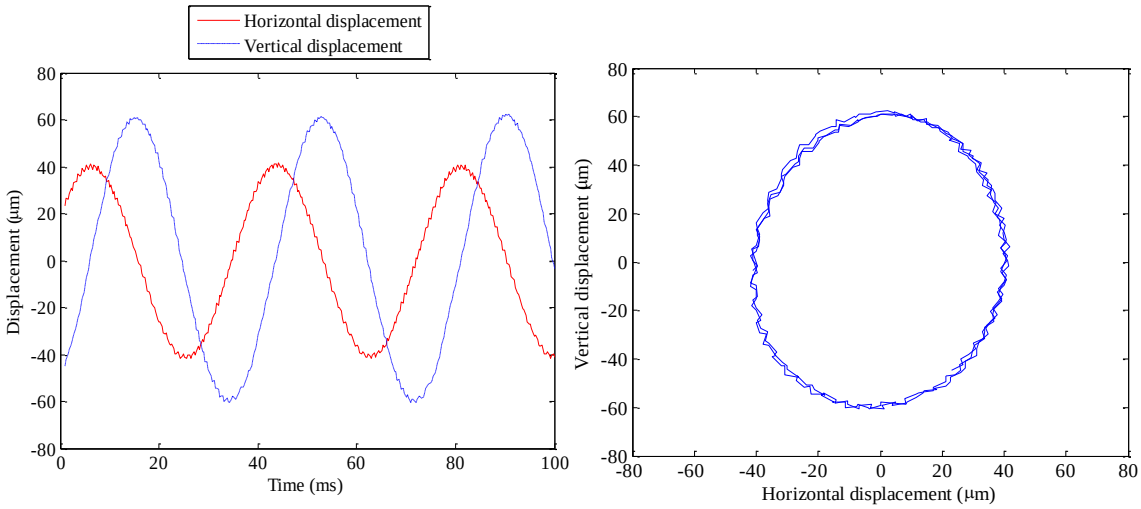

a) **b)**

Figure 5. 6 Experimental response at 1600 RPM using controller "A" at ADRE sensor. a) Time response. b) Orbit.

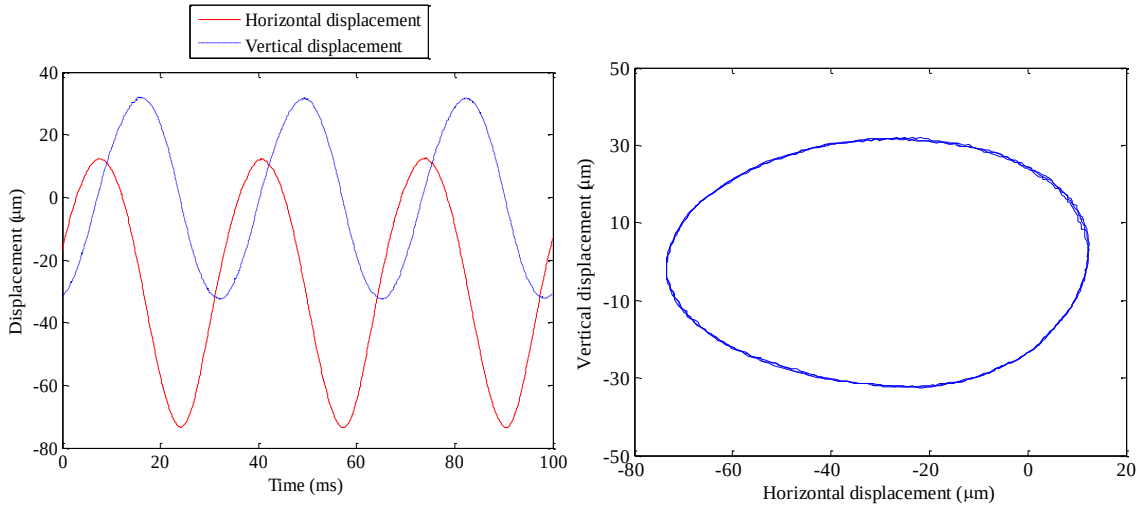

a) **b)**

Figure 5. 7 Experimental response at 1813 RPM using controller "A" at AMB sensor. a) Time response. b) Orbit.

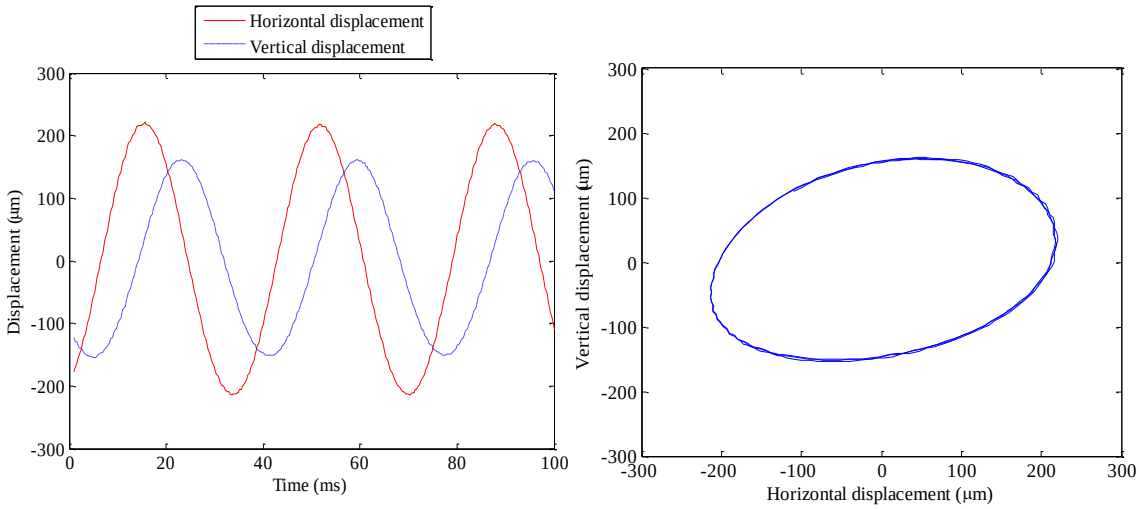

a) **b)**

Figure 5. 8 Experimental response at 1813 RPM using controller "A" at ADRE sensor. a) Time response. b) Orbit.

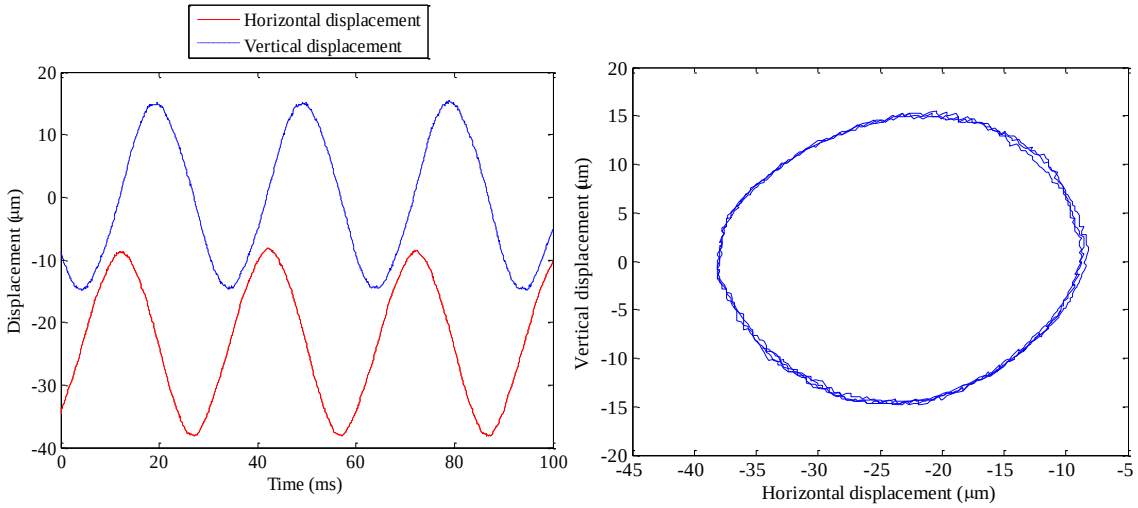

a) **b)**

Figure 5. 9 Experimental response at 2000 RPM using controller "A" at AMB sensor. a) Time response. b) Orbit.

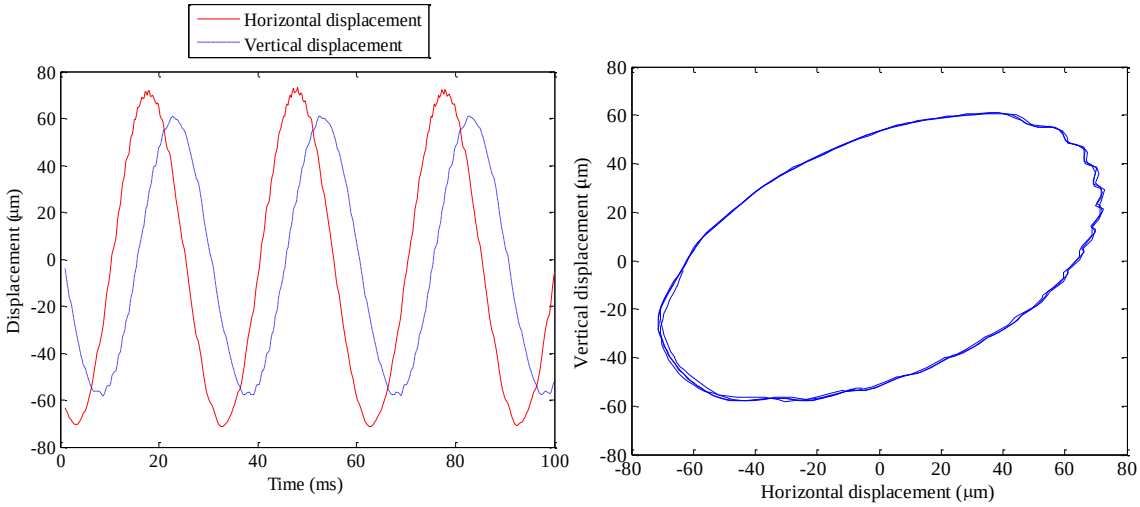

a) **b)**

Figure 5. 10 Experimental response at 2000 RPM using controller "A" at ADRE sensor. a) Time response. b) Orbit.

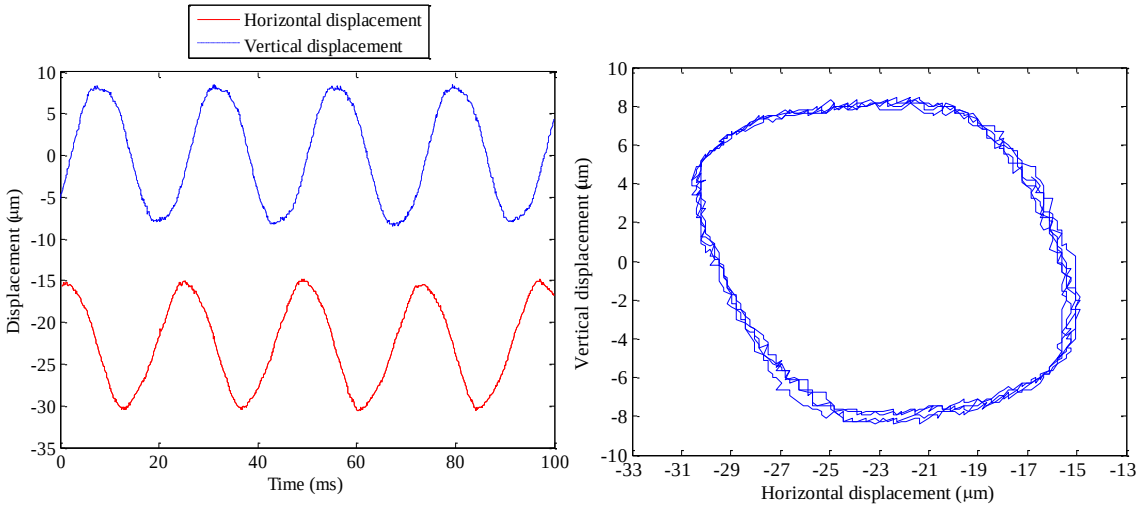

a) **b)**

Figure 5. 11 Experimental response at 2500 RPM using controller "A" at AMB sensor. a) Time response. b) Orbit.

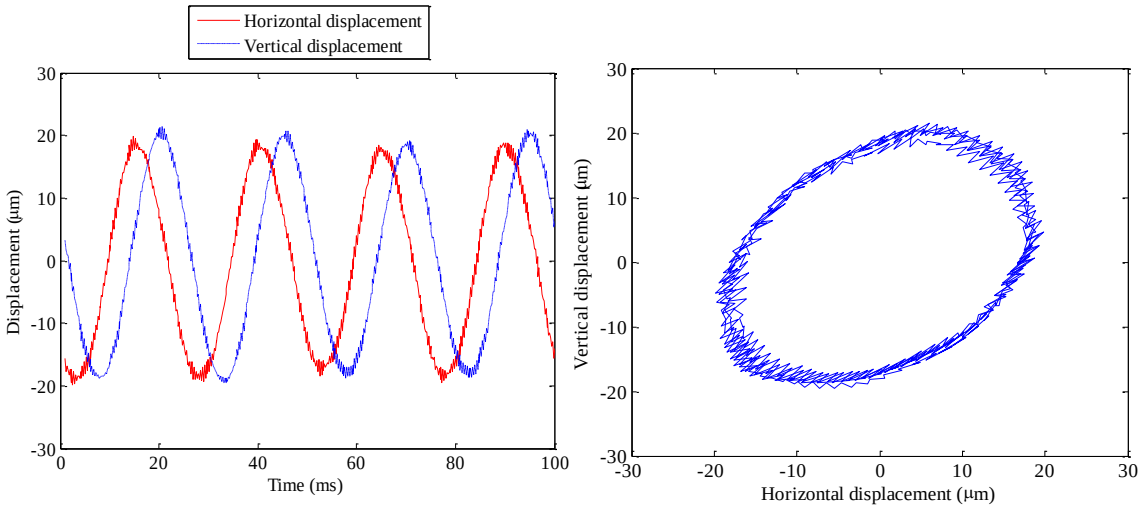

a) **b)**

Figure 5. 12 Experimental response at 2500 RPM using controller "A" at ADRE sensor. a) Time response. b) Orbit.

Figure 5.3 through 5.12 shows the system vibration response using controller “A”. From figures, the following observations can be made.

1. The closed-loop system natural frequency happens at 29.6 Hz, which is 1776 RPM when using controller “A”.
2. This experiment has verified that controller “A” is effective at levitating the system within practical limits.
3. The largest vibration has a speed around 1813 RPM, which roughly agree with the experimental closed-loop system identification result.
4. From AMB sensor data, one can read that the vertical controller with an integral term helps the system overcome gravity, all vibrations are around X-axis, when y=0. While on the other axis, there is always displacement due to rotor or AMB assembly misalignment.
5. From the ADRE sensor, horizontal and vertical vibration are always near the ideal point (0,0), because the initial installment for the ADRE sensor probes.

5.3 Controller "B"

5.3.1 Closed-loop Sine Sweep Identification

Closed-loop system identification using controller "B" is proceed in the following section, Figure 5.13 and 5.14 below shows the experimental closed loop system identification results:

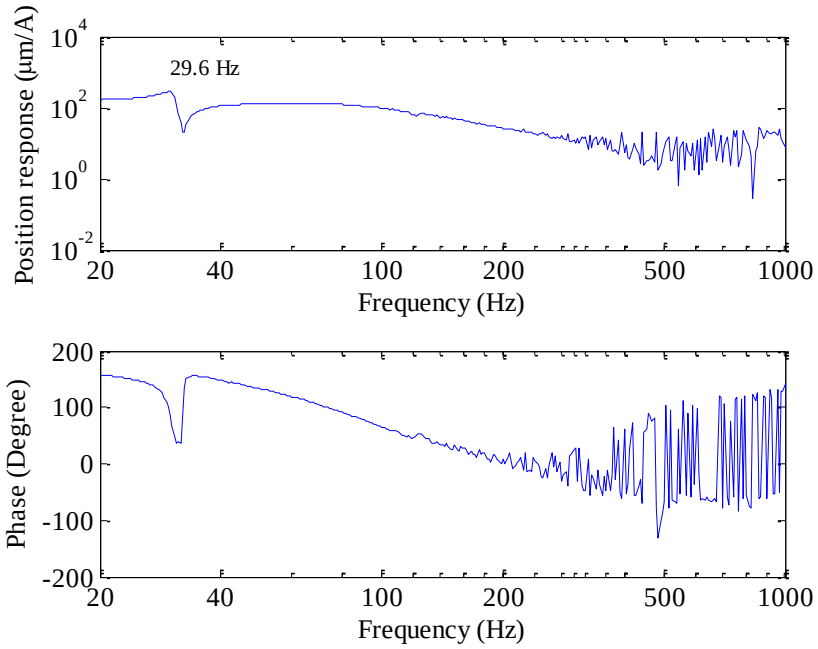

Figure 5. 13 Controller "B" closed-loop sine sweep in vertical direction

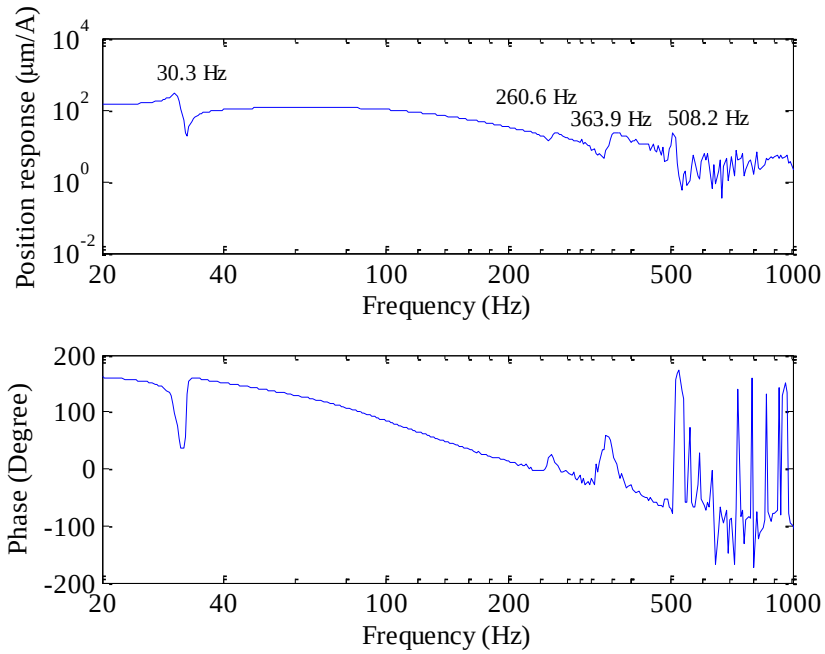

Figure 5. 14 Controller "B" closed-loop sine sweep in horizontal direction

Shown in the above figures, the closed-loop system critical speeds happen at 30.3 Hz, which is 1818 RPM.

5.3.2 Running Speed Tests

Following Figure 5.15 through Figure 5.24 shows experimental result of system vibration data corresponding to AMB sensor and ADRE sensor at speeds 1000 RPM, 1600 RPM, first natural frequency, 2000 RPM, 2500 RPM and one critical speed using controller "B"

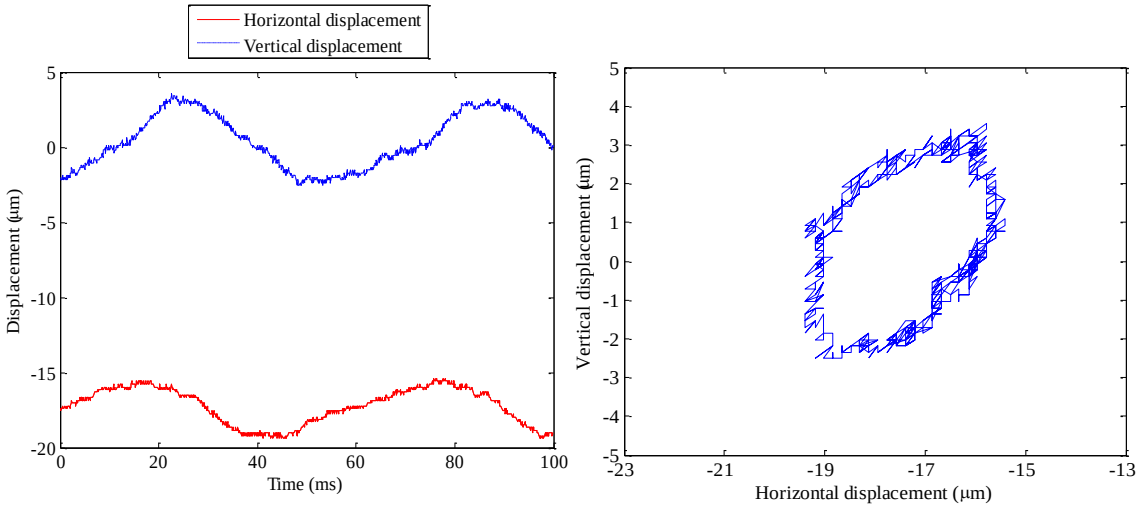

a) **b)**

Figure 5. 15 Experimental response at 1000 RPM using controller "B" at AMB sensor. a) Time response. b) Orbit.

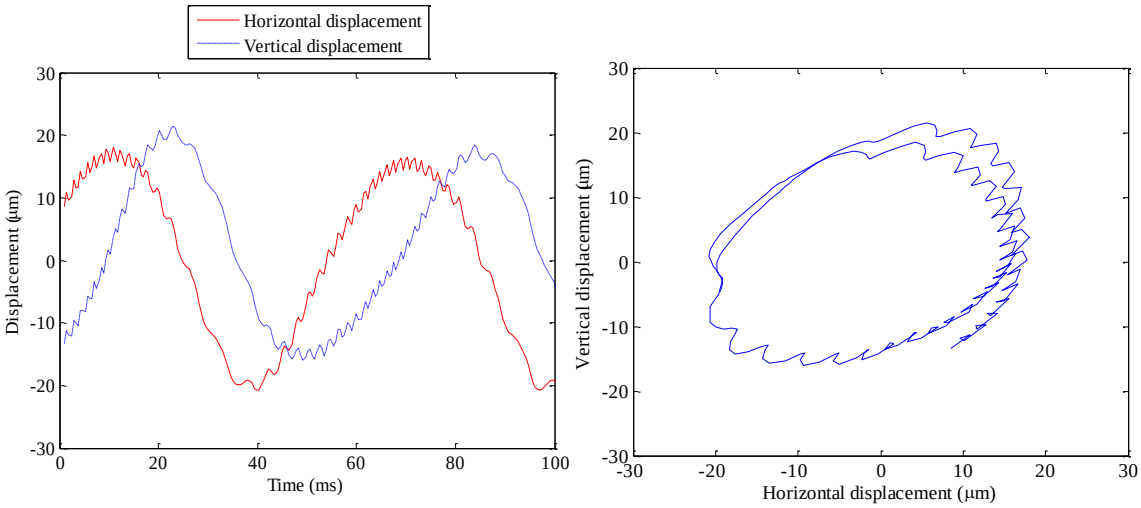

a) **b)**

Figure 5. 16 Experimental response at 1000 RPM using controller "B" at ADRE sensor. a) Time response. b) Orbit.

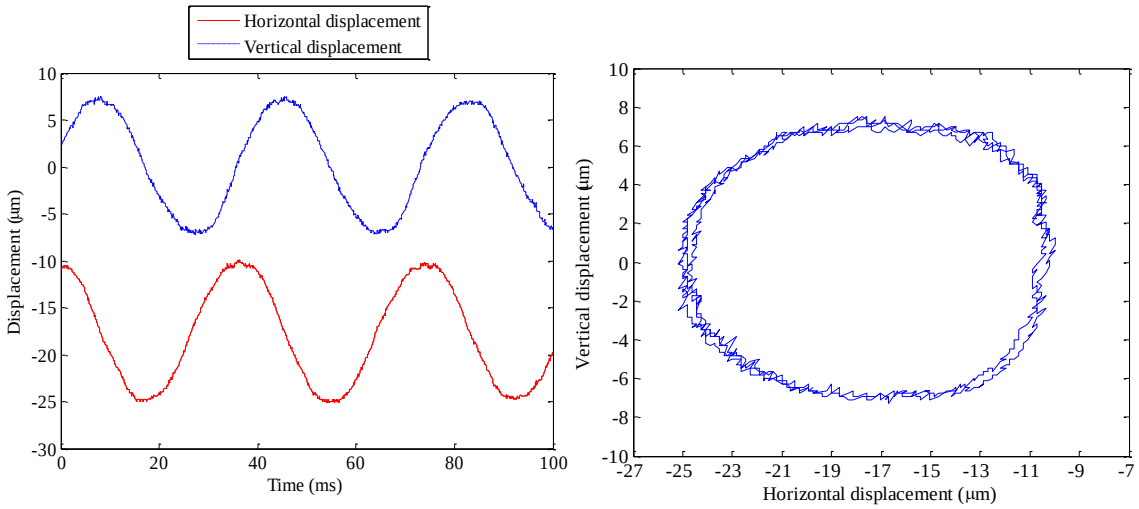

a) **b)**

Figure 5. 17 Experimental response at 1600 RPM using controller "B" at AMB sensor. a) Time response. b) Orbit.

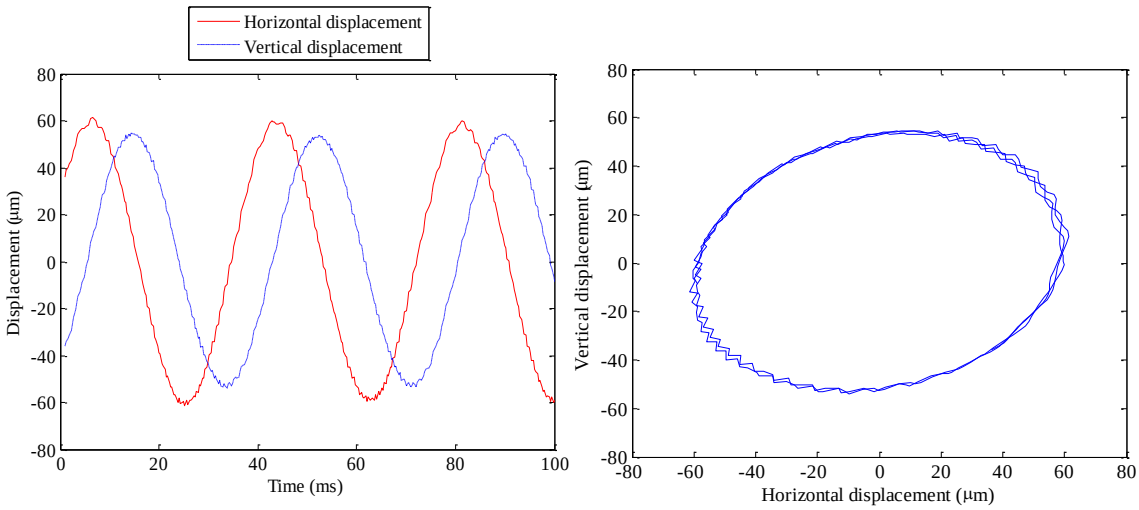

a) **b)**

Figure 5. 18 Experimental response at 1600 RPM using controller "B" at ADRE sensor. a) Time response. b) Orbit.

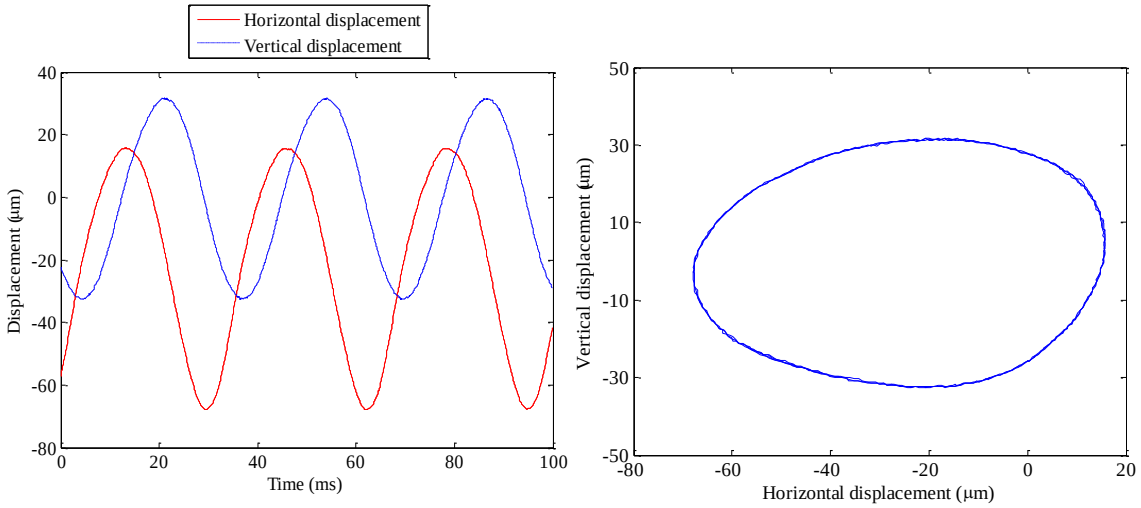

a) **b)**

Figure 5. 19 Experimental response at 1833 RPM using controller "B" at AMB sensor. a) Time response. b) Orbit.

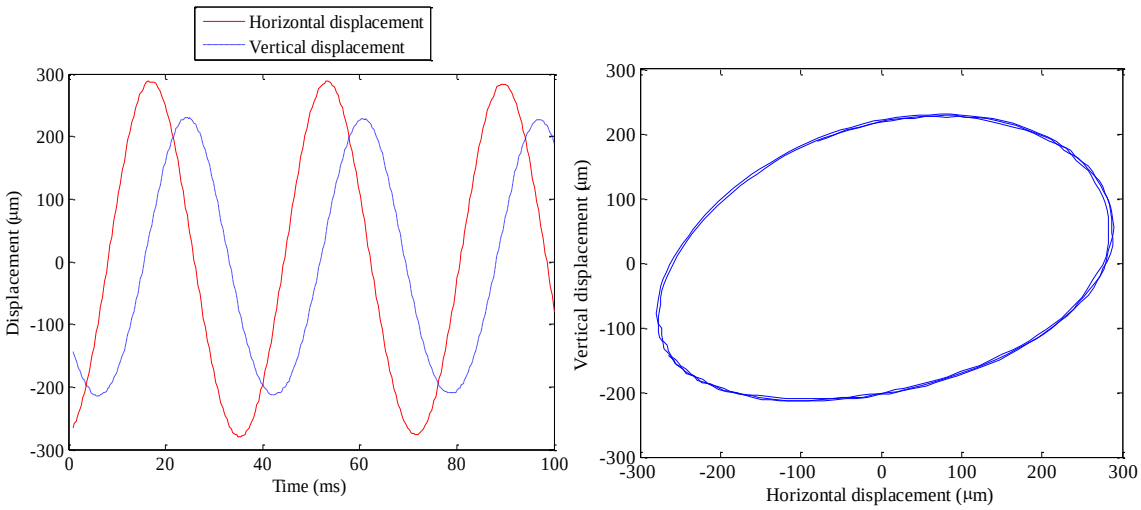

a) **b)**

Figure 5. 20 Experimental response at 1833 RPM using controller "B" at ADRE sensor. a) Time response. b) Orbit.

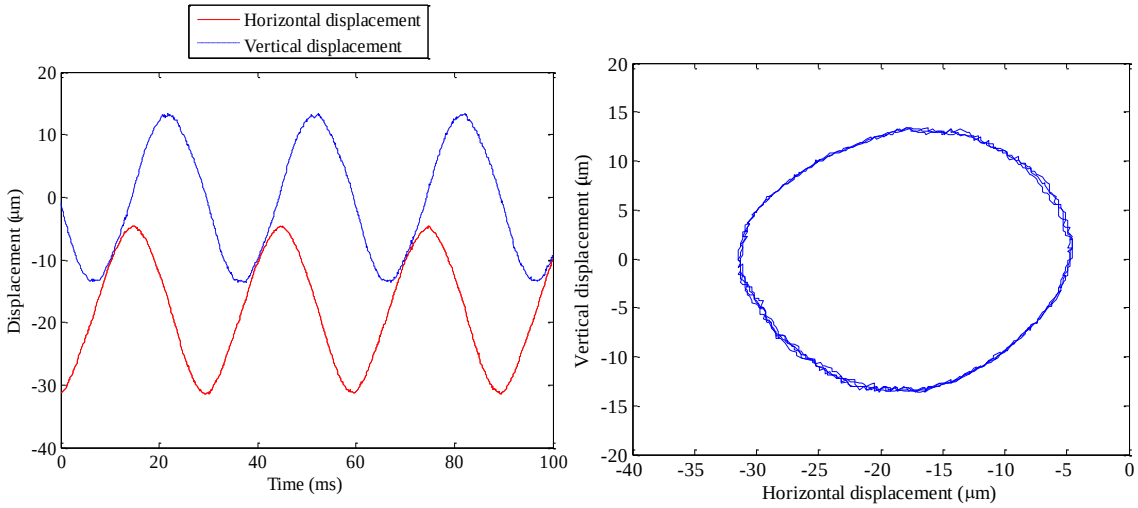

a) **b)**

Figure 5. 21 Experimental response at 2000 RPM using controller "B" at AMB sensor. a) Time response. b) Orbit.

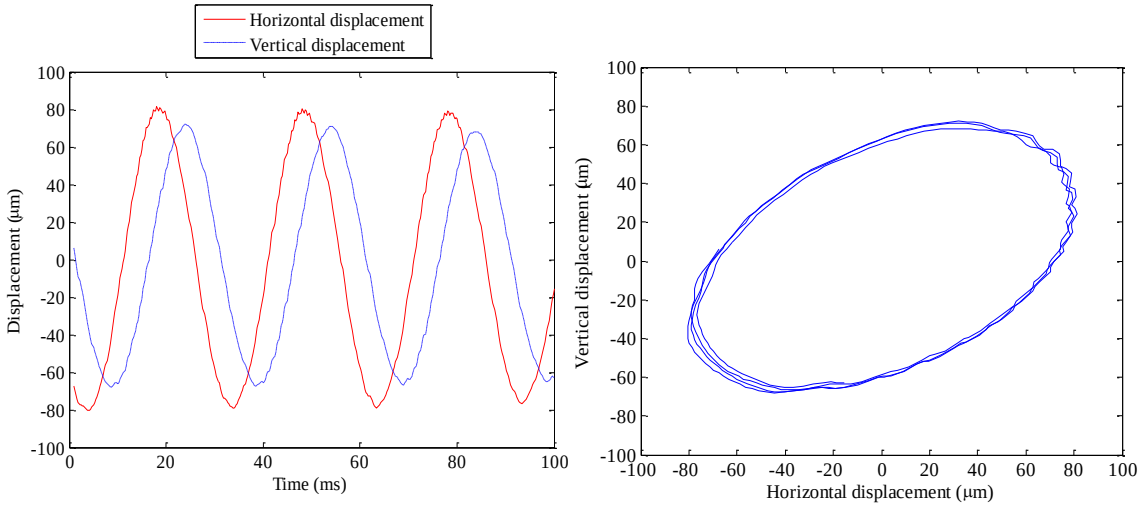

a) **b)**

Figure 5. 22 Experimental response at 2000 RPM using controller "B" at ADRE sensor. a) Time response. b) Orbit.

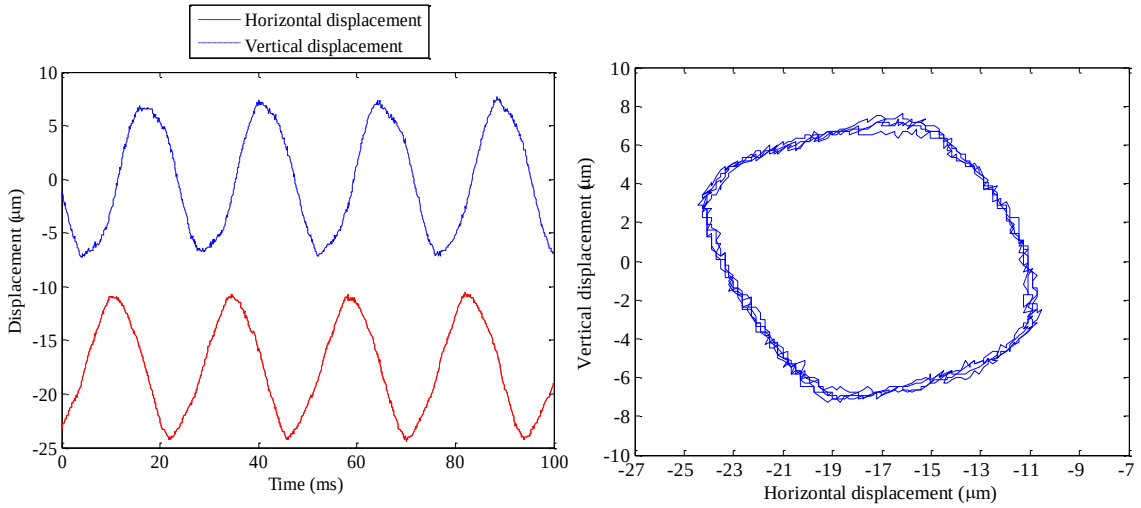

a) **b)**

Figure 5. 23 Experimental response at 2500 RPM using controller "B" at AMB sensor. a) Time response. b) Orbit.

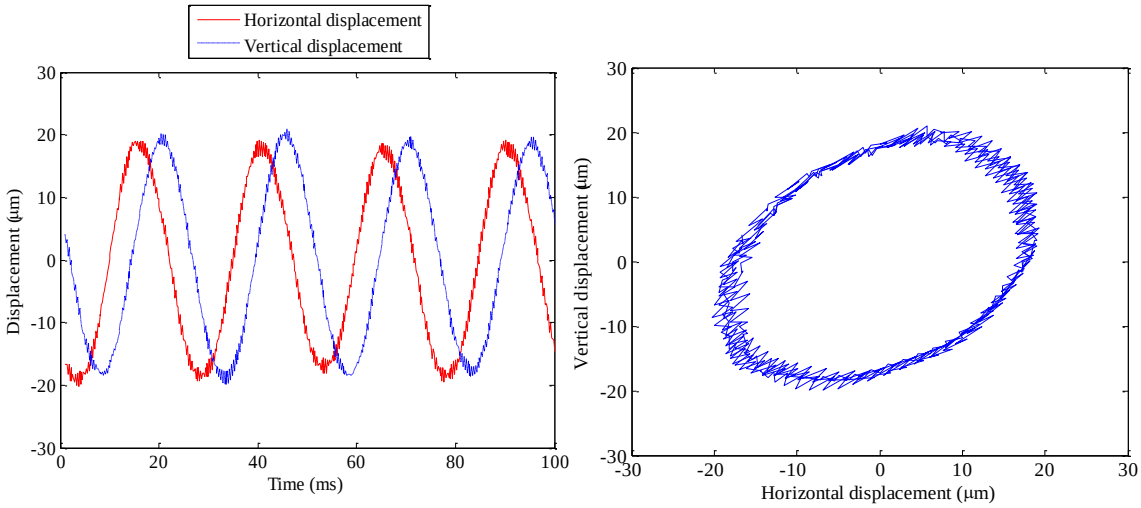

a) **b)**

Figure 5. 24 Experimental response at 2500 RPM using controller "B" at ADRE sensor. a) Time response. b) Orbit.

Figures 5.15 through 5.24 show the system vibration response using controller “B”. From these figures, the following observations can be made.

1. The closed-loop system natural frequency happens at 30.3 Hz, which is 1818 RPM when using controller “B”.
2. This experiment has verified that controller “B” is effective at levitating the system within practical limits.
3. The largest vibration has a speed of 1833 RPM, which roughly agree with the experimental closed-loop critical speed.
4. From AMB sensor data, one can read that the vertical controller with an integral term helps the system overcome gravity, all vibrations are around X-axis, when y=0. While on the other axis, there is always displacement due to rotor or AMB assembly misalignment.
5. From the ADRE sensor, horizontal and vertical vibration are always near the ideal point (0,0), because the initial installment for the ADRE sensor probes.
6. For the same running speed for the two controllers, at the same sensor location, controller “B” and a smaller system vibration response than using controller “A”.

5.4 Comparison of the Experimental Results and Simulation

With the two controllers successfully demonstrated on the test rig, comparisons can be made between the results and the results predicted by the numerical simulations. The simulation using controller “B” is more similar to the experimental results than that using controller “A”, not only in natural frequency, but also in vibration amplitude. The

simulation using controller “A” on the three-mass analytical model has generally smaller vibration amplitude than the experimental result using controller “A” on the actual test rig. Smaller vibration suggests the model system has higher stiffness than the actual system. Therefore, the finite element model is superior to the approximate analytical method from a performance prediction standpoint.

Since it is a cost function controller design method that is developed in Chapter IV, to further investigate the aptitudes of these two modeling techniques to this design problem, a comparison of cost index values for both controllers is made using both experimental and simulation values of position and current. The experiment has a sampling rate of 10 kHz and the simulation has a numerical step size with the same time. Both cases are allowed to come to steady state and then a data vector for 100 ms is taken. The vector includes AMB position and current. The vectors are used in Equation (4.1) which is evaluated with trapezoidal integration. The cost function J is evaluated at each running speed. The values for each speed and each controller are shown in the following table for comparison.

Table VIII Experimental and simulation cost function values comparison

Speed (RPM)	cost function evaluating factor J value			
	Experiment		Simulation	
	controller “A”	controller “B”	controller “A”	controller “B”
1000	0.7532	0.6559	0.0020	0.1473
1600	11.8489	7.7443	0.0701	7.7121
2000	22.4145	23.1188	0.2686	15.0440
2500	7.6301	6.1967	0.0664	4.4818

Seen from the table above, controller “B” has a smaller difference of J values for speed over 1600 RPM than controller “A” experimentally. The cost function evaluating J involves the displacement and control current at the AMB, so the smaller value, the smaller vibration and control effort. It is obvious that controller “B” is more effective than controller “A”. As for the simulation comparison, simulation using controller “B” is more accurate than using controller “A”, this can tell by looking through simulation on the three-mass analytical model results with controller “A”, with stiffer system, the smaller vibration itself is not accurate.

After experimental results, simulation results and cost function value computation, it is safe to come to a conclusion that in designing a controller for this dissimilar bearing support system, the controller designed upon the finite element model is more accurate and more reliable to use with experiment.

CHAPTER VI

CONCLUSIONS

6.1 Contributions

This work is focused on the system modeling, controller design and dynamic analysis of a dissimilar rotor bearing system to increase the state of art knowledge of dissimilar bearing supports. Two modeling methods are proposed for a rotor with one bushing and one AMB, an approximate analytical modeling method and a finite element modeling method. In order to evaluate the two modeling methods, a model based AMB controller design strategy is proposed. The optimum controller design method maintains the proportional derivative control structure that is easy to use with current industry standard hardware. Numerical simulations were conducted using both models with their respective controllers and an experimental test rig was run with implemented both controllers. Stable levitation was achieved for all cases. Non-rotating closed-loop sine sweep tests were conducted on each system. Running speed orbits were measured for several speeds including the first natural frequency and the data used for a quantitative evaluation of a cost function.

Sine sweeps were done on the open-loop systems and compared. It was found that both modeling methods can be used to model the system effectively, but the approximate analytical method is less accurate than the finite element approach. However, the approximate analytical method is easier to employ having no specific rotordynamic expertise. The proposed controller design method was found to be effective for stabilizing the AMB in this dissimilar rotor bearing support system. But for practical implementation on the experimental test rig, the provisions of notch filter, low pass filter and vertical axis integrator had to be included. The effectiveness of the controllers was demonstrated using the closed loop sine sweeps. The running speed tests show the practical implementation is possible for various operating conditions. The cost function analysis of the running speed tests show that the controller designed for the finite element model is quantitatively superior as compared to the other controller for all running speeds examined. This is to be expected because of the higher accuracy model used. The cost function analysis also shows the discrepancy between the experiment and simulation results. The simulation cost functions were lower than the experimental ones due to the use of the same models in simulation as in controller design.

Qualitatively, the entire study shows that one AMB and one bushing can be effectively used on the same rotor although this is not a novel contribution.

6.2 Future Work

Modeling techniques have been shown to be effective and a rotor dynamic performance of a dissimilar support rotor bearing system has been studied. It remains to

be shown that such a system can have the advantages of both bushings and AMB, while avoiding their disadvantages. To this end, future work should include investigations of the static and dynamic load capacity of the system. Also active vibration control techniques which have been developed for pure AMB levitation should be applied to this dissimilar support system. In literature, such as Britta [2010], there are examples of traditional supported rotor with a magnetic actuator added for active damping. Such a system could be replaced with a system with one traditional support and one AMB, thereby eliminating one component while increasing the active damping possibility. Further research should use an actual machine with dissimilar bearing supports in a non-laboratory setting.

BIBLIOGRAPHY

Adiletta, G., Guido, A.R., Rossi C., 1996, "Chaotic motions of a rigid rotor in short journal bearings" *Nonlinear Dynamics* 10: 251-269, KluwerAcademic Publishers., Netherlands.

Adiletta, G., Guido A.R., and Rossi C., 1996, "Non-periodic motions of a Jeffcott rotor with non-linear elastic restoring forces", *Nonlinear Dynamics*, Vol. 11, pp. 37-59.

Antti, K., Jussi, S., Aki, Mikkola, 2007, "Dynamic simulation of a flexible rotor during drop on retainer bearings", *Journal of Sound and Vibration*, Vol. 306, pp. 601-617.

Chang-J., Cai-W., Chen, C.K., 2008, "Non-linear dynamics analysis of rub impact rotor supported by turbulent journal bearings with non-linear suspension", *International Journal of Mechanical Sciences*, vol. 50, issue 6, pp. 1090-1113.

Chang, Y.F., Kang, Y., Tsai, J.W., Mu, L.H., 2000, **"**An investigation in stiffness effects on dynamics of rotor-bearing-foundation systems**",** *Journal of Sound and Vibration*, (2000) 231(2), 343-374.

Cheng, M., Meng, G., Jing, J., 2006, "Non-linear dynamics of a rotor bearing seal system", *Archive of applied Mechanics*, vol.76, issue 3-4, pp.215-227.

Childs, D., 1993, *Turbomachinery rotordynamics: phenomena, modeling, and analysis*, John Wiley & Sons, Inc., New York.

Cuesta, E.N., Medina, L.U., Rastelli, V.R., Montbrun, N.I. and Diaz, S.E., 2003, "A simple kinematic model for the behavior of a magnetically levitated rotor operating in overload regime", *Proceedings of ASME Turbo Expo 2003, Power for Land, Sea, and Air*, June 16-19.

Galary, G., Dehez, B., Grenier, D., 2006, "Finite element modeling of a two degree of freedom spherical actuator", *The International Journal of Computation and Mathematics in Electrical and Electronic Engineering*, vol.25, pp. 399-411.

Keesee, J., Rawal, D., Kirk, R.G., 1991, "Critical speeds and forced response solutions for active magnetic bearing turbomachinery, part 1", *Aerospace Applications of Magnetic Suspension Technology*, Part 2, pp. 539-558.

Kirk, R.G., Gunter, E.J., 1972, "Effect of support flexibility and damping on the dynamic response of a single mass flexible rotor in elastic bearings", NASA CR-2083.

Mohiuddin, M.A., Bettayeb, M., Khulief, Y.A., 1998, "Dynamic analysis and reduced order modeling of flexible rotor-bearing systems", *Computers and Structures*, Vol.69, pp349-359.

Maria, H., Jakub, O., 2010, "PID controller design for magnetic levitation model", *International conference Cybernetics and information*, February 10-13, 2010.

Micheal, I.F., 2006, "Efficient placement of rigid supports using finite element methods", *Communications in Numerical Methods in Engineering*, Vol.22, pp205-213.

Milne, N.G., Beerschwinger U., 1994, "Finite-element analysis of rotor stability in an axial-drive micromotor", *Journal of Micromechanics and Microengineering*, vol.4, pp. 74-83.

Rao, S.S., 2004, *Mechanical Vibrations*, Prentice Hall.

Shigley, J.E., Budynas, R.G., Nisbett, J.K., 2006, *Shigley's mechanical engineering design*, McGraw-Hill.

Sinou, J.-J., 2009, "Non-linear dynamics and contacts of an unbalanced flexible rotor supported on ball bearings", *Mechanism and Machine Theory*, vol.44, issue 9, pp. 1713-1732.

Späh, B., Nordmann, R., Kern, S., Rinderknecht, S., 2010 "Optimal control of chatter vibration of a motor spindle with integrated electromagnetic actuator", *Proceedings of the 8th IFToMM Conference on Rotordynamics*, September 12-15.

Tiwari, R., Vyas, N.S., 1997, "Non-linear bearing stiffness parameter extraction from random response in flexible rotor-bearing system", *Journal of Sound and Vibration*, vol. 203, issue 3, pp. 389-408.

Yinh-S.S., 2001, "Design and Implementation of a Controller for a Magnetic Levitation System", *Proc. Natl. Sci. Counc. ROC(D)*, vol. 11, No. 2, 2001, pp. 88-94.

APPENDIX A

Rotor Finite Element Parameter File

```
Cleveland State University
yunlu
Mar 2  2010
     30
     5
     -1        -3        2         0.
     0.        0.6       0.394     0.    0.        0.        30    0.287   0 0 0 0
     0.        0.853     0.394     0.    0.        0.        30    0.287   1 1 0 0 "bushing"
     0.        0.853     0.394     0.    0.        0.        30    0.287   0 0 0 0
     0.        0.853     0.394     0.    0.        0         30    0.287   0 0 0 0
     0.        0.853     0.394     0.    0.        0.        30    0.287   0 0 0 0
     0.        0.853     0.394     0.    0.        0.        30    0.287   0 0 0 0
     0.        0.853     0.394     0.    0.        0.        30    0.287   0 0 0 0
     0.        0.853     0.394     0.    0.        0.        30    0.287   0 0 0 0
     0.        0.853     0.394     0.    0.        0.        30    0.287   0 0 0 0
     0.        0.853     0.394     0.    0.        0.        30    0.287   0 0 0 0
     0.        0.853     0.394     0.    0.        0.        30    0.287   0 0 0 0
     0.        0.853     0.394     0.    0.        0.        30    0.287   0 0 0 0
     1.8301    0.752     0.394     0.    2.0589    1.0295    30    0.287   1 1 0 0 "disk"
     0.        0.752     0.394     0.    0.        0.        30    0.287   0 0 0 0
     0.        0.752     0.394     0.    0.        0.        30    0.287   0 0 0 0
     0.        0.752     0.394     0.    0.        0.        30    0.287   0 0 0 0
     0.        0.752     0.394     0.    0.        0.        30    0.287   0 0 0 0
     0.        0.752     0.394     0.    0.        0.        30    0.287   0 0 0 0
     0.        0.752     0.394     0.    0.        0.        30    0.287   0 0 0 0
     0.        0.752     0.394     0.    0.        0.        30    0.287   0 0 0 0
     0.        0.752     0.394     0.    0.        0.        30    0.287   0 0 0 0
     0.        0.752     0.394     0.    0.        0.        30    0.287   0 0 0 0
     0.        0.752     0.394     0.    0.        0.        30    0.287   0 0 0 0
     0.        0.375     0.394     0.    0.        0.        30    0.287   0 1 0 0 "MB sensor"
     0.54      0.25      0.394     0.    0.1236    0.2288    30    0.287   0 1 0 0 "center of mass"
     0.        0.5       0.394     0.    0.        0.        70    0.287   1 1 0 0 "center force"
     0.        0.75      0.394     0.    0.        0.        30    0.287   0 0 0 0
     0.        0.0       0.394     0.    0.        0.        30    0.287   0 0 0 0
     100.      200000.   100.
     0.0
```

APPENDIX B

Magnetic Bearing Specifications

(a)	**Bearing Performance Specifications**	**Units**
	Static Load Capacity	12 lbf
	Saturation Current	3.00 A
	Current Stiffness ($\frac{N}{A}$)	11.74 $\frac{N}{A}$
	Position Stiffness ($\frac{N}{m}$)	$-2.1\times10^{4}\ \frac{N}{m}$
(b)	**Bearing Geometry**	
	Number Of Poles Per Quadrant	2
	Stator Stack Length	0.500 in
	Stator OD	2.809 in
	Stator ID	1.380 in
	Rotor OD	1.350 in
	Rotor Lamination ID	0.905 in
	Nominal Gap	0.015 in
	Pole Width	0.207 in
	Pole Height	0.456 in
	Slot Width (at ID)	0.331 in
	Pole Centerline Angle	22.5°
(c)	**Material Properties**	
	Material Grade: Stator	M-19, C-5
	Rotor	Arnon 5, C-5
	Saturation Flux Density	1.25 T
	Relative Permeability	3000
	Lamination Thickness: Stator	0.014 in
	Rotor	0.005 in
	Material Resistivity	18.9 μΩ-in
	Density	0.276 lb/in^3
	Temperature	1350°F
	Insulation	C-5 Both Sides
	Stacking Factor	96 %
(d)	**Coil Specifications**	
	Wire Gauge	23 AWG
	Wire type	Hyslik 200 heavy/round
	Coil Insulation	0.0135 in

	Packing Factor	97 %
	Turns Per Coil	114
	Coil Extension (max)	0.316 in
	Quadrant Resistance (calculated)	0.912 Ω
	Quadrant Inductance (nominal)	6.116 mH
(e)	**Power Amplifiers Specifications**	
	Maximum Continuous Current	3 A
	Peak Current	10 amp for 2 seconds
	Max DC Supply Voltage	48V unregulated
	Minimum Required Voltage	38.67 V
	Minimum Load Inductance	250 μH
	Switching Frequency	20 kHz
	Power Dissipation @ Cont. Current	20 W
(f)	**Position Sensor Specifications**	
	Type	Variable Reluctance
	Number per axis	2
(g)	**Speed Sensor**	
	Type	Hall Effect